The Effect of Environment on the Formation and Evolution of Galaxies in the Distant Universe

Robert W. Chuter

The University of Nottingham

Thesis submitted to the University of Nottingham
for the degree of Doctor of Philosophy

June 2011

"In the beginning the Universe was created. This has made a lot of people very angry and has been widely regarded as a bad move."

– **Douglas Adams**

Supervisor:	Dr. Omar Almaini
Examiners:	Dr. Alastair Edge *(University of Durham)*
	Prof. Michael Merrifield *(University of Nottingham)*
Submitted:	17th June 2011
Examined:	12th August 2011
Final version:	24th August 2011

Contents

List of Figures

List of Tables

Abstract

In this thesis I primarily use the UKIDSS Ultra-Deep Survey (UDS) to investigate the effect environment has on galaxies across the redshift range $0.25 < z < 3.25$. The UDS is a K-selected survey so it does not suffer from the strong biases that affect optical surveys at high redshift ($z > 1$). The combination of a large contiguous area (0.77 deg^2) and depth (K_{AB} $\sim$24) allows us to study a range of environments up to a redshift of $z \sim 3$. Due to the multiwavelength coverage we are able to obtain reliable photometric redshifts which are necessary for studies of environment. I utilise progressive releases of the UDS data to study the effect environment has on the rest frame (U-B) colour of galaxies. Using the U-B colour and absolute K-band magnitude I was able to divide our galaxies into red and blue and study their average environments. In this thesis I also employ data from the spaced based, GOODS NICMOS Survey (GNS) to help study the environments out to high redshift ($z \sim 3$), in which I also study the colour-density relation.

The UDS project was recently enhanced by the addition of $\sim$3500 spectra of high-redshift galaxies, obtained using the VIMOS and FORS2 instruments on the VLT. The data reduction and redshift determination for the VIMOS data is discussed and is exploited to improve the photometric redshifts for the study of environments in the DR8. The $\sim$1600 reliable spectra are utilised directly to investigate the effect that environment has on the spectral properties of galaxies.

We find that red galaxies are on average in denser environments than blue galaxies up to a redshift of $z \sim 2$. The colour-density relation is strongest at the lowest redshifts studied ($0.25 < z < 0.75$) and gradually weakens out to redshift $z \sim 2$ where it becomes almost flat. We also observe a distinct positive correlation between K-band luminosity and local density for galaxies between $1.25 < z < 2.75$. This relation becomes strongest for the blue galaxies on the smallest scale studied (125kpc radius). Through studying the effect of environment on spectral features we have found evidence that galaxies between a redshift of $1.25 < z < 2.2$ have significantly larger values of the C(29-33) index, in denser environments, indicating that older/more passive galaxies, even at this high redshift, reside in denser environments. The other indices similarly tend to indicate that older galaxies inhabit denser environments, whilst the environment has little effect on the properties of the blue galaxies. The spectra also indicate that one age determining index, C(29-33) is a very good indicator of colour for samples of galaxies at high redshift where the traditional measures such as the 4000Å break strength are difficult to obtain. This study of environments leads us to the final conclusion that although the stellar mass of a galaxy is clearly important in determining its evolution, its environment is also an important driver in a galaxy's evolution. Disentangling the relative importance of these drivers (nature vs nurture) will be a major goal in the coming years.

Acknowledgements

First of all, I would like to thank my Mum and Dad for their endless loving support and encouragement, I could, quite literally, not have done it without them. I am in great debt to Omar for giving me the opportunity to work on such a great data set and for his scientific guidance throughout the PhD. I would also like to thank the two postdocs in the UDS group, Seb and Will for their patience, help and friendship over the last four years. A special thanks goes to Ruth for being a great friend, a great listener, a great scientist and a great draft thesis reader.

Whilst in Nottingham I have made many good friends, too many to name here but I make some special thanks here: to Asa for being a great friend and for all those memorable evenings spent in various pubs, bars and even canals; to Emma for making life in Nottingham more interesting and for my 15mins of 'fame' on URN; to Phil, the two Bens and everyone else in MPS, for the many great trips up north and for the stories; to Robby for listening to my problems and for the best rants that I have ever heard; to Mando, Ari and Karima for adding some European sparkle to my life, and to The JA for taking those edges off and becoming mine and Asa's second home.

I would also like to thank friends that are not in Nottingham: to Dan for always being there and being someone who I could laugh and cry with; to Andy and the rest of my friends from home for always listening and being up for a pint. Thank you to anyone who has been a friend over the years, its been grand. Thank you.

Finally thank you to all my family, you are the reason that I am here. Thank you for the fun times and being there so that the bad times weren't so bad, I love you all.

Published work

Much of the work in Chapter 2 has been previously presented in a paper (paper II), while much of Chapter 3 was shown in paper III.

I Hartley W. G., Almaini O., Cirasuolo M., Foucaud S., Simpson C., Conselice C. J., Smail I., McLure R. J., Dunlop J. S., Chuter R. W., Maddox S., Lane K. P., Bradshaw E. J., 2010, "The evolution of galaxy clustering since $z = 3$ using the UKIDSS Ultra Deep Survey: the divergence of passive and star-forming galaxies", MNRAS, 407, 1212.

II Chuter R. W., Almaini O., Hartley W. G., McLure R. J., Dunlop J. S., Foucaud S., Conselice C. J., Cirasuolo M., Bradshaw E. J., 2011, "Galaxy Environments in the UKIDSS Ultra Deep Survey (UDS)", MNRAS, 413, 1678.

III Grützbauch R., Chuter R. W., Conselice C. J., Bauer A. E., Bluck A. F, L., Buitrago F., Mortlock A., 2011, "Galaxy Properties in Different Environments up to $z \sim 3$ in the GOODS NICMOS Survey", MNRAS, 412, 2361.

IV Bradshaw E. J., Almaini O., Hartley W. G., Chuter R. W., Simpson C., Conselice C. J., Dunlop J. S., McLure R. J., Cirasuolo M., 2011, "AGN environments at $z < 1.5$ in the UKIDSS Ultra-Deep Survey", MNRAS, 415, 2626.

V Grützbauch R., Conselice C. J., Bauer A. E., Bluck A. F, L., Chuter R. W., Buitrago F., Mortlock A., Weinzirl T., Jogee S., 2011, "The relationship between star formation rates, local density and stellar mass up to $z \sim 3$ in the GOODS NICMOS Survey", MNRAS, *accepted*.

Chapter 1

Introduction

In the 1920s astronomers thought that the Universe was much smaller, consisting of only our Galaxy, the Milky Way. Then at the end of the 1920s Edwin Hubble proved the existence of galaxies outside of our own by measuring the distance to the Andromeda Galaxy (M31) using Cepheid variable stars (Hubble 1925). These have a well understood relationship between their pulsation period and their luminosity, allowing Hubble to place M31 beyond the Milky Way. He then followed up this work by classifying galaxies into the 'Hubble tuning fork diagram' (Hubble 1936 and updated more recently by, e.g. Lintott et al. 2008) dividing galaxies into 'early types' (ellipticals and lenticular galaxies) and 'late type' (spiral galaxies). This classification system is shown in Figure 1.1. Hubble labeled one end 'early' and the other 'late' but he did not state that this was an evolutionary definition. We now know that the evolution of galaxies is much more complex but Hubble's naming system is still used today. The study of morphology, whether a galaxy is late or early type is still important today as it contains important information about a galaxy's evolution and formation. The morphology of a galaxy can be determined in two main ways, visually or computationally. Galaxy Zoo (Lintott et al. 2008) have used the internet and the public to visually identify galaxies as either elliptical or spiral whereas others, (e.g. Conselice 2003) use more quantative morphological measurements like the Sersic indices or CAS parameters (concentration C, asymmetry A, and clumpiness S) to define the morphology more automatically which is useful in the days of large surveys.

This distinct difference between galaxies is also seen in their rest frame colour. Figure 1.2 shows data taken from the Sloan Digital Sky Survey (SDSS,York et al. 2000) illustrating the distinct differences. Galaxies divided in a rest frame colour - magnitude diagram divide into the red sequence (highlighted in red) and the blue cloud (highlighted in blue). This distinction between red and blue relates to the differences between early and late type galaxies with elliptical galaxies tending to be redder, whilst spirals are more blue. Only around a third of the galaxies in the red sequence have Sa or later type morphologies, despite their greater prevalance in general (Wolf et al. 2005). These colours can be understood in the context of galaxy evolution. Galaxies with ongoing star formation emit more strongly at the bluer end due to very luminous short-lived blue stars. The bluer colour therefore indicates the presence of star formation, though the bulk of the stellar mass may be old. Low mass stars contribute little to the galaxy light, so it tends to be more massive red giants that dominate the galaxies' red light. The precise age of an evolved star has little effect on its colour which is a major reason why the red sequence is so tight. The lack of scatter in the red sequence led Bower et al. (1992) and Stanford

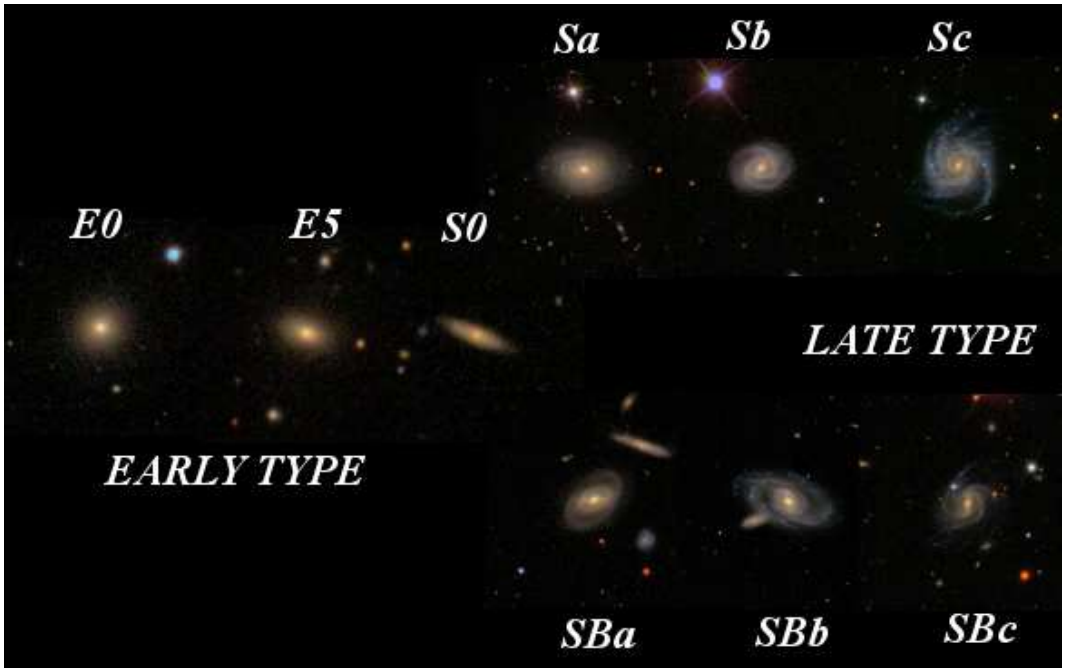

Figure 1.1. Hubble's tuning fork classification diagram, constructed here using galaxies taken from the Sloan Digital Sky Survey (SDSS) and classified by users of Galaxy Zoo (Lintott et al. 2008).

et al. (1998) to conclude that the majority of the star formation either happened at a very similar time or they were formed in the early universe ($z > 2$). With no physical reason for all the stars to be formed simultaneously at lower redshift, they concluded that the stellar populations of the red sequence are likely to be very old. The slope of the colour-magnitude relation reflects the increasing metallicity of more massive (brighter) galaxies (Kauffmann & Charlot 1998). These can hold on to the chemically enriched interstellar medium due to their deeper potential well.
However, how this distinction between red and blue, early- and late-type galaxies arises is still unknown. When, where and through which processes the galaxies are shaped to obtain the properties that we observe today is another key question in galaxy evolution.

1.1 Galaxy Formation

The most popular paradigm for explaining how galaxies formed and gained the observed properties that they have today is hierarchical merging. In this scenario the slight over-densities left over from the quantum fluctuations of the Big Bang allow dark matter to condense. This causes regions of greater dark matter density and thus greater gravitational pull (dark matter halos) which in turn attract more dark matter. These dark matter overdensities then merge with other dark matter overdensities, growing in mass (Lacey & Cole 1993). This mass growth of the dark matter halos, with the smallest forming first is called 'hierarchical assembly'. The Universe, however, is made up of $\sim$73% dark energy, responsible for the observed acceleration of the universe (Riess et al. 1998), 23% dark matter and 4% baryonic matter (Spergel et al. 2007). This baryonic matter falls into the dark matter halos,

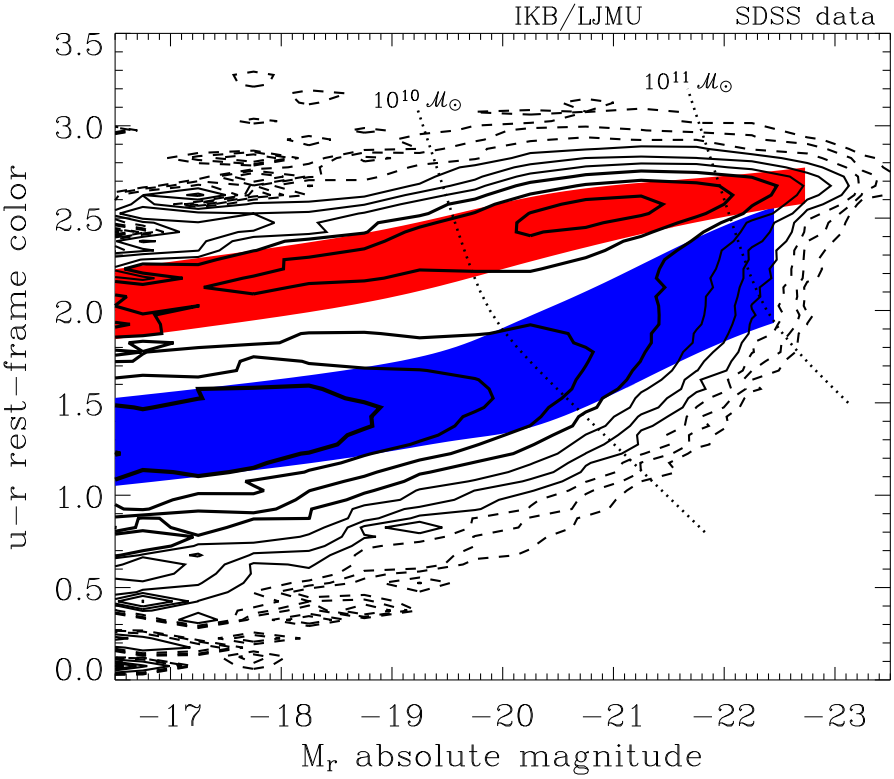

Figure 1.2. Colour-magnitude diagram from the Sloan Digital Sky Survey (SDSS) at $z < 0.1$ showing the galaxy colour bimodality. The black solid and dashed contours represent the number density of galaxies. The red and blue shaded regions show the mean and dispersion ($\pm$ 1σ) of the red and blue sequences based on the fitting described by Baldry et al. (2004)

cooling through thermal Bremsstrahlung emission and line cooling. The cold gas condenses into large molecular clouds, inside which stars form, following a mass distribution known as the stellar initial mass function (IMF).
Observational studies have shown that up to half of the stellar mass within galaxies was in place by $z \sim 1$ (Brinchmann & Ellis 2000; Cimatti et al. 2004). This is also the epoch when the peak in star formation is seen to occur (e.g. Madau et al. 1996). Star formation is also seen to be mass dependant, with the most massive galaxies forming first (e.g. Thomas et al. 2005). Cowie et al. (1996) coined the term 'downsizing' to describe this behaviour. This initially seems to contradict the hierarchical formation paradigm, which requires that the smallest galaxies form first and merge to form the more massive systems. However if the merging galaxies contain very little gas then the star-burst associated with merging cannot occur, this is often termed dry merging (Hopkins et al. 2010).

There are many other significant correlations between the physical properties of galaxies. For example the visual morphologies of galaxies correlate well with colour, star formation rate (SFR), mass, luminosity and surface brightness (Blanton et al. 2003). It is well known that the galaxy stellar mass is closely related to its luminosity. The Tully-Fisher relation (Tully & Fisher 1977) is an empirical relationship that describes the correlation between a spiral galaxies luminosity and the rotational velocity of its disk, such that more luminous galaxies have a higher

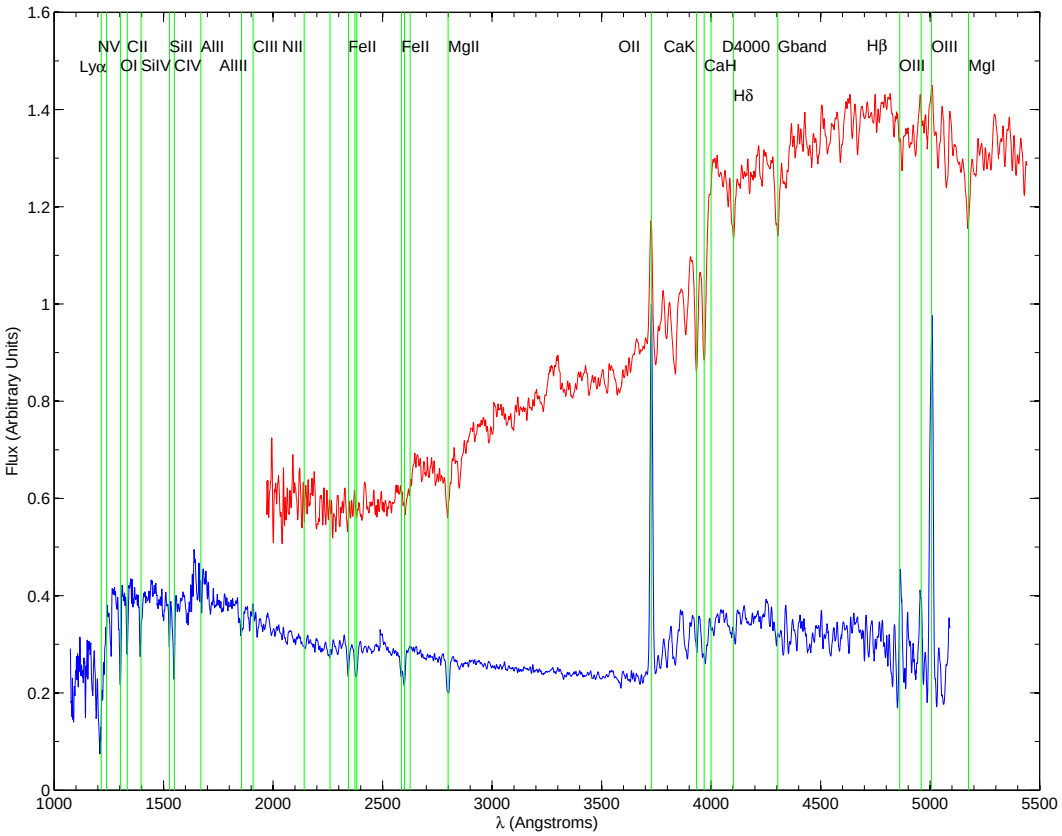

Figure 1.3. Stacked spectra of high-redshift galaxies from the UDSz spectroscopic survey described in Chapter 4, separated into red and blue based on rest frame $U - B$ colours. These illustrative stacks use all galaxies with secure redshifts in the range $0.8 < z < 2.5$, the important emission and absorption lines are shown.

rotational velocity, which has previously been used for determining the distance to galaxies. Faber & Jackson (1976) also found that there are relationships between an elliptical galaxy's luminosity, effective radius and surface brightness, known as the Fundamental Plane. These correlations all show that galaxy structure, luminosity and galaxy mass are correlated, indicating a common formation mechanism for galaxies of similar morphology.

1.2 Galaxy Spectra

Another way of studying galaxies and their evolution is to use spectroscopic surveys. These use a range of instruments with spectrographs (e.g. see Le Fèvre et al. 2005 and Lilly et al. 2007) to obtain spectra of different types of galaxies (e.g. Cimatti et al. 2008). A spectrum of a galaxy shows, amongst other things, the age of the stellar population within the galaxy. This can be seen from the strength of the 4000Å break, the strength of any emission lines and from the shape of the continuum. Figure 1.3 shows two spectra, combined red galaxies (red line - top) and combined blue galaxies (blue line - bottom). The spectra in this figure are stacks of subsets of galaxies from the spectroscopic survey (UDSz) discussed in Chapter 4. They are

divided into red and blue galaxies using a colour-magnitude diagram as discussed earlier. The figure also shows the important emission and absorption lines used for redshift determination and spectra analysis. The red galaxy spectrum shows a much redder continuum compared to the blue spectrum, with much more flux at red wavelengths than at the blue end. The red galaxy spectrum also illustrates a much larger 4000Å break and less [OII] emission compared to the blue spectrum, which are two useful, prominent features in a galaxy spectrum. The 4000Å break is a sudden increase in the continuum flux at this wavelength and is due to the combination of absorption lines of different elements (Ca H and K being the most prominent) and the lack of continuum emission from young blue stars (Kauffmann et al. 2003). The [OII] emission line is widely used as an indicator for recent star formation, since it is directly linked to the presence of ionised gas around star-forming regions. It is also the strongest feature of faint galaxies in the blue and allows star-formation to be traced to high redshifts. These all demonstrate that red galaxies are on average older, as there is less blue light coming from the short-lived hot young stars, with the older, more metal-rich red stars dominating the spectrum instead. One issue however is that the red colours and many spectral features can be caused by both older ages and higher metallicity of the stellar population. This is often referred to as the age/metallicity degeneracy (e.g. Worthey 1994). However some of the spectral features are thought to be more sensitive to age (e.g. the 4000Å break or Balmer lines (Hβ)) while others trace metallicity (e.g. Fe or Mg lines). To break the age/metallicity degeneracy and to recover the age of the stellar population accurately is still a major challenge, especially at higher redshifts, where the 4000Å break moves out of the optical wavelength range.
Active Galactic Nuclei (AGN) spectra are also worth noting here. These have spectra similar to the galaxy spectra discussed above but for Type 1 AGN their emission lines are much broader (FWHM>2000 kms^{-1}), whilst for Type 2 AGN they still remain narrow. The main diagnostic is that AGN exhibit a wide range of ionisation levels (e.g Ne[V], C[IV]). AGN can be hard to separate from star forming galaxies as the spectra can look very similar but AGN typically have much higher ionisation lines than ordinary galaxies (Baldwin et al. 1981).

1.3 Galaxy Environments

It has long been known that the properties of galaxies depend on the environment in which they are located. Elliptical, non-star-forming galaxies occupy more dense regions of space than star-forming, disc-dominated galaxies, giving rise to the so-called morphology-density relation (Oemler 1974; Dressler 1980; Bamford et al. 2009; Pannella et al. 2009) shown in Figure 1.4. The physical origin of this relation is still subject to debate, with disagreement mainly centering on whether the relation arises due to internal or external processes (nature vs nurture).

Most recent low redshift studies (e.g. Kauffmann et al. 2004; Balogh et al. 2004) utilise the Sloan Digital Sky Survey (SDSS) or the Two-degree-Field Galaxy Redshift Survey (2dFGRS) to conduct statistical investigations of galaxy environments. Kauffmann et al. (2004) constrained the specific star formation rate (SSFR) using the 4000Å break and found that the SSFR (and nuclear activity) depend most strongly on local density, from star-forming galaxies at low densities to predominantly inactive systems at high densities.

Studies by van der Wel (2008) and Bamford et al. (2009) found that structure,

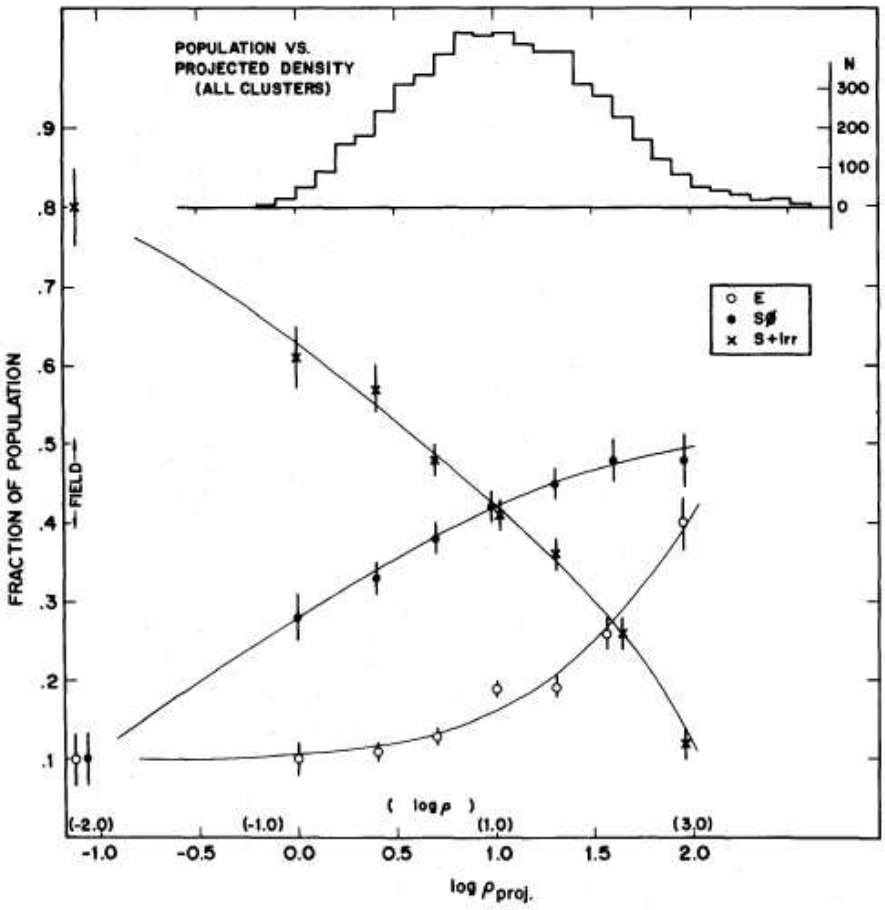

Figure 1.4. The morphology-density relation, reproduced from Dressler (1980). From the outskirts to the centres of clusters there is a smooth increase in the fractions of S0 and elliptical morphological types. These observations have since been extended to encompass smaller group and field environments, and can equally be applied to colour.

colour and morphology are mainly dependent on galaxy mass but that at fixed mass, colour and, to a lesser extent, morphology are sensitive to environment. Studies of Hα (Balogh et al. 2004) found that it's strength does not depend on environment but that the fraction of galaxies with equivalent width, $W_0(H\alpha)$ >4Å is environmentally dependant, decreasing with increasing density. They also noted that emission line fraction appears to depend on both the local environment ($\sim$ 1Mpc) and on the large scale structure ($\sim$ 5Mpc).

Studies at higher redshifts ($z \sim 1$) have used surveys such as DEEP2 (Davis et al. 2003) and VVDS (Le Fèvre et al. 2005). DEEP2 investigations (Cooper et al. 2006; Cooper et al. 2007) used the projected third nearest neighbour statistic, studying galaxy properties and the colour-density relation respectively. They concluded that there is a strong dependence on rest frame $(U - B)$ colour, with blue galaxies occupying lower density regions but showing a strong increase in mean local density with luminosity at $z \sim 1$. This they conclude is consistent with the rapid quenching of star formation by AGN or supernova feedback, as ram pressure stripping,

harassment and tidal interactions, which occur preferentially in clusters, would be insufficient to explain these findings. Cooper et al. (2007) also observed that the fraction of galaxies on the red sequence increases with local density, as in the local Universe, but this weakens with redshift and disappears by $z \sim 1.3$ (see Figure 1.5). A similar convergence is seen by Gerke et al. (2007) between the group and field blue fraction at $z \sim 1.3$.

Other studies at high redshift ($z \sim 1$) have found that galaxy environment does not have an effect on the galaxies properties for galaxies above a mass of $\sim 10^{10.6} M_{\odot}$. Tasca et al. (2009) found this effect in the morphology-density relation and concluded from this that nature (internal processes) gave the galaxy its properties early in its life. A similar result was seen by Iovino et al. (2010) who made similar conclusions. Studies of star formation at this redshift also draw different conclusions. Some authors report a turn around of the local star formation rate-density relation (Elbaz et al. 2007; Cooper et al. 2008), corresponding to enhanced star formation in high density regions. Other groups (Poggianti et al. 2008; Patel et al. 2009) find that the star formation is suppressed in high density environments. The cause of this difference is still unknown but Sobral et al. (2011) presented a study of SFRs over a wide range of environment at $z \sim 1$ and found that the median SFR and star-forming fraction increases with local density up to a critical surface density of Σ=10-30 Mpc^{-3}, decreasing at higher densities, possibly reconciling these contradictory results. Cooper et al. (2010) argue that it is the environmental measures that are causing the discrepancy. They say that given the substantial noise in the measures of environment that intrinsic correlations between galaxy properties and environment can easily be smeared out. They also assert that it is far easier to wash out a correlation than it is to erroneously detect one, given that the environment and internal galaxy properties are measured independently.

The VIMOS VLT Deep Survey (VVDS) investigated the redshift and luminosity evolution of the galaxy colour-density relation up to $z \sim 1.5$ (Cucciati et al. 2006). In agreement with Cooper et al. (2007) they found that the local colour-density relation progressively weakens and possibly reverses in the highest redshift bin ($1.2 < z < 1.5$) (see Figure 1.5). This may imply that quenching of star formation was more efficient in high density regions. The VVDS team also observed that the colour-density relations depend on luminosity and found that at fixed luminosity there is a decrease in the number of red objects as a function of redshift in high density regions. This implied that star formation ends at earlier cosmic epochs for more luminous/massive galaxies, which is consistent with downsizing (Cowie et al. 1996). We note, however, that the VVDS survey is based on optical I-band selection, and as such will be strongly biased against red, passive galaxies at $z > 1$. Conclusions from deep K-selected samples suggest that the galaxy colour bimodality (see Figure 1.2) is present to at least $z \sim 1.5$ (e.g. Cirasuolo et al. 2007) and may be still be present at $z \sim 2$ (Cassata et al. 2008; Kriek et al. 2008; Williams et al. 2009). Furthermore red galaxies have been seen to strongly cluster at $z > 1.5$ (Daddi et al. 2003; Quadri et al. 2007; Hartley et al. 2008; Hartley et al. 2010) which suggests that a colour-density relation may also exist at these higher redshifts. A detailed study of a protocluster at $z = 2.3$ by Steidel et al. (2005) showed that the mean stellar masses and modelled ages are $\sim$2 times larger than an identically selected sample of galaxies outside the cluster. This further hints at environment having an effect to high redshift.

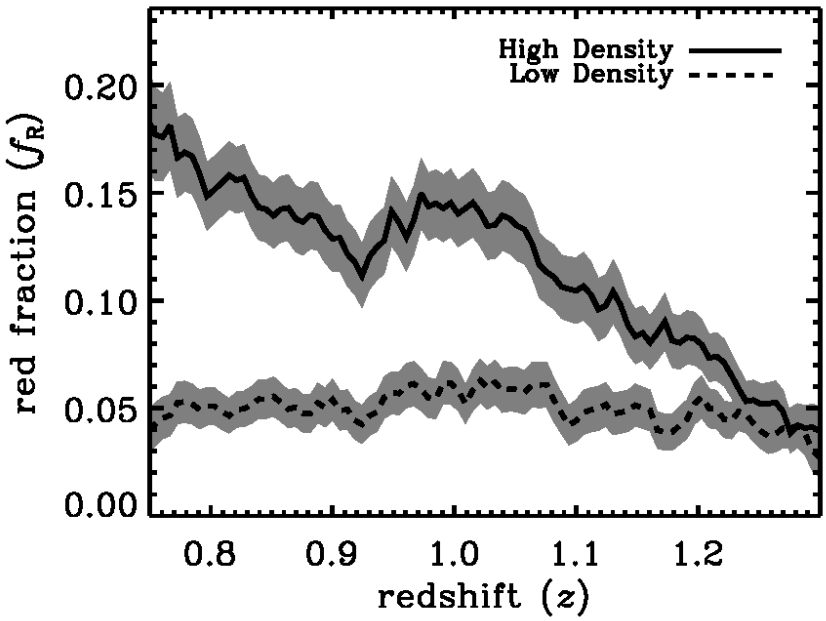

Figure 1.5. The red fraction ($f_R = N_{red}/(N_{red} + N_{blue})$) of galaxies in high (solid line) and low (dashed line) density thirds against redshift from Cooper et al. (2007).

A number of physical processes may be responsible for the observed environmental trends. Mergers or tidal interactions can tear galactic discs apart and are likely to play an important role in forming the most massive galaxies observed today (Toomre & Toomre 1972; Farouki & Shapiro 1981). Other processes such as gas stripping can severely reduce the star formation rate by removing the cold gas from galaxies falling into massive dark-matter halos (Gunn & Gott 1972; Dekel & Birnboim 2006). Feedback is also thought to play a major role, either from AGN or supernovae (e.g. Benson 2005; Springel et al. 2005). These processes may heat or eject the gas within galaxies and thus effectively terminate any further star formation, which can rapidly lead to the build-up of the galaxy red sequence. Finally infalling cold gas in low mass dark matter halos may fall directly onto the galaxy, whereas in high mass halos the gas is thought to be heated by shocks and therefore remains supported (White & Frenk 1991; Birnboim & Dekel 2003). A key goal of observational extragalactic astronomy is to disentangle which of these processes are responsible for establishing the bimodal galaxy populations observed in the local Universe. Over 25 years ago Postman & Geller (1984) used the best available redshift surveys at the time to investigate these processes over different timescales and how these related to the morphology-density relation. They found several distinct regimes. At densities below 5 Mpc^{-3} there is little density dependence, above $\sim$600 galaxies Mpc^{-3} S0's dominate and stripping is likely to be the dominant process and above $\sim$3000 Mpc^{-3} the elliptical fraction increases steeply. In this regime the collision time is of the same order as the collapse time, making disk formation difficult.

With the recent advent of deep, wide-field infrared imaging in the UKIDSS UDS we can now extend studies of galaxy environments beyond $z > 1$. Selection in the

infrared avoids the major biases against dusty and/or evolved stellar populations, allowing us to investigate whether correlations observed at low redshift also occur at high redshift and how these change over time. The large contiguous area of the UDS survey also allows us to probe a wide range of environments using large samples of galaxies. We also use a very deep Hubble Space Telescope (HST) survey to extend this study up to redshifts of $z \sim 3$. The surveys used in this work are described briefly in the following section.

1.4 Overview of the Surveys

The majority of this work has been performed using data from the UKIRT (United Kingdom Infra-Red Telescope) Infrared Deep Sky Survey, Ultra-Deep Survey (UKIDSS, UDS; Lawrence et al. 2007; Almaini et al in prep). The UKIDSS project consists of five sub-surveys of which the UDS is the deepest, with a target depth of K=25 (AB) over a single 4-pointing mosaic of the Wide-field camera (WFCAM, Casali et al. 2007), giving the UDS an area of 0.88 x 0.88 degrees. This makes it the deepest near-infrared survey ever conducted. The UDS was started in 2005 and will continue until at least 2013 improving the depth in J, H and K. The UDS also has a multitude of multi-wavelength imaging with U,B,V,R,i′,z′,Y,J,H,K as well as X-ray, Spitzer IRAC (3.6 and 4.5 μm) and MIPS (24 μm), far-infrared, submillimeter and radio observations. This imaging data is also complimented by ∼4000 spectroscopic redshifts from previous observations (mostly at $z < 1$) and has recently been supplemented with ∼1500 new redshifts (mostly at $z > 1$) from the spectroscopic survey (UDSz) described in Chapter 4.
Data from the GOODS NICMOS survey (GNS) is also utilised, which is a 180 orbit Hubble Space Telescope survey using the NICMOS-3 near-infrared camera. Each of the 60 pointings is centred on a massive galaxy ($M^* > 10^{11} M_\odot$) between $1.7 < z < 3$ covering at total area of 45 arcmin^2 (see Conselice et al. 2011 for more details). The GNS also has good multi-wavelength coverage with X-rays with Chandra and XMM-Newton, optical from HST-ACS, infrared with Spitzer IRAC and MIPS as well as spectroscopic data from VIMOS and FORS2. Both of these surveys are exploited to take advantage of each surveys strengths. The UDS is a much wider survey with a contiguous field whereas the GNS goes deeper over a smaller area. However with more data still being taken the UDS will reach a much greater depth.

1.5 Thesis Structure

In this thesis I present an investigation into the effect of local environment on the properties of galaxies over cosmic time, in particular galaxy colour. I will address the question of when and where passive galaxies are formed and how a galaxy's environment affects this. I also show a preliminary study of the effect of environment on the spectral properties of galaxies through time. Through this I aim to help answer one of the key questions in the field of galaxy environments: is it galaxy mass, galaxy merging on local scales or large scale environment that drives galaxy evolution?

I begin in Chapter 2 with an environmental analysis of galaxies in the UDS Data Release 3 (DR3). Here I separate galaxies into red and blue, and present the environments in which these populations reside between $0.25 < z < 1.75$ with a tentative discussion up to $z \sim 2.25$. Monte Carlo simulations are used to illustrate

the effect of the photometric redshift errors and the effect of outliers. We find that red galaxies inhabit denser environments than blue galaxies up to $z \sim 1.5$ and find a strong luminosity-density relation for blue galaxies on small scales.

In Chapter 3 I present work done with Ruth Grützbauch to study the environments of galaxies in the GOODS NICMOS Survey (GNS). We study the colour-density relation between $1.5 < z < 3$ pushing the work shown in Chapter 2 to higher redshift but in the smaller, non-contiguous field of the GNS. We also study the blue fraction and stellar mass in high and low density quartiles with redshift. We conclude that stellar mass is the most important factor in determining galaxy colour between $1.5 < z < 3$ with local density only having a small effect in the most extreme overdensities.

An outline of the data reduction of an ESO Large Programme is described in Chapter 4. This chapter discusses the spectroscopic reduction and redshift determination for ∼3500 galaxies in the UDS field with VIMOS. A brief outline of the reduction of 90 hours of data is shown, including a summary of the cleaning, identifying and combining of the spectra. The techniques used for redshift determination and the results of this are then examined and some spectra shown.

In Chapter 5 I utilise the spectra discussed in Chapter 4 to conduct a preliminary investigation of the relationship between environment and the spectral properties of galaxies. I combine the spectra in various subsets to analyse the effect environment may have on the spectral properties of galaxies. I measure eight spectral features to investigate whether local density relates to, for example, the equivalent width of [OII] or the 4000Å break strength (D4000). I find tentative correlations between D4000, the C(29-33) index and local environment, both indicating that older galaxies reside in denser environments.

The spectra from Chapter 4 and the significantly deeper UDS data from the DR8 release allows us to further develop the work of Chapter 2. Chapter 6 presents this work, studying the environment of red and blue galaxies up to $z \sim 3$. We use a refined method to calculate the density of galaxies using 1 Gyr redshift bins and a new renormalisation technique. We utilise the increase in the number of spectroscopic redshifts at $z > 1$ to once again run Monte Carlo simulations to understand the effects of the photometric redshift errors. Here we find a strong colour-density relation which weakens over time until at z ∼2 it has mostly disappeared. The colour-density remains flat to z ∼3 at the limits of our analysis.

The results of these chapters are then concluded and discussed in Chapter 7 with some comment made on further work.

Chapter 2

Galaxy Environments in the UDS up to $z \sim 2$

2.1 Introduction

In this chapter I present a study of galaxy environments to $z \sim 2$ using the multi-wavelength data in the UDS survey. This is based on a K-selected sample from the UKIDSS DR3 release. I performed the majority of the work, unless otherwise stated. The limitations of photometric redshifts do not allow robust studies of environments for individual galaxies, so instead I use a statistical method to compare the average environments of galaxy populations. I calculated the environments of the galaxies in the UDS DR3 using a fixed aperture method and 3^{rd} nearest neighbour and ran Monte Carlo simulations to investigate the effects of the photometric redshifts on the density estimates. Much of the work in this chapter is presented in a paper written by me, Chuter et al. (2011).

2.1.1 Data and Sample Selection

This work has been performed using the third data release (DR3) of the UKIRT (United Kingdom Infra-Red Telescope) Infrared Deep Sky Survey, Ultra-Deep Survey (UKIDSS, UDS; Lawrence et al. 2007; Almaini et al in prep). The UDS has an area of 0.88 x 0.88 degrees with 5σ, AB depths within $2''$ apertures for the J, H and K-bands of 23.7, 23.5 and 23.7 respectively, making it the deepest near infrared survey over such a large area at the time of release. For details of the stacking procedure, mosaicing, catalogue extraction and depth estimation we refer the reader to Almaini et al. (in prep.) and Foucaud et al. (2007). The field is also covered by deep optical data in the B, V, R, i$'$ and z$'$ -bands with depths of B_{AB}=28.4, V_{AB}=27.8, R_{AB}=27.7, i'_{AB}=27.7 and z'_{AB}=26.7 from the Subaru-XMM Deep Survey (SXDS) [Furusawa et al. (2008), 3σ, $2''$ diameter]. Data from the *Spitzer* Legacy Program (SpUDS, PI:Dunlop) reaching 5σ depths of 24.2 and 24.0 (AB) at 3.6μm and 4.5μm respectively and U-band data from CFHT Megacam (U_{AB}=25.5; Foucaud et al. in prep) are also utilised, which results in a co-incident area of 0.63 deg^2 after masking.

The galaxy sample used here is primarily based on selection in the K-band image, upon which we impose a cut at K_{AB}=23 to minimise photometric errors and spurious sources and also to ensure a high level of completeness ($\simeq$100 per cent) and reliable photometric redshifts (see Cirasuolo et al. 2010; Hartley et al. 2010). Bright stars are trivially removed from the combined catalogue by excluding objects on a stellar locus defined by 2-arcsec and 3-arcsec apertures, which is effective to $K < 18.1$. The

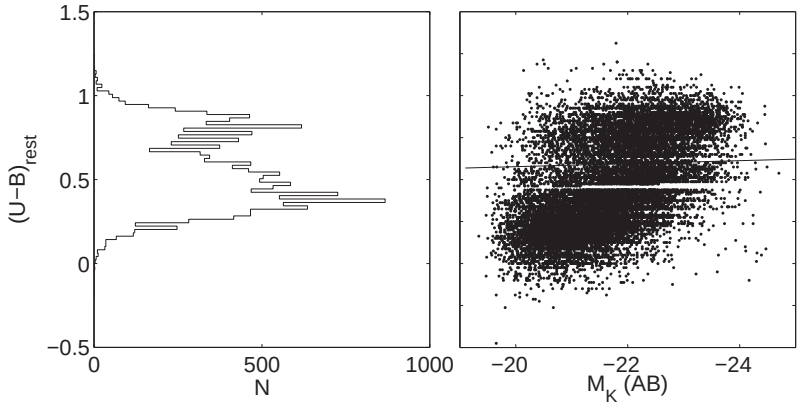

Figure 2.1. Rest Frame $(U-B)$ colours for UDS galaxies between $0.75 < z < 1.75$. Shown as a histogram and as a function of absolute K-band magnitude. The division between red and blue is shown, using the red-sequence slope derived by Hartley et al. (2010).

fainter stars are removed using a $(B-z')-(z'-K)$ diagram (Daddi et al. 2004) and the criterion $(z'-K) < 0.3\ (B-z') - 0.5$. These cuts and careful masking of bright saturated stars and surrounding contaminated regions leave 33,765 galaxies in our sample.

2.1.2 Photometric Redshifts

The magnitudes from the DR3 catalogue were used to determine photometric redshifts and stellar ages by χ^2 minimisation using a large set of templates. This was performed with a code based largely on the HYPERZ package (Bolzonella et al. 2000) using both average local galaxy SEDs and templates from the K20 survey. Six SEDs of observed starbursts from Kinney et al. (1996) were also used to improve the characterisation of young blue galaxies. This yielded photometric redshifts with a $\delta z/(1+z) = 0.008$ with a standard deviation of $\sigma = 0.034$ after the exclusion of outliers (for more detail see Cirasuolo et al. 2007; Cirasuolo et al. 2010 and references within). This also provided rest frame magnitudes and colours, of which the rest frame $(U-B)$ and K-band absolute magnitude are utilised here. Sources with an unacceptable fit ($\chi^2 > 15$) are removed from our sample as these are likely to be unreliable. This removes 4% of the galaxy sample, the majority of these are either QSOs (36%), cross-talk (26%) or the minor members of pairs or mergers (23%), with the remainder consisting largely of objects with very low surface brightness. The fraction of otherwise useful objects rejected is therefore <0.6%.

2.1.3 Passive Sample

To define a passive galaxy subset with minimal contamination from dusty star forming objects we use a subset of galaxies outlined in Hartley et al. (2010). Templates were used to fit either an instantaneous burst parameterised by an age, or an exponentially decaying star-formation rate parameterised by an age and τ, the e-folding time in the exponentially declining star-formation rate, such that,

$$SFR = SFR_0 \times e^{-age/\tau} \tag{2.1}$$

	$0.25 < z < 0.75$	$0.75 < z < 1.25$	$1.25 < z < 1.75$	$1.75 < z < 2.25$
Red	3,469	3,500	2,565	481
Blue	7,367	7,255	4,674	1,711
Passive	1,623	1,395	722	87
S.F.	6,938	6,741	5,048	1,817

Table 2.1. Table showing the number of galaxies in each sample and in each redshift range, including our conservative subsets of passive and actively star-forming galaxies.

where SFR is the star-formation rate at the time of observation and SFR_0 was the initial value. We define a conservative passive sample as galaxies that are simultaneously old (age>1Gyr) and have ongoing star formation with $SFR \leq 0.1\%$ of SFR_0, and a star forming sample with $SFR \geq 10\%$ of SFR_0, with 3947 and 22,158 galaxies in each sample respectively.

To define the red sequence we performed a χ^2 minimisation to fit an equation of the form $(U - B) = a \times M_K + b$ to the old, burst galaxies, defining the red sample to be all galaxies within 3σ of this fit (see Hartley et al. (2010) for a more detailed description). In this work, to separate red and blue galaxies, we use the red-sequence slope from Hartley et al. (2010) but choose the division between the two populations to fit the minimum in the overall colour bimodality (as shown in the histogram in Figure 2.1). This leads to a dividing line in the colour-magnitude diagram as follows:

$$(U - B) = -7.09 \times 10^{-3} M_K + 0.52 \tag{2.2}$$

This boundary was found to separate the red and blue populations effectively to $z \sim 1.75$. At higher redshift the bimodality in galaxy colours is less clear, which may in part be due to photometric errors. A full examination of this issue and the evolution of the red sequence will be presented in Cirasuolo et al. (in prep). Previous studies have found evidence for an evolution in the location of the red sequence with redshift (e.g Brammer et al. 2009). For simplicity we choose not to model the red sequence in such detail and instead use the fixed colour selection boundary given above. We note, however, that using an evolving boundary made no significant difference to any of the conclusions presented in this work.

Table 2.1 shows the resulting number of red and blue galaxies assigned to each photometric redshift bin, including the conservative subsamples of passive and actively star-forming galaxies.

2.1.4 Environmental Measurement

We used two methods to calculate galaxy environment: Counts in an Aperture and nth Nearest Neighbour. In both methods all the galaxies within a photometric redshift bin are collapsed down onto a 2D plane and the redshift information within the bin is not utilised any further. In the aperture method apertures of 1Mpc, 500kpc and 250kpc diameter (physical) are placed on each galaxy and the number of galaxies within that aperture are counted (N_g^{Aper}). A sample of ∼100,000 random galaxies are then put down in the unmasked regions and the number of randoms within the aperture are counted (N_r^{Aper}). The number of galaxies within the aperture

is then normalised to give the final density measurement, ρ/ρ_r:

$$\frac{\rho}{\rho_r} = \frac{N_g^{Aper}}{N_r^{Aper}} \times \frac{N_r^{Tot}}{N_g^{Tot}} \tag{2.3}$$

where N_r^{Tot} and N_g^{Tot} are then total number of random points and galaxies respectively, so that ρ/ρ_r=1 corresponds to a density consistent with that of a random distribution of galaxies. This method was chosen to be the basis of this work as it is conceptually simple, and, as concluded by Cooper et al. (2005), this technique has a distinct advantage in fields masked by a large number of holes. The nearest neighbour method would require the exclusion of a large fraction of data close to holes and field edges.

The nth nearest neighbour method was first employed by Dressler (1980), this calculates the distance to the nth nearest galaxy, D_n in Mpc and is expressed here as a surface density,

$$\Sigma_n = \frac{n}{\pi D_n^2} \tag{2.4}$$

The surface density, Σ_n is then renormalised such that,

$$\delta_n = \frac{\Sigma_n}{\bar{\Sigma}} \tag{2.5}$$

where $\bar{\Sigma}$ is the median density of galaxies within the field. To reduce the effect of the edges, the distance to the nearest edge was calculated and if this was less than the distance to the third nearest neighbour then the object was removed from the sample. This method was only used in this work to test the primary findings of the aperture method.

2.2 Results

Below we explore the relationship between galaxy colours and environment as a function of redshift. Relatively broad redshift bins are used to minimise the contamination due to photometric redshift errors. These sources of uncertainty are explored further in section 2.3.

2.2.1 Red and Blue Environments

Figure 2.2 shows histograms of galaxy environments within two apertures of 1Mpc and 500kpc diameter. These are divided into four redshift bins between $z = 0.25$ and $z = 2.25$ and into red and blue populations. A KS-test was performed on the samples to assess the difference between the red and blue populations, with all but the final redshift bin showing highly significant differences between the two populations. In the first three redshift bins we can exclude the null hypothesis that the red and blue galaxies are drawn from the same underlying population with a significance in excess of 5σ significance, falling to $<2\sigma$ and $<1\sigma$ significance at $z > 1.75$.

Figure 2.3 is a plot of the mean density of red, blue, passive (black) and star forming (cyan) galaxies in bins of absolute K-band magnitude. Error bars are derived from the error on the mean density of galaxies within a given bin. Sources of error are explored further in Section 2.3. The passive and star forming galaxies are defined in Section 2.1.3. As before they are plotted in four redshift bins but with an additional

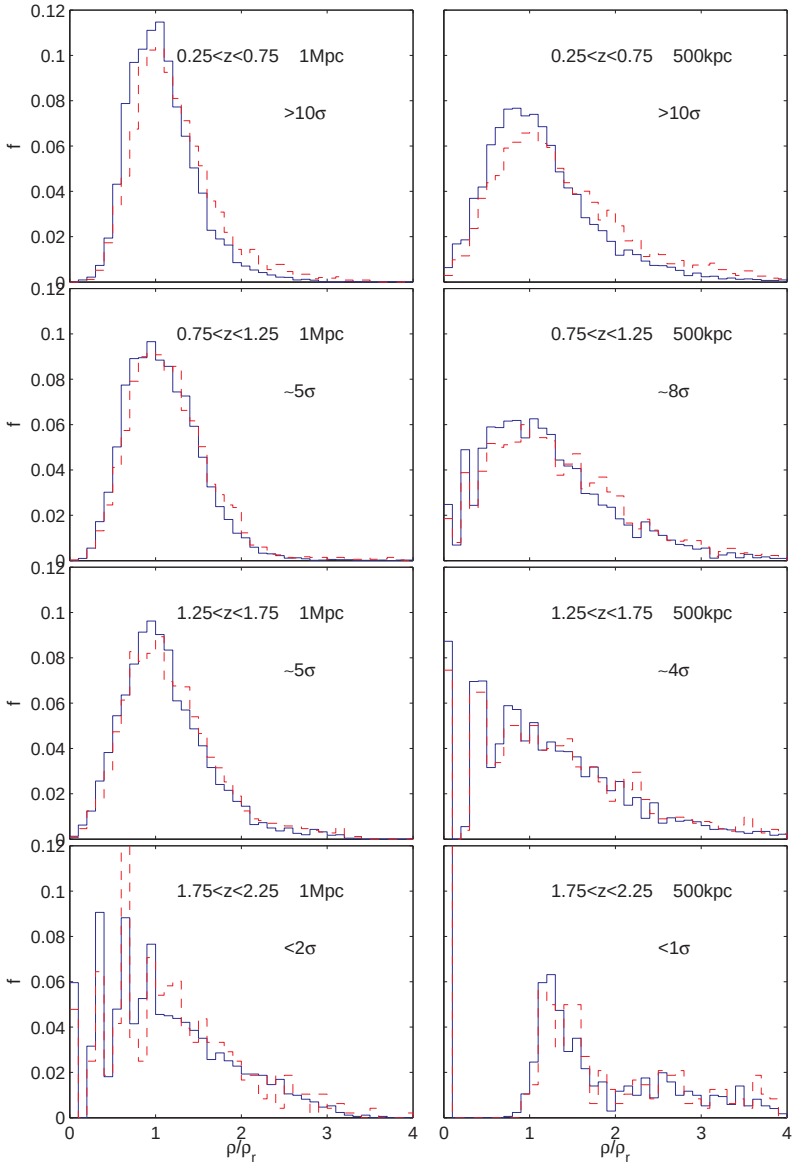

Figure 2.2. Histograms of the density of galaxies within 1Mpc and 500kpc diameter apertures compared to a random sample for red (dashed line) and blue (thick line) galaxies. The σ values are obtained by performing a KS test, representing the significance in rejecting the null-hypothesis that the samples are drawn from the same underlying population.

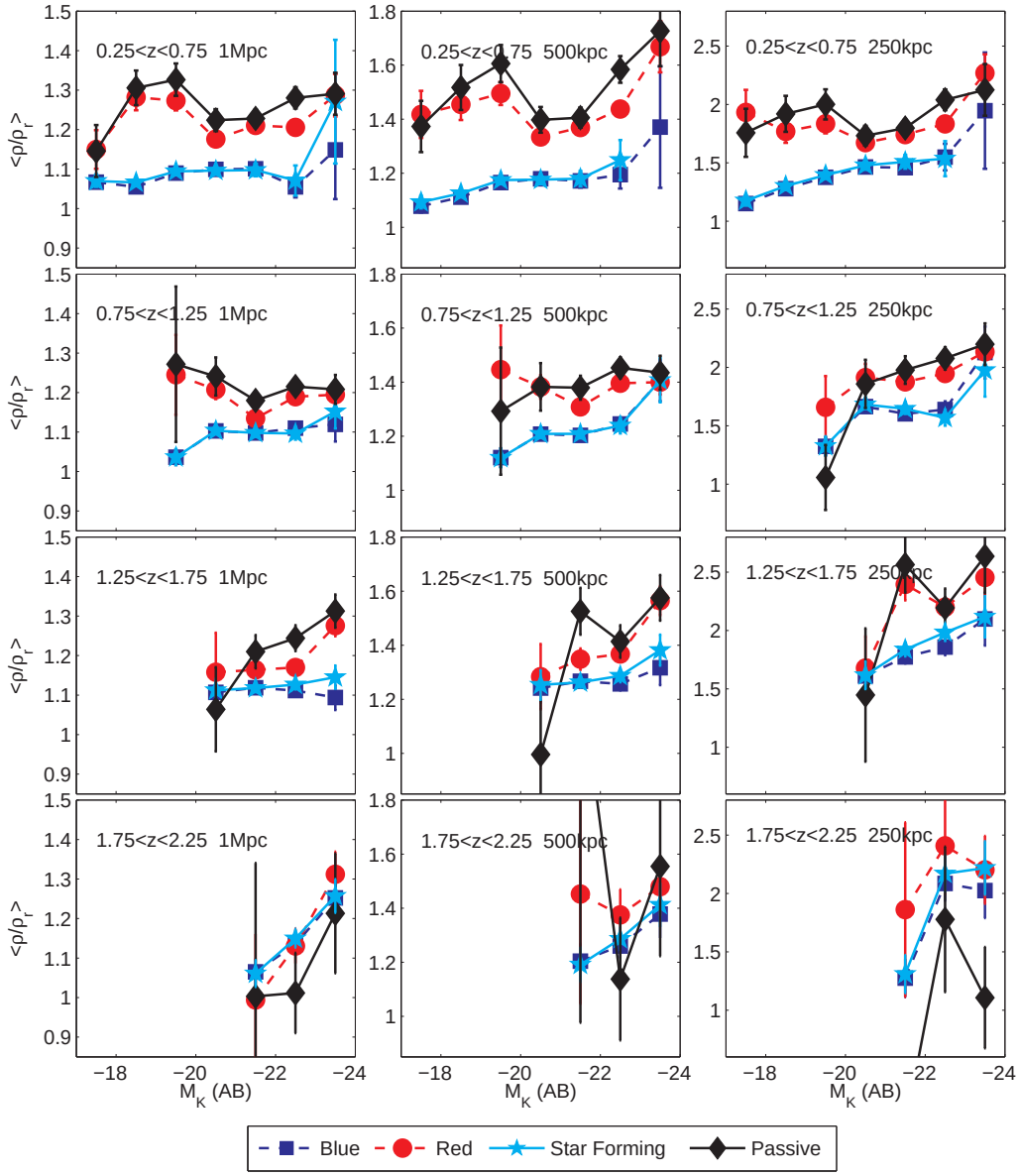

Figure 2.3. The average galaxy overdensity as a function of K-band luminosity, displayed in four redshift bins (top to bottom) and using projected apertures of diameter 1Mpc, 500kpc and 250kpc (three columns). Galaxies are displayed in red, blue, passive and star-forming subsets, as defined in Section 2.1.3. Note the change in scale for each column. The environments are defined so that ρ/ρ_r=1 corresponds to a density consistent with that of a random distribution of galaxies.

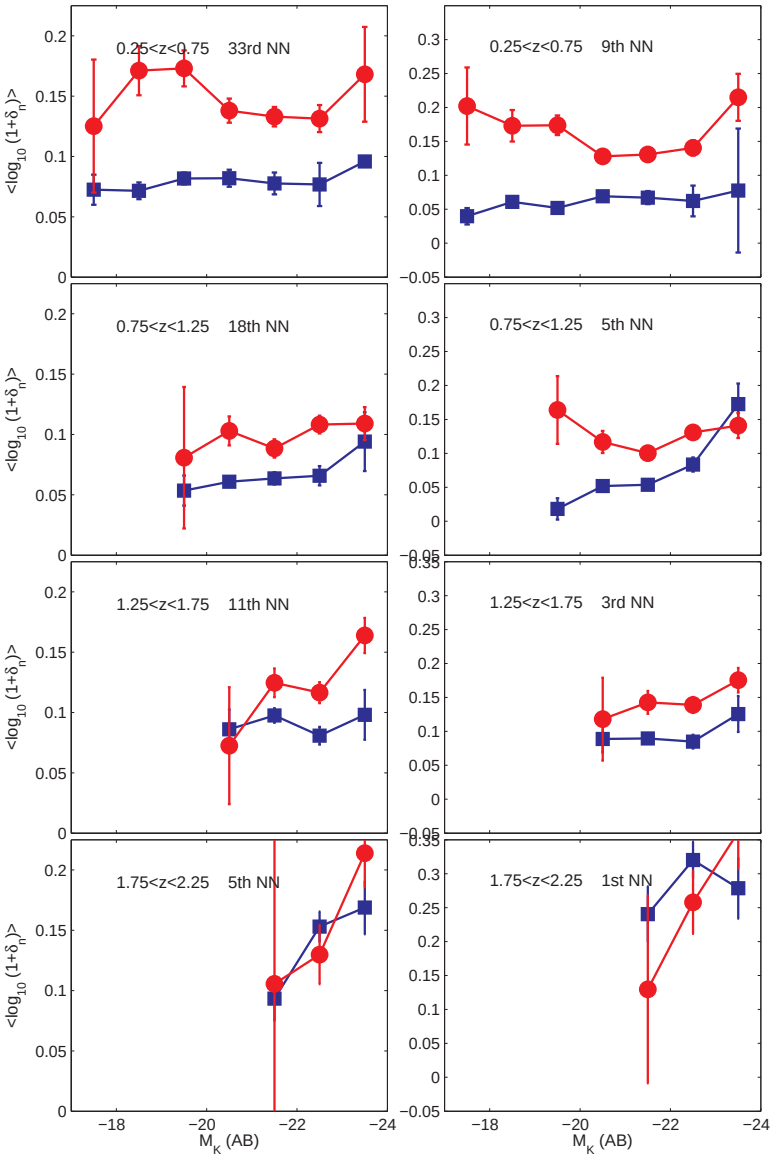

Figure 2.4. The nearest neighbour density of red and blue galaxies with the nearest neighbour chosen so that the mean distance probed was a diameter of 1Mpc and 500kpc in each redshift bin.

250kpc aperture. This plot illustrates that red and/or passive galaxies reside in significantly denser environments than blue and/or star-forming galaxies from the present day to $z \sim 1.5$, and this difference is apparent at all luminosities. This is comparable to what has been found in the local universe by other studies (Kauffmann et al. 2004; van der Wel 2008).

Figure 2.3 also shows that passive galaxies (shown in black) follow a similar density profile to red galaxies but are on average in slightly denser environments. This supports the conclusion that passive galaxies within the red population are responsible for the enhanced environments compared to blue star-forming objects. The environments of galaxies that were red but not in the strict 'passive' sample were also investigated and these were found to lie in-between the red and blue galaxy environments, as would be expected (these are not shown for clarity). The actively star-forming galaxies exhibit the same environmental dependence as the blue galaxies, following the same luminosity-density profile.

In addition to the clear separation of red and blue galaxies, we also find a general trend of increasing galaxy density with luminosity, particularly for blue galaxies and on smaller scales. Inspecting the two intermediate redshift bins in Figure 2.3, on scales below 500kpc we find that the most luminous blue galaxies appear to inhabit environments approaching those of red/passive galaxies. These results are consistent with the findings of Cooper et al. (2007), who observed a strong increase in local density with luminosity for blue galaxies at $z \sim 1$. Our results appear to extend these findings to higher redshift, suggesting that the epoch $1 < z < 2$ represents a key period of transformation of massive galaxies from the blue cloud onto the passive red sequence.

The nth nearest neighbour method is also shown (Figure 2.4) as an alternative environmental estimator, to provide a test of the results presented earlier and to allow comparison with previous work (e.g. Cooper et al. 2007). The nth nearest neighbour was calculated for all the galaxies as a function of absolute magnitude, using the method outlined in Section 2.1.4. The value of n is chosen to probe the same mean scale as the apertures method. The results appear globally consistent with those derived by the aperture method.

2.2.2 Colour-Density Relation

In Figure 2.5 we display average density as a function of $(U - B)$ rest-frame colour, with faint ($-22.5 < M_K < -21.5$) and luminous ($-24 < M_K < -22.5$) objects shown in green and black respectively. This shows a clear trend for galaxies below $z \sim 2$, with redder galaxies occupying denser average environments. In the lowest redshift bin this change occurs very abruptly at the boundary in the colour bimodality at $(U - B)_{rest} \sim 0.7$ (see Figure 2.1). There is also a general trend for more luminous galaxies to occupy denser environments.

In summary, we have found strong evidence that red galaxies are on average found in denser local environments than blue galaxies, extending the comparison to a higher redshift than any previous study. Cooper et al. (2007) probed up to $z \sim 1.3$, finding that red and blue galaxies at this redshift occupy indistinguishable environments. In contrast we find that there is a significant difference between red and blue galaxies between $1.25 < z < 1.75$ (see Figures 2.2 and 2.3). This difference is likely to be due to our method of selecting galaxies from deep infrared imaging. Very red, passive galaxies will have been missed from the R-band selected candidates used in the DEEP2 study. This selection effect can be quantified using our UDS

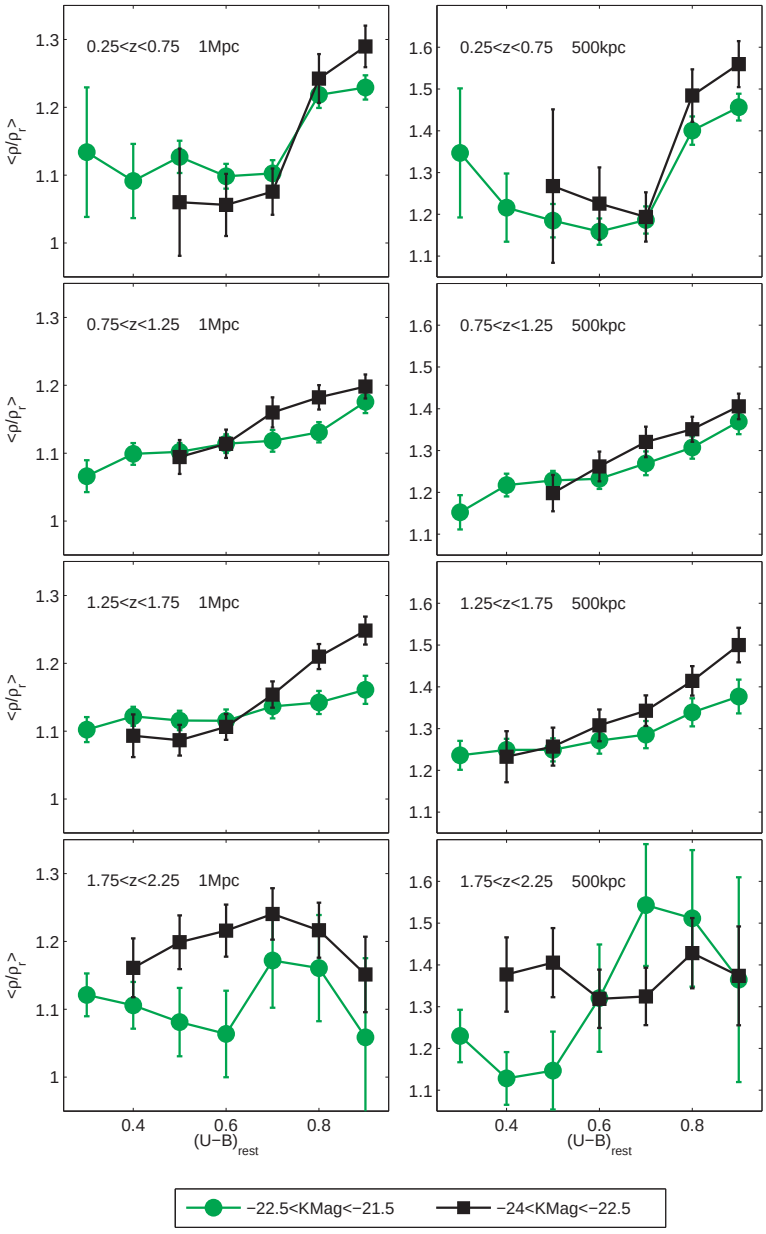

Figure 2.5. The average galaxy density in a 1Mpc and 500kpc diameter apertures compared to a random sample as a function of $(U-B)$ rest frame colour. We separate high (black) and low (green) luminosity subsets. Note the change in y-axis values between the two different aperture sizes.

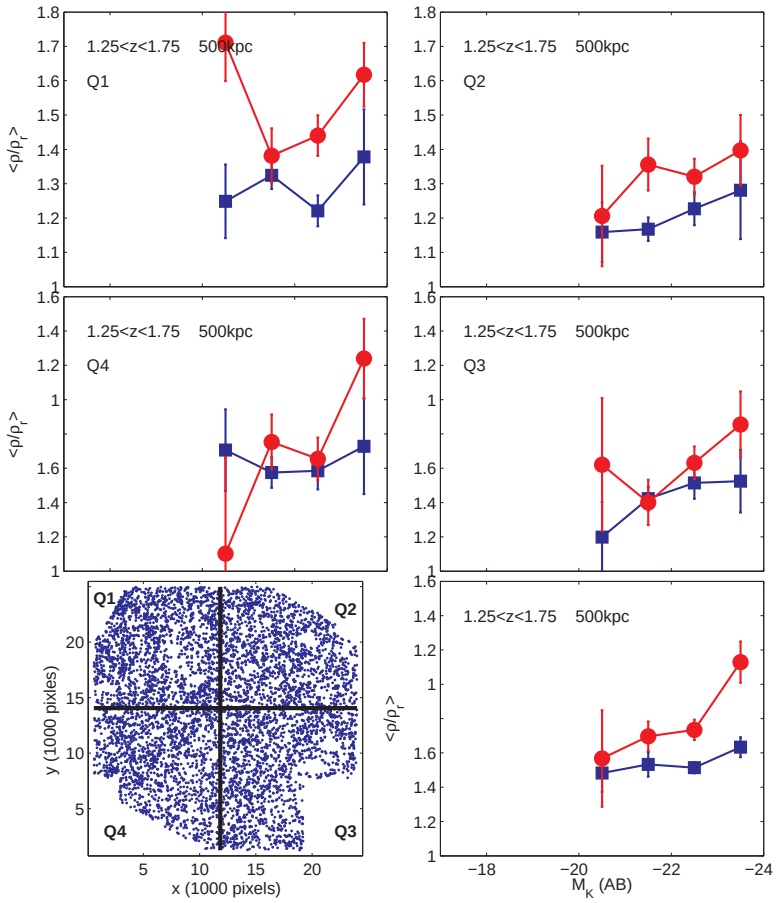

Figure 2.6. Showing the density of red and blue galaxies against K-band luminosity in four quadrants of the UDS field shown in the bottom left, using median values of x and y to calculate the position of the centre. The overall result for the field at $1.25 < z < 1.75$ is shown in the bottom right with the error bars calculated from the error on the mean of the four quadrants, to give an estimate of the cosmic variance.

sample. Considering only the most luminous galaxies ($M_K \leq -22.5$) in the redshift range $1 < z < 1.3$, if we impose the selection criteria of DEEP2 ($R_{AB} \leq 24.1$) we find that 75% of red galaxies would be missed compared to only 20% of the blue sample. At fainter luminosities virtually no red/passive galaxies are selected.

2.3 Investigating Sources of Error

In this section we conduct a number of tests to investigate various source of systematic uncertainty. We attempt to quantify the cosmic variance in our data by dividing the survey into four quadrants. A volume limited study of the brighter galaxies is also performed, to allow a clearer comparison between different redshift bins. Finally we investigate the effects of photometric redshift errors using Monte Carlo simulations.

2.3.1 Cosmic Variance

To attempt to quantify the effects of cosmic variance on our results we divide the UDS field into four quadrants. The median values of the x and y positions of the galaxies were used to divide the field, to ensure that the number of galaxies in each quadrant was comparable. The results for the galaxies in the redshift range $1.25 < z < 1.75$ are shown in Figure 2.6. The average density versus K-band absolute magnitude is shown for the four quadrants, with the bottom left panel showing the projected distribution in the field. The lower right panel shows the original result from Figure 2.3 (red and blue only) but with the error bars calculated from the error on the mean of the densities in the four quadrants in each magnitude bin. It can be seen that the distinction between red and blue galaxy environments remains, although there are clearly significant variations across the field. We conclude that while field variance is clearly present in these data the primary findings remain robust. Similar conclusions were drawn from other redshift bins and on other scales, which are not shown in the interests of brevity.

As a cautionary remark, however, we note that strictly speaking we have only tested the *internal* field variance, since despite the relatively wide field of the UDS (50×50 comoving Mpc at $z \sim 1$) we may nevertheless be prone to large-scale cosmic variance due to unusual superstructures (Somerville et al. 2004). Testing against such effects will require further wide-area infrared surveys, such as the forthcoming VIDEO and Ultra-VISTA surveys.

2.3.2 Volume-Limited Sample

Our measurement of environmental density is based on a flux limited survey, so by definition we are using fainter galaxies to define environments at low redshift. To investigate the influence of this systematic effect we reduced the sample to only the brightest galaxies with $M_K \leq -22$ (AB) and repeated the environmental analysis using this volume-limited sample. This allows the galaxies to be used as tracers in the measure of environment over the same range in luminosity at all redshifts, to allow a fairer comparison between epochs. The results are shown in Figure 2.7, where the average density versus K-band luminosity is shown for comparison with the flux-limited study in Figure 2.3. As expected, the volume-limited study is much noisier (particularly at low redshift) but the results are consistent with the primary findings of Section 2.2. Red and/or passive galaxies are found to occupy denser environments on average to $z \sim 1.5$.

2.3.3 Monte Carlo Simulations

Monte Carlo simulations were conducted to investigate the effect of photometric redshift errors on our results, explicitly allowing for the effects of outliers and catastrophic errors. Such errors would generally dilute differences in galaxy environments, but could potentially introduce fake overdensities if a large fraction of low-redshift structure is incorrectly assigned to a higher redshift bin. We note, of course, that the effects of photo-z errors are already present in the data, so these simulations can only provide an indication of the magnitude of the shifts due to these effects.

The distribution of spectroscopic versus photometric redshifts used in this field are shown in Figure 2.8, with spectroscopic redshifts derived from a variety of sources (Yamada et al. 2005; Simpson et al. 2006; Akiyama et al., in prep; Simpson et al.,

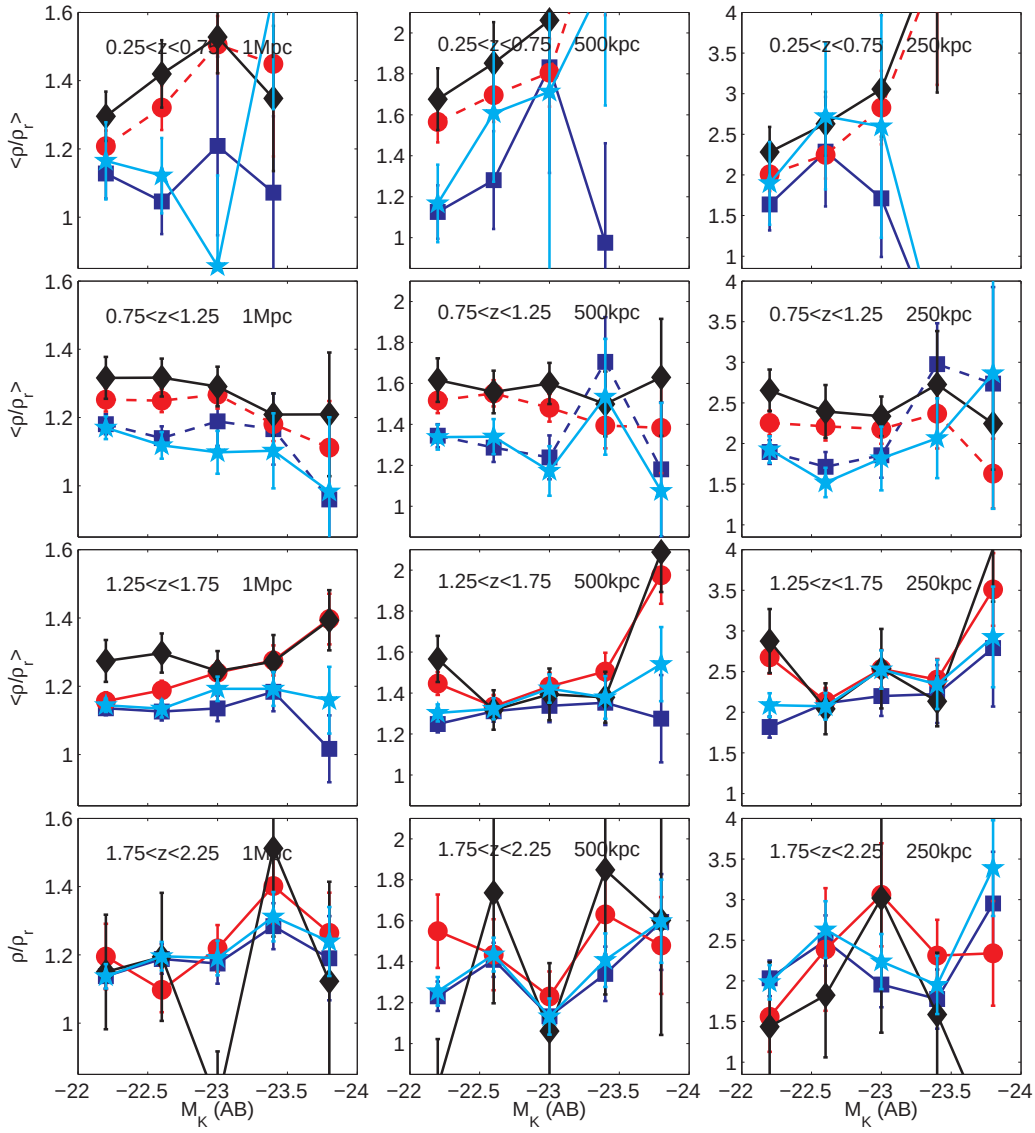

Figure 2.7. As Figure 2.3, but using only the brightest galaxies with M_K $\leq$-22 (AB) as tracers of galaxy density. Note the change in y-axis values between the three different aperture sizes

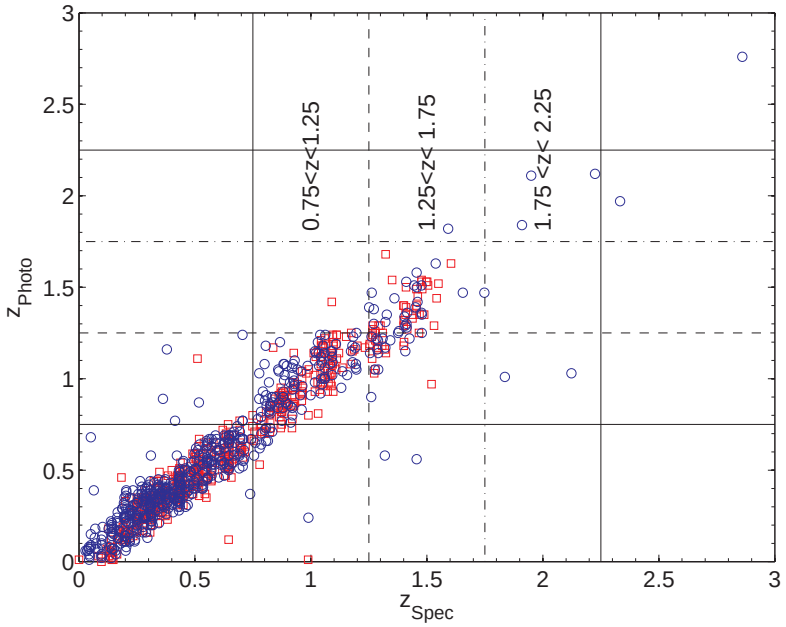

Figure 2.8. Plot of the reliable spectroscopic redshifts against photometric redshifts, highlighting the three highest redshift bins, $0.75 < z < 1.25$, $1.25 < z < 1.75$ and $1.75 < z < 2.25$, with AGN and radio galaxies removed. The red squares and blue circles indicate the red and blue galaxies respectively, as defined in section 2.1.3.

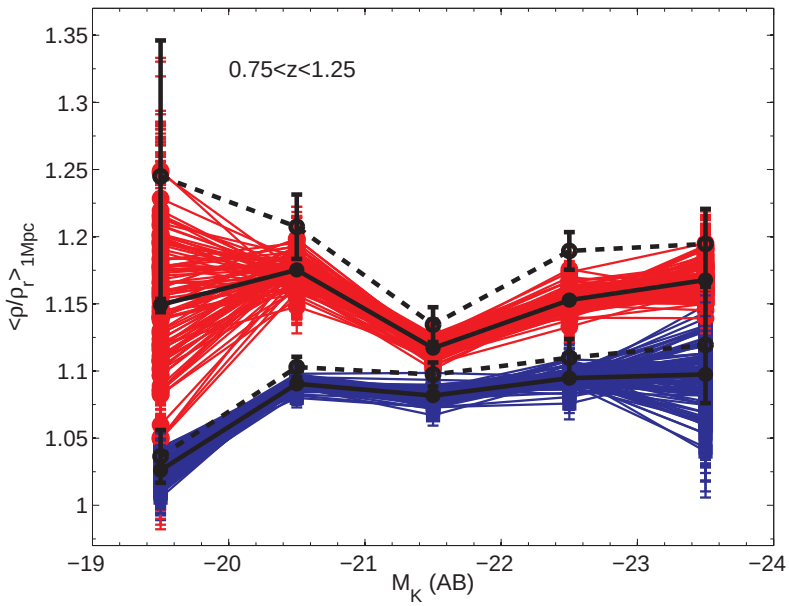

Figure 2.9. Monte Carlo simulation showing the effect of the photo-z errors on our measurement of galaxy overdensity, based on 100 simulations. The thick black line shows the average of the simulations and the dashed black line shows the original result for $0.75 < z < 1.25$ from Figure 2.3.

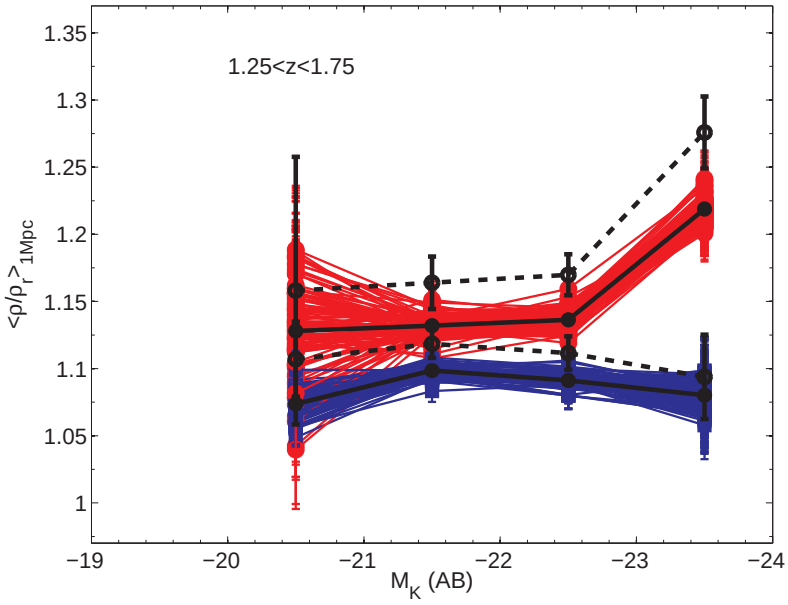

Figure 2.10. As Figure 2.9 but for the $1.25 < z < 1.75$ bin.

in prep; Smail et al., in prep) as outlined in Cirasuolo et al. (2010). We use the distribution in each redshift bin (higher redshift bins indicated in Figure 2.8) to estimate the fraction of galaxies incorrectly reassigned from one redshift bin to another. For simplicity two categories were adopted: 'catastrophic' errors were defined as those with $\delta z > 0.25$, while others are classified as 'normal'. In the absence of catastrophic errors we expect $> 99.9\%$ of galaxies to show $\delta z < 0.25$ at $z \sim 1$ (Cirasuolo et al. 2010). The resulting fractions were then randomly applied to the full sample, shifting galaxies into new bins to simulate the effect of photometric redshift errors ('normal' and 'catastrophic').

This was repeated 100 times per redshift bin. Results are displayed for the redshift bins $0.75 < z < 1.25$ (Fig. 2.9) and $1.25 < z < 1.75$ (Fig. 2.10). These simulations demonstrate that photometric redshift errors tend to dilute the distinction between the red and blue populations rather than introduce fake differences. The resulting additional sources of error in galaxy density are comparable to the errors on the mean displayed previously. Only in highest redshift bin ($z > 1.75$) do the simulated populations introduce significant extra scatter (not shown). Given these findings, and the lack of spectroscopic redshifts at $z \sim 2$, we urge caution in interpreting our preliminary results in this highest redshift bin. At lower redshifts, however, the environmental differences appear robust.

Noting that we have only 97 spectroscopic redshifts in the redshift bin $1.25 < z < 1.75$ (with 64 between $1.25 < z_{photo} < 1.75$), where environmental differences appear to be very significant, we ran additional simulations using only half of the spectroscopic sample. The results were very similar to Figure 2.10, indicating that we are not suffering from low number statistics.

As an additional test, we conduct further Monte Carlo simulations to investigate the effects of contamination of the blue galaxies by the red population and vice versa. These simulations were motivated by the worry that incorrect redshifts may inevitably lead to errors in the resulting restframe $(U - B)$ colours. We adopt an

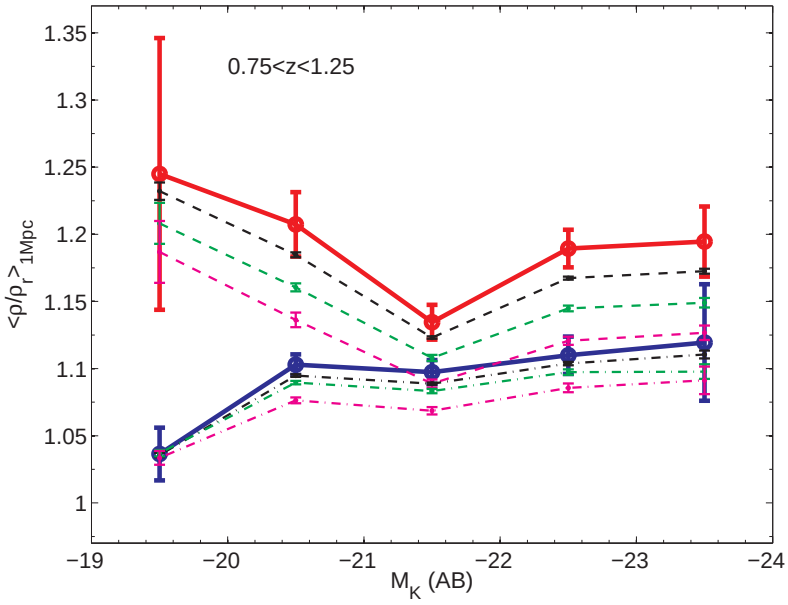

Figure 2.11. The results of Monte Carlo simulations based on the extreme scenario in which all incorrectly assigned photometric redshifts lead to blue galaxies being incorrectly classified as red, and vice versa. The original measures of environment for red galaxies and blue galaxies as a function of luminosity are shown as thick red and blue lines. Black dashed (dot-dashed) lines show the results of Monte Carlo simulations for the red (blue) populations respectively. The corresponding green and magenta lines illustrate the influence of doubling and tripling the number of incorrectly assigned galaxies.

extreme approach by simulating 100% misclassification, using the contaminating fractions outlined above but moving only blue galaxies into the red sample and vice versa. We find that these simulations have the effect of diluting the environment for both red and blue simulations, but once again are insufficient to influence any of the results previously presented. To investigate further, the contaminating fractions are artificially increased to double and triple the maximal contamination indicated by spectroscopic redshifts. These only serve to further reduce the average galaxy densities. Results for the $0.75 < z < 1.25$ bin are illustrated in Figure 2.11, and similar results are found for all other redshift bins.

We conclude that photometric redshift errors (including catastrophic errors) have only served to dilute the differences in environment, but an unrealistic proportion of misclassified galaxies are required to significantly influence our primary findings.

2.4 Conclusions

In this paper we have presented a study of the environment of over 33,000 K-band selected galaxies between $0.25 < z < 2.25$. We have used a simple measurement of projected galaxy overdensities to study the environments of galaxies divided into red and blue based on rest frame $(U - B)$ colours, as well as using 'passive' and 'star-forming' galaxies from template fitting. We attempt to quantify the effects of cosmic variance, photometric redshift errors and flux-limit biases on the resulting environmental measurements. We find the following principal results:

1. We find a strong relationship between rest-frame $(U - B)$ colour and galaxy

environment to $z \sim 1.5$, with red galaxies residing in significantly denser environments than blue galaxies on scales below 1Mpc. These results are robust to the effects of field variance, flux-limit biases and photometric redshift errors. The environments appear indistinguishable by $z \sim 2$, but the current lack of spectroscopic redshifts at this epoch does not allow a robust test of this tantalising signal at present. However other groups have seen similar results (for e.g. Tadaki et al. (2010) and we will investigate this further in Chapter 6.

2. Selecting 'passive' and 'star-forming' galaxies using template fitting yields consistent results, with the passive subset occupying slightly denser environments than the global red population at all epochs. We conclude that the passive subset of the red galaxies are responsible for the enhanced environments compared to blue galaxies.

3. On small scales (< 0.5 Mpc) we find evidence for a positive correlation between galaxy K-band luminosity (a good proxy for stellar mass) and local density. This trend is particularly clear for star-forming and blue galaxies, with the most luminous blue galaxies at $z \sim 1-2$ showing average environments comparable to passive red galaxies. These findings appear in very good agreement with the findings of Cooper et al. (2007) at $z \sim 1$. These results are consistent with the identification of high-z galaxies in transition to the red sequence in the densest environments.

Chapter 3

Galaxy Properties in Different Environments up to $z \sim 3$ in the GOODS NICMOS Survey

3.1 Introduction

In this chapter I used the data from the GOODS NICMOS Survey (GNS) to calculate the environments of the galaxies at redshifts upto $z \sim 3$. Much of this chapter is taken from Grützbauch et al. (2011), which I wrote jointly with the first author and for which I performed the environments calculations and subsequent Monte Carlo simulations which form the basis of the paper.

The UDS (Data Release 3) with over 33,000 galaxies and large, contiguous field is well suited to studying environments up to $z \sim 2$. However to measure local densities at higher redshifts requires a much deeper survey. The GOODS NICMOS Survey uses the Hubble Space Telescope to reach the imaging depth necessary to conduct this study up to a redshift of $z \sim 3$. The limiting magnitude of the GNS at 5σ is H_{AB} = 26.8 whereas for the UDS, which is selected in the K-band, is at $K_{AB} = 23.7$ (H_{AB} = 23.5). The GNS covers a smaller, disjointed region with a total area of about 45 arcmin^2 (Conselice et al. 2011) compared to a 0.63 deg^{2}contiguous field for the UDS. However due to the differences between space-based and ground-based imaging the resolution of the GNS is higher ($\sim$0.1 $''$/pixel) compared to 0.1342 $''$/pixel for the UDS. This combined with the deeper imaging means that the environments study can be extended to higher redshift.

3.2 Survey Description

The GOODS NICMOS Survey (GNS) is a 180 orbit Hubble Space Telescope programme using the NICMOS-3 near infrared camera. Each of the 60 pointings is centred on a massive galaxy ($M_* > 10^{11}\ M_\odot$) in the redshift range $1.7 < z < 3$, selected by their optical-to-infrared colours (see Conselice et al. 2011) from the GOODS (Great Observatories Origins Deep Survey) fields (Dickinson et al. 2003). GOODS has good multiwavelength coverage from X-rays with Chandra, XMM-Newton, optical with Hubble Space Telescope (HST-ACS) to the infrared with Spitzer IRAC and MIPS. This is supplemented with spectroscopic data from the Very Large Telescope (VLT) VIMOS and FORS2 spectrographs for the GOODS South field and DEIMOS

at the Keck Observatory for the GOODS North. A full description of the GNS survey as well as the target selection is given in Conselice et al. (2011).

The photometric redshifts were obtained using the $BVizH$ photometric data and two different methods: χ^2 minimisation with HYPERZ (Bolzonella et al. 2000) and a Bayesian approach using BPZ (Benítez 2000). HYPERZ uses synthetic spectra constructed with the Bruzual & Charlot evolutionary code (Bruzual A. & Charlot 1993) to represent the galaxies found in the local universe. Five template spectra are utilised to correspond to the E, Sa, Sc and Im spectra types and a single burst model, using the reddening law taken from Calzetti et al. (2000). This then outputs the best fit redshift, corresponding probability and best fit parameters including spectral type, age, metallicity, A_V and secondary solutions.

The BPZ approach on the other hand uses empirical templates and uses additional information about the likelihood of a certain combination of parameters, or priors. In this work the prior is the distribution of magnitudes for the different morphological types as a function of redshift, obtained from the Hubble Deep Field North (HDF-N) Data. So not only does it do something similar to HYPERZ but it also takes into account how likely it would be to find a galaxy of a given spectral type and magnitude at that redshift.

The photometric redshifts from both methods were compared to the spectroscopic redshifts available in the GOODS fields to assess their reliability. The redshifts for the GOODS-N were compiled by Barger et al. (2008) and the redshifts in the GOODS-S were taken from FIREWORKS (Wuyts et al. 2008). When matched to the GNS catalogue with a $2''$ matching radius this gave 906 spectroscopic redshifts in total with a mean separation of 0.41 ± 0.06 arcsec in the GOODS-N and 0.13 ± 0.05 arcsec in the GOODS-S. Figure 3.1 shows both sets of photometric redshifts measured with HYPERZ (left) and BPZ (right) against the spectroscopic redshifts, with higher probability z_{phot} circled in red. They are both in good agreement but HYPERZ is slightly better at dealing with the outliers by giving them a lower probability. For HYPERZ the high probability photometric redshifts ($P > 95\%$), have a median offset of $\langle\Delta z/(1+z)\rangle = 0.033$, with a scatter of $\sigma_{\Delta z/(1+z)} = 0.045$ (356 out of 906 galaxies with $P > 95\%$). With all the redshifts regardless of their probability, the median offset decreases to $\langle\Delta z/(1+z)\rangle = 0.011$, while the scatter rises slightly to $\sigma_{\Delta z/(1+z)} = 0.061$. BPZ gives comparable offsets, but slightly higher scatters: $\langle\Delta z/(1+z)\rangle = 0.026$ with a scatter of $\sigma_{\Delta z/(1+z)} = 0.058$ for high probability redshifts (792 out of 906) and $\langle\Delta z/(1+z)\rangle = 0.030$ and $\sigma_{\Delta z/(1+z)} = 0.064$ for all galaxies. BPZ identifies more redshifts with a high probability than HYPERZ, however, they are not necessarily better than the low probability redshifts, as shown by the comparable scatter.

Figure 3.2 shows the dependence of $\Delta z/(1+z) \equiv (z_{spec} - z_{phot})/(1+z_{spec})$ on H-band magnitude. HYPERZ and BPZ results are plotted as circles and crosses respectively. Only galaxies in the redshift range of $1.5 \leq z \leq 3$ are shown in this plot. The median offset and RMS scatter are computed in each magnitude bin and are plotted as big symbols (with corresponding errorbars) in red for HYPERZ and in blue for BPZ. The figure shows the slightly better performance of HYPERZ, which is also visible in the fraction of catastrophic outliers with $|\Delta z/(1+z)| > 0.3$ (bottom panel of Figure 3.2). The redshift error is stable up to faint magnitudes of $H_{AB} \sim 24$, as is the fraction of outliers. Overall, the performance of HYPERZ is slightly better than that of BPZ. For this reason the photometric redshifts from

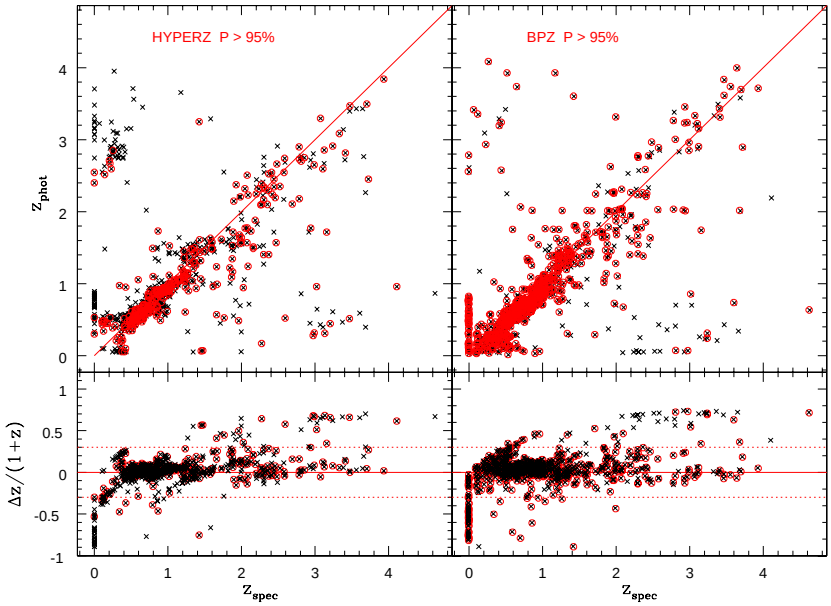

Figure 3.1. Reliability of photometric redshifts: *Top panels:* photometric vs. spectroscopic redshifts using HYPERZ (left) and BPZ (right). Photometric redshifts with a high probability of $P > 95\%$ are circled in red. *Bottom panels:* $\Delta z/(1+z)$ dependent on redshift. Black symbols show all redshifts, red symbols high probability redshifts only. The dashed lines show the limit for catastrophic outliers at $|\Delta z/(1+z)| > 0.3$.

HYPERZ are used throughout the rest of this chapter.

The performance of HYPERZ at different redshifts is important to look at, both at low redshift ($z < 1.5$) and in the redshift range of $1.5 \leq z \leq 3$, which is the redshift range of the galaxy sample we use in this study. The photometric redshift errors and outlier fraction are computed separately in the low and high redshift sample. These values are then used in the Monte Carlo simulations described in Section 3.2.3 to account for the photometric redshift errors. For the high redshift sample we obtain an average offset $\langle \Delta z/(1+z) \rangle = 0.06$ and a RMS of $\sigma_{\Delta z/(1+z)} = 0.10$, with a fraction of catastrophic outliers of 20%. As above catastrophic outliers are defined as galaxies with $|\Delta z/(1+z)| > 0.3$, which corresponds to ~ 3 times the RMS scatter. Galaxies below $z = 1.5$ show a slightly lower, but still comparable scatter of $\sigma_{\Delta z/(1+z)} = 0.08$, however the outlier fraction decreases dramatically to only $\sim 2\%$.

3.2.1 Stellar Masses and Rest Frame $(U - B)$ Colours and Colour Selection

Instead of using K-band magnitudes as a stellar mass proxy (as in other chapters) we here calculate the stellar masses directly. The stellar masses and rest-frame colours are measured by multicolour stellar population fitting techniques, based on the same catalogue used for the photometric redshift determination. A large set of synthetic spectral energy distributions (SEDs) are constructed from the stellar population models of Bruzual & Charlot (2003) (hereafter BC03), assuming a Salpeter initial mass function. The star formation history is characterised by an exponentially declining model with various ages, metallicities and dust extinctions. These models are parametrised by an age of the onset of star formation, and by an e-folding time

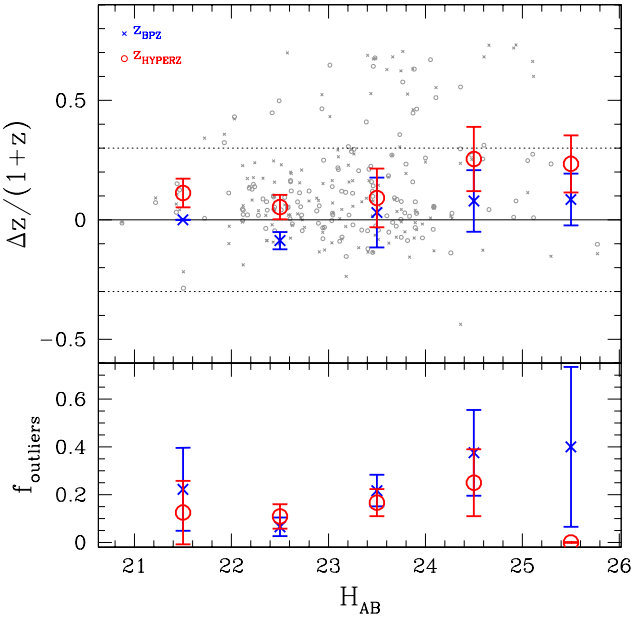

Figure 3.2. Dependence of $\Delta z/(1+z)$ on magnitude. *Top panel:* $\Delta z/(1+z)$ vs. H-band magnitude for HYPERZ (red circles) and BPZ (blue crosses). Median values in each magnitude bin (bin size of 1 mag) are plotted as big symbols with errorbars representing the scatter in each bin. The dashed lines show the limit for catastrophic outliers at $|\Delta z/(1+z)| > 0.3$. *Bottom panel:* fraction of catastrophic outliers $|\Delta z/(1+z)| > 0.3$ as a function of H-band magnitude. Only galaxies in the redshift range $1.5 < z < 3$ are used in this plot.

such that $\mathrm{SFR(t)} \sim \mathrm{SFR}_0 \times \mathrm{e}^{-\frac{t}{\tau}}$, where the values of τ are randomly selected from a range between 0.01 and 10 Gyr, while the age of the onset of star formation ranges from 0 to 10 Gyr. The metallicity ranges from 0.0001 to 0.05 (BC03), and the dust content is parametrised by τ_v, the effective V-band optical depth for which we use values $\tau_\mathrm{v} = 0.0, 0.5, 1, 2$. The model SEDs are then fit to the observed photometric datapoints of each galaxy using a Bayesian approach. For each galaxy a likelihood distribution for the stellar mass, age and absolute magnitude at all star formation histories described above is computed. The rest-frame $(U-B)$ colours are then computed, since the wavelength range of the U and B bands is covered best by the observed optical and H bands. The peak of the likelihood distribution is then adopted as the galaxy's stellar mass and absolute U- and B-band magnitude, while the uncertainty of these values is given by the width of the distribution. The rest-frame $(U-B)$ colours are obtained by subtracting the two absolute magnitudes. While parameters such as age, e-folding time and metallicity are not accurately fit due to various degeneracies, the stellar masses and colours are robust. From the width of the probability distributions we determine typical errors for our stellar masses of 0.2 dex. There are additional uncertainties from the choice of the IMF and due to photometric errors, resulting in a total random error of our stellar masses of $\sim$0.3 dex, roughly a factor of two.

To study the different populations of red and blue galaxies we split the sample by their location in the colour-magnitude diagram. Due to the low number of objects and even fewer spectroscopic redshifts the division is chosen by evolving the red

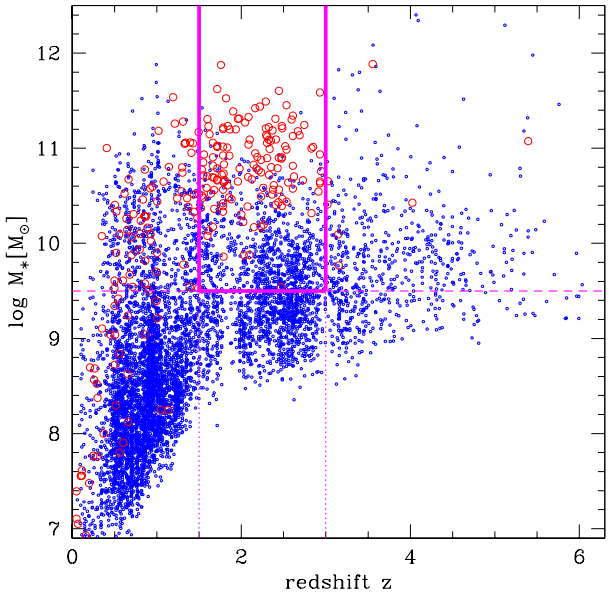

Figure 3.3. Distribution of stellar masses ($\log M_*$) with redshift z for red galaxies (red big circles) and blue galaxies (blue small circles). The adopted completeness limit of $\log M_* = 9.5 M_\odot$ (at $z = 3$) is shown as dashed line. The limits of the redshift range used in this study are marked with dotted lines. The resulting window in redshift and stellar mass containing the galaxy sample we use in the following is given by the thick solid lines.

sequence found at lower redshift back in time. We take the red sequence of galaxies in the DEEP2 redshift survey at $z \sim 1$ (Willmer et al. 2006), converted to AB magnitudes:

$$(U - B) = -0.032\ (M_B + 21.52) + 1.284 \tag{3.1}$$

and evolve it back with redshift according to van Dokkum & Franx (2001). The separation between the narrow red sequence and the diffuse blue cloud was found to be present up to at least $z \sim 1.4$ (Willmer et al. 2006), with a separation between the two populations of 0.25 magnitudes. We adopt this colour limit of 0.25 mag blueward of the red sequence to separate between red and blue galaxies. In Figure 3.3 shows the stellar mass versus redshift z for blue and red galaxies, as defined above. The dashed magenta line shows the completeness limit of $\log M_* = 9.5$ at the upper redshift limit of $z = 3$ (dotted line) adopted in this study. This completeness limit is derived from the 5σ depth and mass-to-light ratio for a maximally old stellar population at the redshift limit of this study ($z = 3$). The completeness of blue galaxies at a given stellar mass is higher than for red galaxies, which are more difficult to detect at high z due to the shape of their SED. However, since we want to compare red and blue galaxy populations we have to make sure that our sample is not biased towards blue galaxies at high z, and we therefore use the conservative stellar mass cut of $\log M_* = 9.5$. The colour dependent completeness limits and mass functions of red and blue galaxies in the GNS are further investigated by Mortlock et al. (2011), who find similar completeness limits. The final galaxy catalogue used comprises of 1289 galaxies down to a stellar mass of $\log M_* = 9.5$ within the redshift range of $1.5 < z < 3$.

3.2.2 Environmental Measurements

A different environmental measure is utilised for calculating the GNS environments than is used for the UDS galaxies. This was largely due to the smaller sample size and due to the limitations of the GNS field. Edge effects are important in the GNS as each pointing is about 500 h^{-1} kpc in diameter, at $z = 1.5 - 3$ and the survey does not have a contiguous survey area. This means that for some galaxies not all of the area within the aperture used for the local density measure is fully covered by the survey. This is especially problematic for isolated galaxies on non-overlapping pointings. However due to the techniques discussed below these effects will be taken into account as carefully as possible.

As for the UDS we calculated the environments using both the apertures method and the nearest neighbour method. Here, for both methods we use a redshift interval of $\Delta z = \pm 0.25$ to minimise contamination from foreground and background galaxies. Spectroscopic redshifts are used if avaliable. For the apertures method, the number of galaxies in the redshift interval and 500 h^{-1} kpc radius of each galaxy were calculated, giving a surface density, Σ_{AP} in galaxies per Mpc^2. To try to account for the problems imposed by the survey edges we renormalise by the number of image pixels with in the aperture. To account for the variation with redshift due to depth and resolution we then take a further step. We divide each surface density by the median density of all the galaxies in $\Delta z = \pm 0.25$ centred on each galaxy. This gives a relative overdensity

$$(1 + \rho) = \frac{\Sigma_{AP}}{N_{pixels}} \Big/ \left\langle \frac{\Sigma_{AP}}{N_{pixels}} \right\rangle_{\Delta z} \tag{3.2}$$

where ρ is the overdensity, the density relative to the median density, where the angled brackets denote the median density. Taking the log of $(1 + \rho)$ divides the sample in under- and over-dense environments relative to the average density, where by definition $\log\ (1 + \rho) = 0$.

For the nearest neighbour method we calculated the distance to the third (D_3), fifth (D_5) and seventh (D_7) nearest galaxy. The number of neighbours that you calculate to depends on the size and mass of the structure that you are interested in. A high n (as used in, for example Dressler 1980) is suited for high-mass, high density areas like clusters but in low density regions it measures the distance to other structures. For this reason a lower n is more suited to measuring the local galaxy density. However the overall choice does not change the resulting densities significantly (Cooper et al. 2005). To take account of the edges, a similar method was used as for the aperture densities. Firstly the distance to the third, fifth and seventh nearest neighbours was calculated within $\Delta z = \pm 0.25$ for each galaxy. The number of image pixels within the area πD_n^2 ($N_{pixels}(D_n)$) was calculated to approximate the area covered around each galaxy, giving the surface density as $\Sigma_n = n/N_{pixels}(D_n)$. This was then normalised by the median value in each redshift slice, $\langle \Sigma_n \rangle_\Delta z$ for each galaxy such that the overdensity (δ_n) is given by:

$$(1 + \delta_n) = \frac{\Sigma_n}{\langle \Sigma_n \rangle_{\Delta z}} \tag{3.3}$$

with $\log\ (1 + \delta_n) < 0$ being underdense and $\log\ (1 + \delta_n) > 0$ being overdense environments.

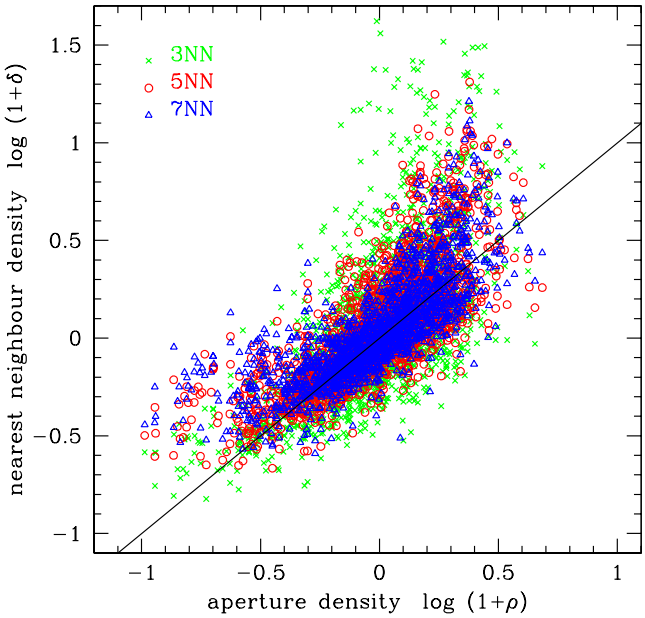

Figure 3.4. Comparison of the nearest neighbour densities, $\log\ (1+\delta_n)$ versus $\log\ (1+\rho)$ with green crosses ($n=3$), red circles ($n=5$) and blue triangles ($n=7$).

3.2.3 Investigating the Effect of Photometric Redshift Errors

The main source of uncertainty in calculating the environments is in the uncertainties of the photometric redshifts (e.g. Cooper et al. 2005) which leads to blurring along the line of sight. To estimate this effect we perform a set of Monte Carlo simulations by randomising the photometric redshift input according to the $\Delta z/(1+z)$ error and including a fraction of outliers and recalculating the local density. For this purpose we take the typical photometric redshift error $\Delta z/(1+z)=0.10$ in our redshift range of $1.5\leq z\leq 3$ (see Section 3.2 and Figure 3.1) and assume a Gaussian distribution of errors, where the width of the distribution σ corresponds to $\Delta z/(1+z)$. For each galaxy a random value is selected within this distribution, which is then added to the measured photo-z. Catastrophic outliers are accounted for by randomly adding much larger offsets to the original redshifts of the percentage of galaxies corresponding to the fraction of catastrophic outliers, which is calculated from the comparison with secure spectroscopic redshifts. Galaxies with $|\Delta z/(1+z)|>0.3$ are treated as catastrophic outliers here. The offsets are randomly picked from the interval $0.3<\Delta z/(1+z)<1$ and added or subtracted from the original redshift.

Once this was done the new randomised photometric redshifts were put through the code and the densities measured. This was done 100 times, giving 100 density estimates. This Monte Carlo technique allows us to account for the average redshift uncertainty within the redshift range of interest as well as for the respective fraction of catastrophic outliers. The local density error for each individual galaxy is then given by the standard deviation of all 100 Monte Carlo runs. These individual errors are then averaged to obtain an average uncertainty of the respective local density estimator. This gives the average uncertainties as: $\Delta\log\ (1+\delta_3)=0.24$, $\Delta\log\ (1+\delta_5)=0.21$, $\Delta\log\ (1+\delta_7)=0.18$ for the three nearest neighbour densities and $\Delta\log\ (1+\rho)=0.20$ for the aperture density. The Monte Carlo simulations are

discussed further in the results section and are shown in the respective figures.

3.3 Results

Here we first discuss the correlations between the local galaxy densities [log $(1+\delta_n)$ and log $(1+\rho)$] and then investigate the colour-density relation, additionally looking at the differences between galaxy properties in high- and low-density quartiles. We focus on the redshift range of $1.5 \leq z \leq 3$, which has a reasonable surveyed volume and stellar mass completeness down to log $M_* = 9.5$.

3.3.1 Local Galaxy Densities

Two different methods were used to calculate the local galaxy densities (see section 3.2.2) fixed aperture density, $(1+\rho)$, and the 3^{rd}, 5^{th} and 7^{th} nearest neighbour density, $(1+\delta_n)$. The three nearest neighbour densities are plotted against the aperture densities in Figure 3.4. They are in good overall agreement with an average spread of $\sim 0.2-0.3$ dex, with the green crosses, red circles and blue triangles showing the $n = 3, 5$ and 7 respectively. Whilst they are on average in good agreement it also illustrates that on different scales they are not necessarily comparable due to the different sensitivities of the n values. At the low density end for example the density estimates of the 3rd, 5th and 7th nearest neighbours are quite different as the higher values will be tracing the density on much large scales rather than on the local scales in which we are interested. The n^{th} nearest neighbour density is a better tracer of the extremes in local density since it uses an adaptive area and therefore is sensitive to galaxy concentrations at very small scales, that the fixed aperture cannot probe. The lower the value of n, the more sensitive the density measure is to local galaxy concentrations on small scales. For this reason the 3^{rd} nearest neighbour density log $(1+\delta_3)$ is used for the remainder of this work.

3.3.2 The Colour-Density Relation

Here we investigate the colour-density relation in three redshift bins: $1.5 < z < 2$, $2 < z < 2.5$ and $2.5 < z < 3$.

Figure 3.5 shows the relation between $(U-B)$ colour (top row) and the fraction of blue and red galaxies (bottom row) as a function of relative overdensity log $(1+\delta_3)$. We do not find a significant correlation between colour and overdensity in the data. There is, however, a possible trend for a higher fraction of blue galaxies ($\sim 100\%$) at the highest overdensities (log $(1+\delta_3) > 0.8$) at all redshifts, whereas the blue fraction at intermediate and low densities is around 80-90%. A trend of a lack of red galaxies at high overdensities is visible, but is not significant due to the low number of galaxies at high overdensities.

To further check the significance of the higher fraction of blue galaxies at high overdensities we used Monte Carlo (MC) simulations. We performed 100 Monte Carlo runs based on the randomised photometric redshift input as described in Section 3.2.3. The scatter between the individual runs represents the uncertainties in the local densities due to the photometric redshift error. The results from the MC simulations are shown in Figure 3.6. The average colour (bottom panel), fraction of blue galaxies (middle panel) and stellar mass (top panel) as a function of local density in each Monte Carlo run is plotted. The large scatter in the high density end due to the low number of galaxies in extreme overdensities becomes visible.

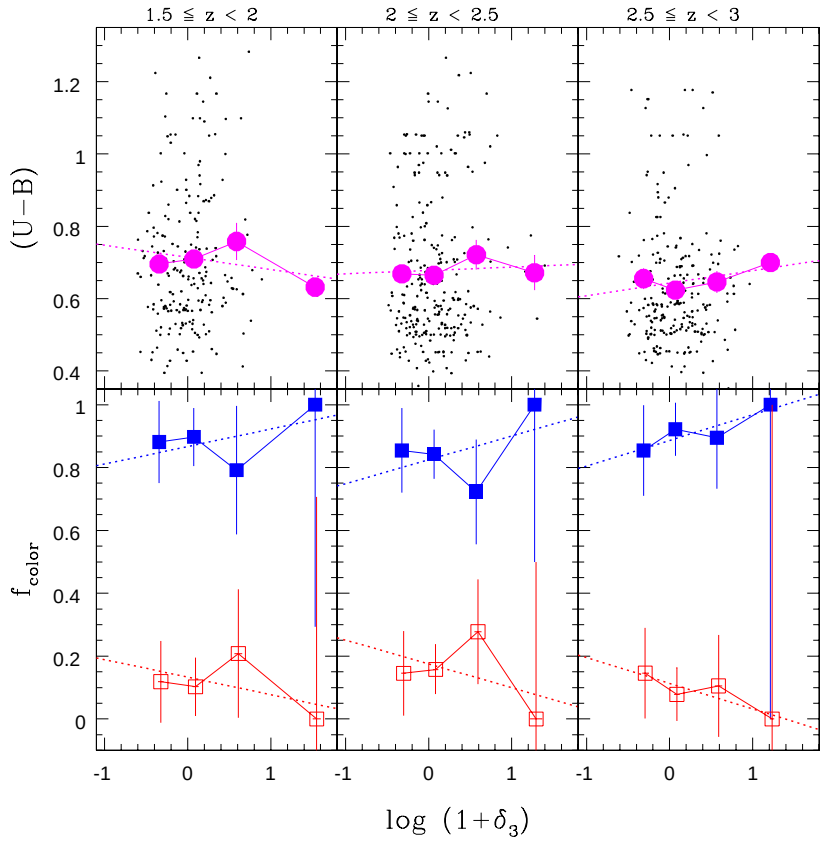

Figure 3.5. Colour-density relation in three redshift ranges for the whole mass range (log $M_* > 9.5$). The redshift bins are indicated on top of each panel. The rest frame $(U-B)$ colour and fraction of red and blue galaxies as a function of local density log $(1+\delta_3)$. The mean and error of the mean in each bin of local density is overplotted in magenta (big symbols). Blue fractions are plotted as blue solid squares, red fractions as red open squares. The dotted lines show least squares fits to the data.

At all the redshifts studied above densities of log $(1+\delta_3) > 0.8$ the vast majority of MC runs show a blue fraction of 100%, whereas at lower densities the blue fractions vary between 85-90%. The average and RMS of all Monte Carlo runs at log $(1+\delta_3) < 0.8$ shows an average blue fraction of 85±2% in the two lower z bins and 90±2% in the high z bin. At the highest densities the average blue fraction is 95±13%, however, the distribution of average blue fractions at the highest overdensities is not Gaussian and the standard deviation does not represent the distribution adequately. To estimate the probability that the difference between high and low density is caused by chance, we consider the number of times a Monte Carlo run gives a blue fraction at the highest densities which is lower than the average value plus 3σ at lower densities. In the lowest redshift bin about 90% of Monte Carlo runs result in $f_{blue} > 90\%$, giving a $\sim$ 10% probability that the difference between highest and lower densities is caused by chance. The intermediate and high redshift bin have a probability of $\sim$ 15%.

We conclude that the colour-density relation at $z > 1.5$ is either very weak or does not exist at all. If a trend with local density persists it must be very minor, with a variation of the average $(U-B)$ colours of less than $\sim$0.1 magnitudes between relative local densities that differ by a factor of 100. There could be an environ-

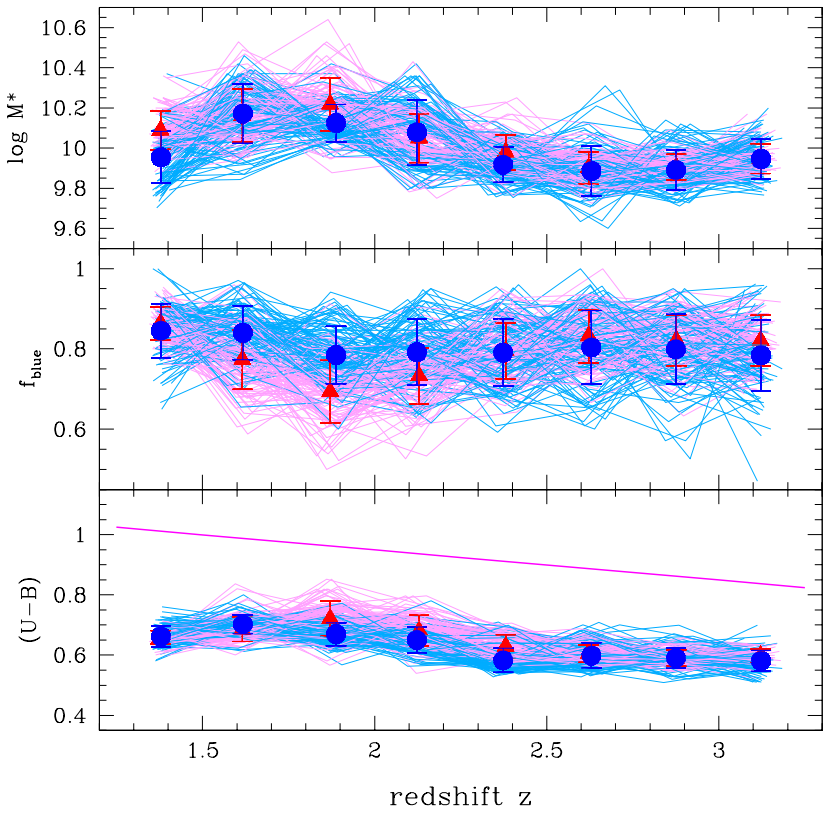

Figure 3.6. Colour, blue fraction, and stellar mass in high and low density quartiles (log $(1+\delta_3)$). The high quartile corresponds to log $(1+\delta_3) > 0.22$, the low quartile to log $(1+\delta_3) < -0.23$. Each line is the result of one Monte Carlo run. The average and RMS of all Monte Carlo runs in each redshift slice of 0.25 is overplotted as big symbols. Red lines and triangles correspond to the high density quartile, while blue lines and circles correspond to the low quartile of the density distribution. The magenta straight line in the bottom panel indicates the distinction between red and blue galaxies at $M_B = -21.5$, calculated from evolving back the red sequence as described in Section 3.2.1.

mental influence on the blue fractions of galaxies in the most extreme overdense environments. This difference in blue fractions amounts to about 10% and is not detectable at a statistically significant level with the low number of galaxies in our sample located at the highest overdensities (33 galaxies at log $(1+\delta_3) > 0.8$ between $1.5 < z < 3$).

3.3.3 Galaxy Properties in the High and Low Density Quartiles

In the following we compare the properties of galaxies in low and high density quartiles, i.e. 25% of galaxies at each extreme respectively. The high quartile of local density corresponds to galaxies located in overdense regions of log $(1+\delta_3) > 0.22$, while the low quartile corresponds to underdense regions of log $(1+\delta_3) < -0.23$. After dividing the sample into low and high quartiles a Kolmogorov-Smirnov (K-S) test between the different quartiles is used to investigate the statistical difference of the two subsamples. To increase the number statistics we consider the full redshift range of our sample at $1.5 \leq z \leq 3$, instead of binning into the three redshift

ranges used above. The stellar mass limit is kept at log $M_* = 9.5$, as above. The K-S test gives the probability $P_{low,high}$ that the galaxy properties in the low and high quartile come from the same parent distribution. We find that galaxies in the low and high quartile of the local density distribution have marginally different colours ($P_{low,high} = 0.05$, i.e. $\sim 2\sigma$) but not statistically different stellar masses ($P_{low,high} = 0.12$, i.e. $< 2\sigma$). We further investigate the reliability of this 2σ difference by using the Monte Carlo simulations described in Section 3.2.3

In Figure 3.6 we plot galaxy properties in low and high density quartiles as a function of redshift. The results of each of the 100 Monte Carlo runs are plotted as a single line. Figure 3.6 shows the median $(U-B)$ colour, blue fraction and median stellar mass in each redshift bin ($\Delta z = 0.25$) in the low quartile (blue) and high quartile (magenta) of local densities. The average of all Monte Carlo runs in each redshift slice is overplotted as big symbols, blue circles for the low quartile and red triangles for the high quartile.

Figure 3.6 shows that there is barely any difference in colour, blue fraction or stellar mass between the low and high quartile of local density. We may see evidence for a weak trend of a lower blue fraction at high densities emerging at $z < 2.2$, as well as a correspondent peak in the average stellar mass in the high density quartile, which is probably responsible for the positive correlation found from the K-S test on the data described above. However, we conclude that we lack the number statistics to reliably confirm the presence of a difference between low and high density quartile and that our data is consistent with there being no difference.

Note however that the lack of a clear separation between the low and high density quartiles does not contradict the results from the colour-density relation in Section 3.3.2, where we possibly see evidence for a higher blue fraction in the most overdense environments above log $(1+\delta_3) \sim 0.8$. The high density quartile includes all galaxies at densities above log $(1+\delta_3) \sim 0.2$ and does not comprise of the most extreme overdensities only, in which we see the higher blue fraction. Since there is no relation with local density at densities below log $(1+\delta_3) \sim 0.8$, we do not see any difference between the colours of galaxies in the low and high quartile of the density distribution.

We conclude that in the redshift range of $1.5 \leq z \leq 3$ the highest local overdensities (log $(1+\delta_3) > 0.8$, i.e., an overdensity of roughly a factor of 5, possibly show a higher fraction of blue galaxies. At densities below log $(1+\delta_3) \sim 0.8$ there is no correlation between rest-frame colours or fraction of blue galaxies with local density. This finding is different from the colour density relation found at lower redshifts (up to $z \sim 1.4$), where higher density environments show a higher fraction of red galaxies (e.g. Cooper et al. 2006; Cucciati et al. 2006; Pannella et al. 2009; Grützbauch et al. 2010).

In Chapter 2 we looked at the local colour-density relation, with redder galaxies located in regions of higher local density up to a redshift of $z \sim 1.75$. Above this redshift the distinction between the environments of red and blue galaxies can not be confirmed at a statistically significant level. Chapter 2 also hints at a possible reversal of the colour-density relation at even higher redshift, however, the currently available UDS Data Release (DR3) does not allow for reliable conclusions at high z. The results we present in this study are consistent with extrapolating the results of Chapter 2, suggesting a gradual disappearance of the colour-density relation with redshift and a possible reversal of the colour-density relation at the most extreme

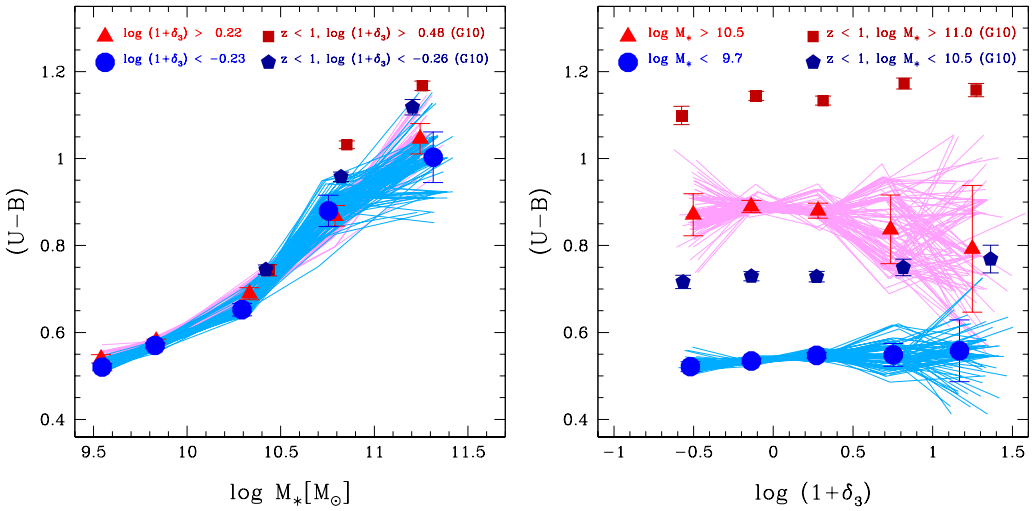

Figure 3.7. Colour-stellar mass and colour density relation in low and high density and mass quartiles, respectively, over the whole redshift range $1.5 < z < 3$. Left panel: colour-stellar mass relation in high (red) and low (blue) local density quartiles. Right panel: colour-density relation in high (red) and low (blue) stellar mass quartiles. This figure shows the results of the Monte Carlo simulations (see text). The mean and RMS of all Monte Carlo runs in bins of stellar mass (left panel) and local density (right panel) are overplotted as big symbols: red triangles for the high quartile and blue circles for the low quartile. The average data points are from a sample of Grützbauch et al. (2010) covering the redshift range $0.4 < z < 1$. These are plotted for comparison as big red squares (high quartile) and blue pentagons (low quartile) respectively.

overdensities at $z > 1.5$. We shall look at this further in Chapter 6.

3.3.4 Is the Colour-Density Relation Caused by Variations in Stellar Mass?

Recent studies at intermediate redshift ($z \sim 1$, e.g. Cooper et al. 2007; Grützbauch et al. 2010) have suggested that the observed colour-density relation is mainly caused by the strong correlation between rest-frame colour and stellar mass. This also requires the presence of a stellar mass-density relation, such that higher mass galaxies are preferentially located in regions of higher overdensity. We indeed find a weak trend for this behaviour, emerging at $z < 1.8$, at a significance of $\sim 2\sigma$.

Another question is if the higher fraction of blue galaxies in high overdensities (see Section 3.3.2) is due to a trend in stellar mass. To answer this question we investigate the colour-stellar mass relation and the colour-density relation in quartiles of local density and stellar mass respectively.

The left panel of Figure 3.7 shows the colour-stellar mass relation in high and low density quartiles and the right panel shows the colour-density relation in high and low stellar mass quartiles. The same high and low quartiles of local density and stellar mass are used as described above (Section 3.3.3). As in Figure 3.6 we plot the results of each Monte Carlo run as well as the average and RMS of all runs instead of the measured data. The whole redshift range of $1.5 < z < 3$ is shown in Figure 3.7.

To compare our result with the colour-density and colour-stellar mass relations at lower redshift we use the data of (Grützbauch et al. 2010, hereafter G10). This

sample is based on a deep near-infrared survey (the Palomar Observatory Wide-field Infrared (POWIR) survey, Conselice et al. 2008) and spectroscopic redshifts from the DEEP2 redshift survey (Davis et al. 2003). The local densities and colours are measured in a similar way as in the present study. We split the G10 sample into high and low density quartiles and stellar mass quartiles as described above. The data covers the redshift range $0.4 < z < 1$. The median $(U-B)$ colours of this sample are overplotted as big symbols: dark red boxes are used for the high quartile and dark blue pentagons for the low quartile of the POWIR sample data-points respectively.

The left panel of Figure 3.7 shows that the strong correlation between $(U-B)$ and log M_* is present in both, high (red) and low (blue) density quartiles. The relation is very similar in both density quartiles. The colour-stellar mass relation at lower redshifts of $0.4 < z < 1$ (squares and pentagons in Figure 3.7) is remarkably similar to the colour-stellar mass relation in the GNS data (triangles and circles), with a similar slope and a slightly larger colour difference between low and high local density quartiles ($\Delta(U-B) \sim 0.15$ mag). At the high mass end low z galaxies have redder average colours than galaxies of the same stellar mass at high z. The colours of log $M_* \sim 10.5$ galaxies at $1.5 < z < 3$ are indistinguishable from the colours of similar mass galaxies at $0.4 < z < 1$.

The right panel of Figure 3.7 shows the correlation between colour and local density for galaxies in the low and high stellar mass quartile. A clear colour offset between low- and high-mass galaxies of $\Delta(U-B) \sim 0.2-0.3$ mag is present at all densities. Interestingly, there is a trend that mean colours of galaxies in the high-mass quartile are bluer at higher overdensities (log $(1+\delta_3) > 0.5$) than at low and average local densities. For galaxies in the low-mass quartile we do not see a strong correlation between colour and local density. Combined with the results of the colour-density relation in Figure 3.5, this would point towards high-mass galaxies being responsible for the higher fraction of blue galaxies at the highest overdensities. Note however that the RMS scatter between the single Monte Carlo simulations is larger than the decrease in colour. This large spread is due to the low numbers of objects at the highest overdensities [33 galaxies at log $(1+\delta_3) > 0.8$]. The colour difference between the GNS data-points and the $z < 1$ data-points from G10 is mainly due to the differences in the stellar mass distribution in the two surveys, leading to different limits of the low and high quartiles. The GNS reaches much lower stellar masses down to log $M_* \sim 9.5$, whereas the completeness limit of the POWIR survey is log $M_* \sim 10.25$. Additionally, the G10 sample has a larger number of high mass galaxies with log $M_* > 11$ than the GNS sample, leading to redder average colours, as expected from the colour-mass relation.

If the colour-density relation we see for high-mass galaxies is real, then it is reversed with respect to what is found at lower and intermediate redshifts up to $z \sim 0.85$, where galaxies in higher local densities tend to be redder (see e.g.. Kauffmann et al. 2004; Patel et al. 2009; Grützbauch et al. 2010). Figure 3.7 shows that the high and low mass quartiles of the G10 sample (up to $z \sim 1$) show a weak correlation between colour and local density, such that the average colour increases with higher local density. On the other hand, it was argued by some studies that the colour-density relation and colour-SFR relation at $z \sim 1$ might be reversed (Elbaz et al. 2007; Cooper et al. 2008). Note, however, that Patel et al. (2009) argue that the reversed SFR-density relation (where galaxies in denser environments have higher SFRs) is mainly driven by starforming *low*-mass galaxies, whereas our data indicate that the reversed colour-density relation is due to on average bluer *high-*

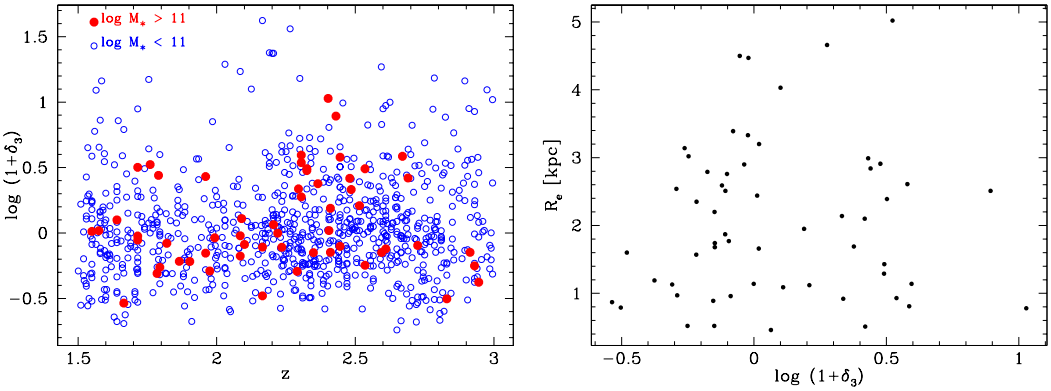

Figure 3.8. Environments of most massive galaxies (log $M_* > 11$). Left panel: local density log $(1 + \delta_3)$ for the full sample (blue open circles) and the most massive galaxies (red dots) as a function of redshift. Right panel: effective radii in kpc as a function of relative overdensity log $(1 + \delta_3)$.

mass galaxies. In other words, we see a lack of red high-mass galaxies in regions of high relative overdensities. The on average bluer high-mass galaxies, however, are on average still redder than low-mass galaxies at comparable densities, but bluer than their high-mass counterparts at average and low local densities. Note that the bluer colour of high mass galaxies does not necessarily imply that there is more ongoing star formation in these galaxies, but that there is possibly less dust-attenuated star formation at highest overdensities. Massive galaxies in our sample show an overall very high dust content relative to low mass galaxies (Bauer et al. submitted). The behaviour of the SFR-density relation using dust corrected star formation rates from Bauer et al. (submitted) will be investigated in a forthcoming paper.

3.3.5 The Environment of the Most Massive Galaxies and its Relation to Galaxy Sizes

In the following we investigate how, and if, the environments of the most massive galaxies (log $M_* > 11$) differ from the rest of the galaxy population and if there is a correlation between local density and galaxy size. The subsample of massive galaxies for which a size measurement is available comprises 57 galaxies from the selection of massive galaxies in the GOODS fields on which the GNS pointings were centred (Conselice et al. 2011). The measured local densities of those galaxies are very reliable since they are in the centre of their respective pointing and should not be affected by survey edges, as discussed in Section 3.2.2. The left panel of Figure 3.8 plots the local densities of the massive galaxy sample (red dots) and the rest of the sample (blue circles) against redshift. A K-S test between the two subsamples shows that they are not statistically different.

To examine a possible environmental effect on the sizes of massive galaxies in our sample, we use the galaxies' effective radii measured by Buitrago et al. (2008). They argue that the measured effective radii of these massive galaxies are consistently smaller than the typical effective radii of galaxies of comparable stellar mass in the local universe. Different scenarios have been proposed to account for this size evolution, one of them being dry merging. In this scenario repeated minor merging of gas poor galaxies would not trigger the formation of new stars, but could possibly increase the size of a galaxy by dynamical friction and the injection of angular

momentum (Naab et al. 2009). This scenario would then suggest a connection between galaxy sizes and local density, since it requires the presence of numerous companions for galaxies to grow in size. The right panel of Figure 3.8 shows the effective radii R_e of massive galaxies as a function of their local density log $(1+\delta_3)$. A Spearman Rank correlation test finds no significant correlation between R_e and local density, although all galaxies in the most underdense environments (log $(1+\delta_3) < -0.2$) have small R_e (< 3 kpc). However, due to the small number of objects in our sample this effect probably arises by chance.

The lack of a correlation between galaxy size and local density is probably due to the different effects that the environment might have on galaxies. High local densities may not only increase the size of a galaxy via minor mergers as suggested by e.g. Naab et al. (2009) they may also tidally truncate galaxies (see e.g. Rubin et al. 1988), although tidal truncation is most effective on low-mass galaxies. Another possibility is that the size evolution, does not occur through frequent minor merging of satellite galaxies, but through internal processes like AGN feedback (Fan et al. 2008).

3.4 Summary and Conclusions

In this section we investigate the influence of local density on galaxy rest-frame colour and the fraction of blue galaxies at redshifts between $1.5 < z < 3$ based on observational data from a deep HST H-band data of the GOODS NICMOS Survey (GNS), reaching a stellar mass completeness limit of $M_* = 10^{9.5}$ at $z = 3$. We find the following results:

1. The strong colour-stellar mass relation is very similar across all local environments and does not evolve strongly with redshift. The colour-stellar mass relation at $1.5 < z < 3$ has a slope similar to the relation at lower redshift ($0.4 < z < 1$), which also has a larger offset in colour between low and high local densities. At the same stellar mass, massive galaxies at high redshifts ($1.5 < z < 3$) are bluer than at low redshifts ($0.4 < z < 1$), whereas the average colour of lower mass galaxies (log $M_* \sim 10.5$) does not vary strongly with redshift.

2. We do not find a strong influence of local environment on galaxy colours. If the colour-density relation persists at $z > 1.5$ it must be very weak. We determine an upper limit to the possible change in the average $(U - B)$ colour between high and low relative densities of ~ 0.1 magnitudes. However, the most overdense regions (~ 5 times overdense) may be populated by a higher fraction of blue galaxies than average and underdense regions. The difference in f_{blue} is $\sim 10\%$. We find possible evidence that this higher blue fractions at the most extreme overdensities could be caused by a lack of massive red galaxies at the highest local densities.

3. We do not find a significant correlation between galaxy sizes (effective radii) and relative overdensity, although we do not find any galaxies with large effective radii ($R_e > 3$kpc) at very low densities (log $(1+\delta_3) < -0.2$). However,

this might be due to the small number of objects we find in low density environments and is probably a chance effect.

To summarise, this work suggests that stellar mass is the most important factor in determining the colours of galaxies in the early universe up to $z \sim 3$. Local density might have a small additional effect, but only at the most extreme overdensities, which are populated by a higher fraction of blue galaxies. These results are consistent with studies at lower and intermediate redshift that suggest a gradual weakening of the environmental influence with higher redshift, as also seen in Chapter 2. A possible interpretation for this is that the environmental processes that alter the properties of galaxies are proceeding slowly over cosmic time. Some of the most influential high density environments like galaxy clusters are still in the process of being build-up at $z > 1.5$ and cannot yet change galaxy colours via, for example, ram pressure stripping or strangulation.

If the trend for higher blue fractions at the highest local densities is real, it would suggest that we are witnessing the epoch of high star formation in more massive galaxies and that the local environment contributes to this epoch by triggering SF through galaxy interactions. Note however, that this result is tentative due to the limited volume of the GNS survey.

To confirm this result on a statistically significant level needs a large area IR survey. The latest UDS data release (DR8) with its significantly improved depth compared to the DR3 (Chapter 2) and greater area compared to the GNS will enable us to draw more reliable conclusions (see Chapter 6). The DR8 imaging data will be complimented by a large spectroscopic survey (UDSz) designed to yield a large number of secure spectroscopic redshifts in the crucial redshift range $z > 1$, which I will describe in the following Chapter.

Chapter 4

The UDS Spectroscopic Survey (UDSz)

In this chapter I describe the reduction of data from an ESO Large Programme designed to obtain spectra for ∼3500 galaxies in the UDS field. My responsibility was to reduce 90 hours of multi-object spectroscopy obtained using the VIMOS instrument. This involved using bias, flat and lamp frames to clean, extract and calibrate the data. Standard stars were also used to photometrically calibrate the spectra. Exposures were then stacked to increase the singal to noise. This had to be done for each of the four quadrants in each of the eight VIMOS pointings and in some cases we had to get them reobserved. I then looked through all of the spectra to determine the redshifts and to flag any issues or interesting objects. These spectra increase the reliability of the photo-zs for the UDS survey and allows better environment measures to be calculated (see Chapter 6). The spectra discussed here are also the spectra utilised in Chapter 5.

4.1 Introduction

The VIsible Multi-Object Spectrograph (VIMOS) is installed on the ESO VLT in the Atacama Desert, northern Chile. It is a 4 channel ("quadrant") instrument covering ∼7× 8 arcmin^2, with ∼ 218 arcmin^2, per field of view ("pointing") with a pixel scale of 0.205"pixel^{-1} (Le Fèvre et al. 2005). The arrangement of these quadrants and pointings for the Spectroscopic Ultra Deep Survey (UDSz) and the grisms used are shown in Figure 4.1 and Table 4.1 respectively. The survey was an ESO Large Programme service mode run 180.A-0776(B) with a total of 235 hours of time allocated to it (PI:Almaini). The VIMOS data were taken between 2nd November 2007 and 27th December 2008 on ESO-VLT-U3.

As outlined in previous chapters, deep infrared surveys are vital to obtain an accurate census of the distant Universe, without the strong selection biases that plague optically-selected surveys. The UKIDSS Ultra Deep Survey (UDS) is already the deepest wide-field (0.8 deg^2) near-infrared survey ever conducted. The aim of the UDSz ESO Large Programme was to obtain spectra and redshifts for a representative sample of ∼3500 K-selected galaxies from the UDS, using the combination of the VIMOS and FORS2 spectrographs. The aims were to obtain accurate mass and luminosity functions to chart the build-up of the galaxy populations, to study galaxy clustering and large-scale structure, and also to conduct a detailed study of the influence of environment on galaxy evolution at $z > 1$ (the primary topic of this thesis). Further science goals include the identification of high-z groups and

clusters, the identification of X-ray and submillimetre sources and the confirmation of candidate galaxies at $z > 5$. The spectra themselves will also allow a detailed study of the evolution of galaxy stellar populations with cosmic time, e.g. by studying star-formation rates from [OII], passivity with the 4000Å break as well as many others (see Chapter 5 for some more examples). Finally the spectra will also be vital for a more accurate calibration of photometric redshifts, which will enable a wide range of science projects. Prior to this project there were only a few hundred confirmed galaxies known in the UDS at $z > 1$, and virtually no spectra at $z > 2$.

The UDSz programme was designed to target ∼3500 galaxies across the UDS field, pre-selected with photometric redshifts to lie at $z_{phot} > 1$. This criterion was introduced since our primary science goals are to study galaxy evolution at $z > 1$ where previous optically-selected studies (e.g. VVDS, DEEP2) are known to be highly biased. Our strategy targets roughly 1/6 of the galaxies in the UDS field to a limit of K_{AB} <23. A random control sample of ∼500 galaxies were also targeted at $z_{phot} < 1$ in order to assess the biases in our photometric selection (this sample grew to ∼1000 during mask design, due to the relatively low surface density of primary targets). The survey uses two instruments; VIMOS was used to target the optically-brighter systems (i' <24 or V <25) while FORS2 was used for fainter, redder systems (V >24 and i' <25), with deliberate overlap in the selection criteria. A pragmatic decision was taken to exclude galaxies with $i' > 25$ since these systems were considered unlikely to yield a reasonable fraction of reliable redshifts in a K-selected sample to the depths probed. This optical cut excludes approximately 25% of galaxies with $z_{phot} > 1$. The next generation of multi-object infrared spectographs (e.g. FMOS on Subaru, KMOS on VLT or EMIR at the Gran Telescopio CANARIAS (GTC)) may be required to obtain spectroscopy of these objects.
The eight VIMOS pointings are shown in Figure 4.1, tiling the region of the UDS field with the best optical Subaru imaging. At each pointing we obtained 4.5 hours exposure with the LR blue grism and 2.6 hours with LR red, which we combined to obtain the maximum spectral coverage for the majority of galaxies (spanning 3700-9500Å). Each VIMOS position targets ∼360 galaxies (∼90 per quadrant). The 20 FORS2 fields are coincident with the central part of the VIMOS tile. At each FORS2 position we obtained 5.5 hours exposure using the 300I grism, observing typically 35-40 faint galaxies per field. The data from FORS2 were reduced and the redshifts were determined by a team in Edinburgh composed of Henry Pearce, Ross McLure, Michele Cirasuolo and Jim Dunlop.

The target selection and mask design was performed by Omar Almaini for both instruments. A brief outline is given below. Full details will be presented in the survey definition paper (Almaini et al., in preparation). Targets were initially selected from the UDS DR1 K-band image to a limit of $K_{AB} < 23$. This was based on a 'DR1+' catalogue tailor-made for the redshift survey, using tighter Sextractor deblending parameters to avoid the blending of close galaxy pairs. From this catalogue 1471 objects with existing secure redshifts were first excluded, most of which lie at $z < 1$. Objects lying in masked regions of the K-band and Subaru images were also removed. Obvious stars were then excluded, with care taken to avoid biasing the redshift survey against quasars or highly compact galaxies; 'stars' had to simultaneously lie in the stellar locus of a BzK diagram, a separate KX diagram (V-J vs J-K) and in the stellar locus of an aperture magnitude plot (comparing magnitudes

Grism	λ Range (nm)	Resolution	Dispersion (Å/pixel)
LR blue	370-670	180	5.3
LR red	550-950	210	7.3

Table 4.1. Table showing the VIMOS grisms used

in 0.7 and 1.5 arcsec diameter apertures). These criteria excluded 1771 robust stars to a limit of $K_{AB} < 20$. Combined, these cuts left 53,874 K-selected galaxies from which to select targets.

After obtaining pre-imaging observations, VIMOS and FORS2 masks were then prepared using the VMMPS (VIMOS Mask Preparation Software) and FIMS (FORS Instrument Mask Simulator) software packages provided by ESO. The majority of targets were not visible in the pre-images, as expected, so a careful astrometric transform was required to convert the RA, Dec of the targets to x,y in the mask frame. This transformation was performed using typically 50-100 stars or compact objects present in both the K-band and VIMOS images to a typical accuracy of $0.10 - 0.15$ arcsec RMS across each VIMOS quadrant. In the case of FORS2 we obtained more accurate slit positions by relying on the internal K-band astrometry of the UDS image, with carefully selected guide stars, so pre-images were only used to perform final checks. After allocating suitable guide stars, primary targets with $z_{phot} > 1$ were used for the first round of mask preparation using photometric redshifts provided by Michele Cirasuolo (see Cirasuolo et al. 2007). In addition to the primary targets, several dozen high priority targets were also assigned slits, including 36 candidate galaxies at $z > 6$ (FORS2 only), a few dozen X-ray sources and SCUBA submillimetre galaxies and a number of optically-variable objects. Remaining slits were placed on secondary targets in the field with $z_{phot} < 1$. A few hundred radio galaxies and bright 24μm sources were also added as higher priority secondary targets. Approximately 40% of FORS2 galaxies were also forced onto VIMOS LR-Blue masks, to extend the wavelength coverage for at least a sample of these faint targets (e.g. to catch potential emission lines). These objects were not observed with VIMOS LR-Red, which allowed a few hundred extra 'red-only' targets to be observed with VIMOS in vacated slit locations. In total, we targeted 2,881 objects with VIMOS and 802 with FORS2.

4.2 Reduction

The data was reduced using a piece of software called the VIMOS Interactive Pipeline and Graphical Interface (VIPGI) (http://cosmos.iasf-milano.inaf.it/pandora/vipgi.html). The software is capable of handling Imaging, Multi Object Spectrograph (MOS) data and Integral-field Unit (IFU) data, but we are only concerned with the MOS reduction here. There are many steps involved in sorting and calibrating the data in VIPGI and these are discussed in detail in Appendix A.1. Here I will only give a brief summary of each step:

1. Unpacking - VIPGI unpacks all of the data into their quadrant and pointing. It also categorises them according to the headers. This separates out stan-

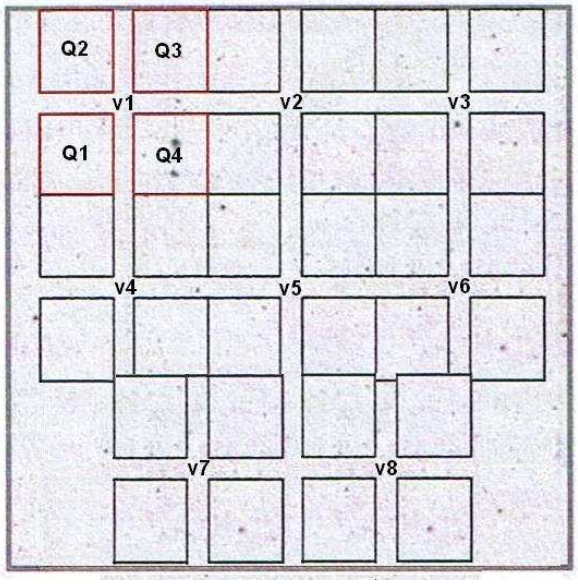

Figure 4.1. Shows the arrangement of the VIMOS quadrants and pointings which covers $\sim$0.8 deg^2 of the UDS field. Twenty FORS2 pointings are also arranged across the field in a similar pattern to above but for clarity they are not shown here.

dard stars, science frames and calibration files in the GUI, making it easier to organise the large quantity of data.

2. Standard Stars - For each observation a standard star is used to flux calibrate the spectra. This is done to ensure that the CCD response and conditions can be corrected for on a night-by-night basis.

3. Flat and Lamp files - The first guesses as to where the spectra are located and a first guess at the wavelength calibration are stored in the header of the files at the time of observation. The first step is to check these and to apply the final solution to the flat and lamp files. The flat files are used to extract the spectra and the lamp files are used to wavelength calibrate the final spectra. It is important at this stage to ensure that the wavelength calibration is good ($\sim$ 1/7 th of a pixel) so that the spectra are combined properly (see Table 4.2 for our values). Each science frame is combined with its own flat, lamp and standard star to ensure an accurate extraction, wavelength calibration and flux calibration for each observation. This helps to improve the combining of the spectra and guarantees that any signal is kept as high as possible. For both the LR Red and LR Blue we obtained an average RMS of $\sim$1.1Å in the wavelength calibration. A raw science frame from pointing one, quadrant one in the blue is shown in Figure 4.2, showing the slits, some objects and star slits used to align the mask.

4. Final Reduction - Three steps of reduction are then done. The first subtracts the bias frames, trims the images and appends the extraction tables to the images. The next step detects the objects on the slits, extracts and flux calibrates the spectra and calculates the sky background. The final step combines all of the observations for each OB into a file with all the 1D, 2D and target

information. In the LR Red fifteen to twenty well exposed spectra are then selected to apply an atmospheric correction to the spectra.

4.2.1 Cleaning, Combining and Identifying the Spectra

1D and 2D spectra can subsequently be extracted from VIPGI. The zeroth order lines and other known skylines were removed from the 1Ds. The zeroth orders are bright lines introduced from adjacent spectra by the grism. Sébastien Foucaud removed the skylines using an IRAF task as these appear at well known positions. Emma Bradshaw removed the zeroth orders using MATLAB code to predict in which spectra and at what wavelength they would appear knowing the widths and lengths of the slits and the position of the primary object. Some of the secondary objects may still have remaining zeroth orders as these weren't possible to remove with this information. These were identified manually during redshift determination. The red and blue parts of each galaxy spectrum is observed separately due to the design of the instrument. So the objects in the red and blue were then matched by Sébastien Foucaud and Will Hartley using the LR Blue as the base. It was known which slit corresponded to which DR1+ ID for any given VIMOS field/quadrant. Within these the objects were matched by the VIMOS x and y co-ordinates given in the headers of the output files. From these the x-offsets between the blue and the red were computed and for those that had offsets greater than 0 and less than 25 pixels the median offset was calculated ($\sim$0.67pix). The objects were then re-matched with this median offset in x applied. Those positioned on the y-axis at zero were labelled as fakes as inspection had shown this to be the case. Objects were then considered matched if they were within 1 pixel of each other after applying the offset.

If both a red and blue spectrum were avaliable then these were stitched together by Emma Bradshaw using IRAF so that the redshift determination could utilise the whole wavelength coverage. This procedure cut the blue spectra between 3600Å and 6700Å and the red spectra between 5800Å and 9000Å with an overlap region defined between 6000-6600Å. The spectra were resampled to ensure no information was lost and the mean S/N in the overlap region was used to weight the spectra in the IRAF SCOMBINE package (with scale set to mean). The 2D spectra were combined using the information from above and IRAF's IMCOMBINE package using an average combination, WCS offsets and resampling the red spectrum to match that of the blue using IRAF - magnify. The targeted object and secondaries were identified and finding charts were made using this data (http://www.nottingham.ac.uk/astronomy/UDSz/index.php).

For the majority of VIMOS slits multiple objects were identified with VMMPS, and in many cases the identification of the primary target was found to be ambiguous. This was due to slight shifts in the positions of targets relative to the expected x, y coordinates from the mask design. Primary targets were therefore identified iteratively using code written by Omar Almaini. After transforming CCD x, y positions to the mask coordinate system, a cross-correlation was first performed between expected mask positions and the objects identified by VIMOS. This yielded an offset (typically 1-2 VIMOS pixels) between object location and the predictions from mask design. After applying this correction, a second match was performed to identify the correct primary targets. Estimated RA, DEC values for the secondary

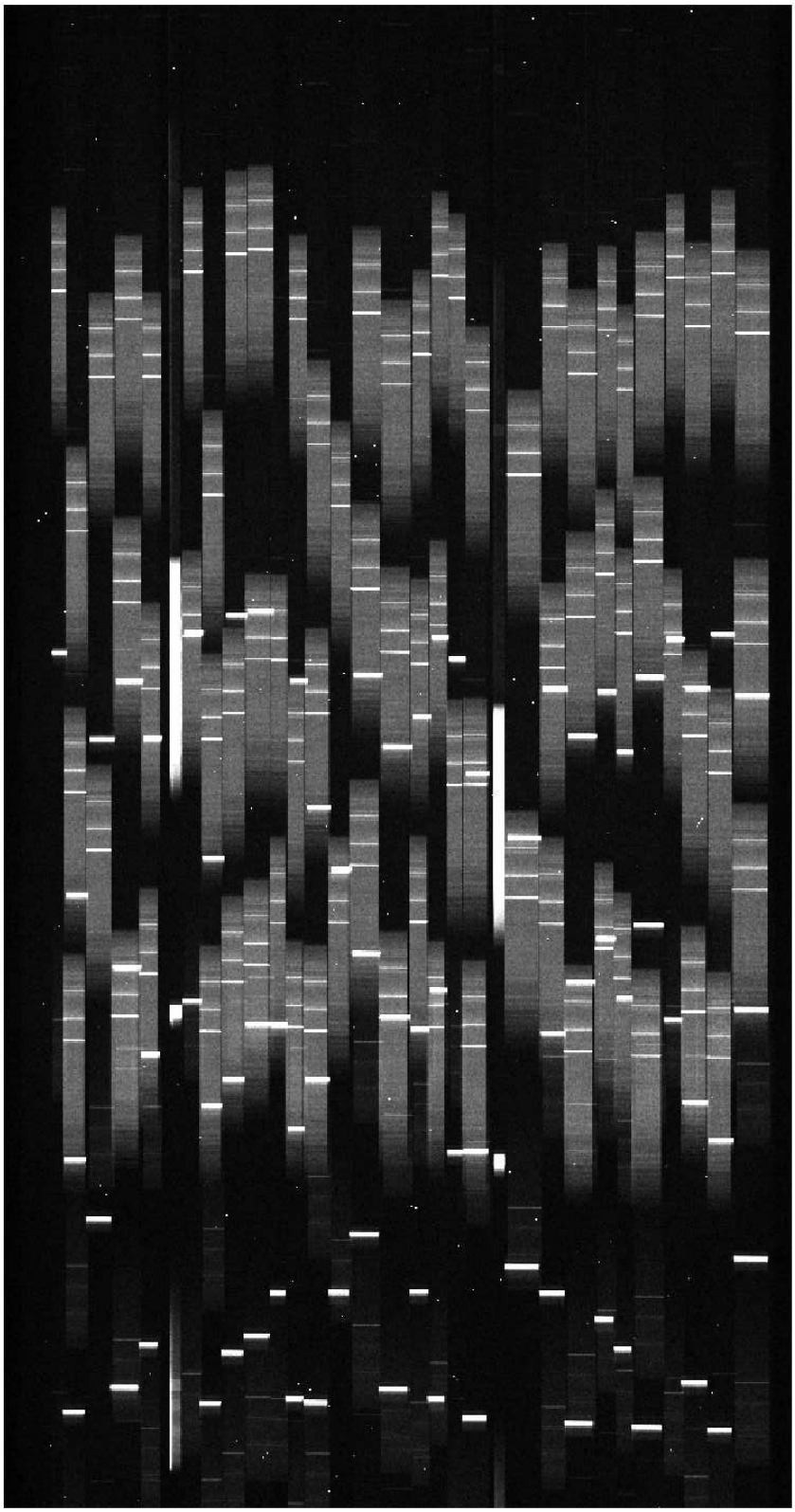

Figure 4.2. A raw science image from VIMOS pointing one, quadrant one (v1Q1) in the blue

targets were then obtained based on their offsets from the nearest primary.

4.3 Redshifts

To obtain the redshifts two packages were used, SGNAPS and EZ both written by the same team that wrote VPGI at the IASF (Istituto di Astrofisica Spaziale e Fisica Cosmica). SGNAPS allows both the 1D and 2D spectra to be viewed simultaneously and to mark any emission or absorption features that can be used to get a redshift by hand. A table of important lines employed in determining redshifts are shown in Table 4.3. SGNAPS determines the redshift by fitting single emission lines which allows the exact centre of the line to be determined to try to increase the accuracy of the redshift. Where possible this was done on the [OII] line to ensure a fair comparison of the redshifts. EZ on the other hand allows the determination of redshifts with templates and cross-correlation which can then be checked by hand in the GUI.

The redshift determination was done in two parts. A first pass through the spectra was done to obtain as many flag 3s (secure redshifts) as possible (see Table 4.4), with the specific aim of building up our own spectral templates to be used in a more careful second pass. The first pass also served as a useful training exercise for our team in redshift determination. This was done by dividing the spectra between the group such that each spectra was seen by at least two people and all of the red/blue spectra were looked at by me. If people agreed on the redshift to ± 0.01 and either one or both of them had put it as a flag 3 then the object was used. If there was disagreement then the spectrum was looked at as a group. Various templates were then made out of these reliable, well exposed spectra. These well exposed spectra were divided into subsets, for example red and blue, passive and star forming and high and low redshift, so that they would cover the full range of the objects that we have. These were consequently combined in IRAF with scombine and loaded into EZ to aid the second, full pass of the spectra. Emma Bradshaw and I then used EZ, the templates and knowledge that we had gained from the first pass to visually inspect all of the spectra again. The templates that we had created proved to be very useful, as they matched the spectra well and allowed an easy determination of tough, redshift desert objects to be made. These were more useful than the templates that we already had as ours had the same response and systematics as the data. For more information on the use of EZ see Appendix A.1.4.

For the second pass the flagging scheme was altered (see Table 4.5) to make the flagging clearer, to aid simple flagging of AGN and to properly flag the flag 9 objects from the first pass. The flags and redshifts from Emma and I were then looked at by Will to make the final decision on which redshift and flag were correct. This was done such that: If both flags were ≥ 3 and the redshift disagreement was less than 0.01 then my flag and redshift were used. If both our flags were <3, with at least one flag>0, then the higher flagged redshift was taken. For flags that we agreed were 1 or 2, my redshift was taken. If the flags were both 0 then these were ignored. For every other possible combination (for example different redshifts with flags≥ 3; objects with flags≥ 0 and one flag ≥ 3) the objects were inspected and re-determined with the full knowledge of the previous determinations. Some sample spectra from the reduction are shown in Figures 4.3 and 4.4, showing good flag 4s and average

Red Field/Quad	S/N	Ave RMS (Å)		Blue Field/Quad	S/N	Ave RMS (Å)
v1 Q1	2.95	1.10		v1 Q1	1.37	1.36
v1 Q2	2.53	0.94		v1 Q2	2.16	0.78
v1 Q3	3.13	1.27		v1 Q3	2.45	0.92
v1 Q4	2.64	0.99		v1 Q4	1.56	0.97
v2 Q1	4.79	1.00		v2 Q1	2.19	0.80
v2 Q2	3.60	0.94		v2 Q2	2.01	0.77
v2 Q3	4.34	1.05		v2 Q3	1.66	1.19
v2 Q4	3.18	1.01		v2 Q4	1.64	2.80
v3 Q1	3.63	1.04		v3 Q1	2.19	0.94
v3 Q2	2.53	0.98		v3 Q2	1.72	0.80
v3 Q3	2.27	1.09		v3 Q3	2.35	0.79
v3 Q4	2.13	1.10		v3 Q4	1.66	0.84
v4 Q1	2.78	1.10		v4 Q1	2.00	0.79
v4 Q2	2.75	0.84		v4 Q2	1.61	0.95
v4 Q3	2.82	1.09		v4 Q3	2.00	0.97
v4 Q4	2.34	0.99		v4 Q4	1.33	0.87
v5 Q1	3.19	0.98		v5 Q1	2.01	0.83
v5 Q2	2.53	0.94		v5 Q2	1.92	0.79
v5 Q3	2.88	1.32		v5 Q3	1.92	0.90
v5 Q4	2.46	0.89		v5 Q4	1.56	0.83
v6 Q1	2.76	1.09		v6 Q1	2.58	0.74
v6 Q2	3.03	0.95		v6 Q2	1.82	0.78
v6 Q3	3.80	0.95		v6 Q3	2.64	0.89
v6 Q4	2.36	0.95		v6 Q4	2.32	0.84
v7 Q1	2.45	0.94		v7 Q1	2.52	0.85
v7 Q2	2.13	0.91		v7 Q2	2.20	0.86
v7 Q3	2.94	0.99		v7 Q3	2.51	0.87
v7 Q4	2.53	0.88		v7 Q4	2.21	0.97
v8 Q1	3.03	0.99		v8 Q1	2.25	1.41
v8 Q2	2.87	0.98		v8 Q2	1.59	1.18
v8 Q3	2.45	1.18		v8 Q3	2.34	0.95
v8 Q4	2.75	1.04		v8 Q4	1.98	0.86

Table 4.2. Table showing the average signal to noise and average wavelength calibration RMS of all of the pointings and quadrants in red and blue.

λ (Å)	Line		λ (Å)	Line
1215.7	Lymanα		2382.0	FeII
1240.0	NV		2586.7	FeII
1260.4	SiII		2600.0	FeII
1303.0	[OI]		2799.0	MgII
1334.5	CII		3727.5	[OII]
1397.0	SiIV		3933.7	CaK
1526.7	SiII		3969.17	CaH
1549.9	CIV		4000	Break
1670.8	AlII		4101.70	Hδ
1856.0	AlIII		4861.32	Hβ
1909.0	[CIII]		4959	[OIII]
2142.0	[NII]		5007	[OIII]
2260.0	FeII		5577	Skyline
2344.2	FeII		5892	Skyline
2374.0	FeII		$\sim$ 6300	Skyline

Table 4.3. Table showing some of the important emission and absorption lines used for redshift determination including skylines which are useful for checking the wavelength calibration

Flag	Preliminary Pass Definition
0	No idea.
1	Possible redshift but not confident.
2	Good chance that is correct but a feature doesn't look correct.
3	Very confident of redshift
9	One emission line only.

Table 4.4. Table showing the preliminary flags used in the UDSz and what they mean.

flag 3s respectively.

To check the reliability of our redshifts and to assess the overall success rates we compare the spectroscopic redshifts with the photometric redshifts from the DR3. The photometric and spectroscopic redshifts agree well (see Figure 4.5) and have a reasonable error of $\sim \langle\delta_z/(1+z)\rangle$=0.0158. For the primary objects this gives a success rate of Flag 4: 18.2%, Flag 3: 17.4%, Flag 2: 17.9% and Flag 1: 13.7%, with 35.6% being secure flags (flags $\geq$3), where the success rate is defined as the fraction of primary objects of that flag with respect to the total number of the primary objects. The redshift range between $z \sim 1.3$ where the [OII] moves out of the spectral range of the VIMOS instrument and $z \sim 2$ where the Lyα moves into the range is known as the redshift desert. This is because there are a lack of strong features in this redshift range (see Table 4.3). However we have managed to use some of the absorption features to obtain a redshift, for example the FeII complex and MgII proved very useful features in this redshift range. The use of templates also made it easier to identify these, especially for the fainter objects. Figures 4.6 and 4.8 show similar flagged data from FORS2. FORS2 used a slightly different flagging system using class A, B and B*, these flags are similar to the VIMOS flag

Flag	Final Definition
0	No idea.
1	'Good guess' (1 sigma, i.e. 30% could be wrong).
2	95% certain. Good for some science, but may be incorrect.
3	'Secure but imprecise', 99.9% certain but z not accurate.
4	'Bulletproof', 99.9% certain and accurate
+0.8	Add 0.8 if it is a AGN.

Table 4.5. Table showing the final flags used in the UDSz and what they mean.

4, 3 and 2 respectively.

4.3.1 Conclusion

Here we have presented the motivation, strategy and reduction for the ∼3500 galaxies in the UDSz K-selected redshift survey. We have outlined the steps taken in the data reduction to ensure that the data yielded as many secure redshifts as possible from this tough redshift desert region. We obtained 4679 spectra including a large fraction of secondaries over the ∼1700 arcmin^2 field of view. With template fitting using EZ and careful visual inspection we have been able to obtain a reasonable sample (∼35% of the primary objects) of reliable redshifts (flag 3 and 4) in the range $0 \leq z \leq 3.99$. Overall we obtain 2204 flagged spectra out of all the 4679 spectra, with 1534 out of the 2282 primary objects. These spectra and redshifts will be used in following chapters to determine the properties of galaxies in different environments and to improve the photometric redshifts for subsequent data releases. They will also be used by our team for a whole range of additional science goals, e.g. studying galaxy outflows, observing AGN, large-scale structure as well as many others.

In the next Chapter I use these redshifts and spectra presented in this Chapter to study how spectral measures such as the equivalent width of [OII] and the 4000Å break are affected by environment.

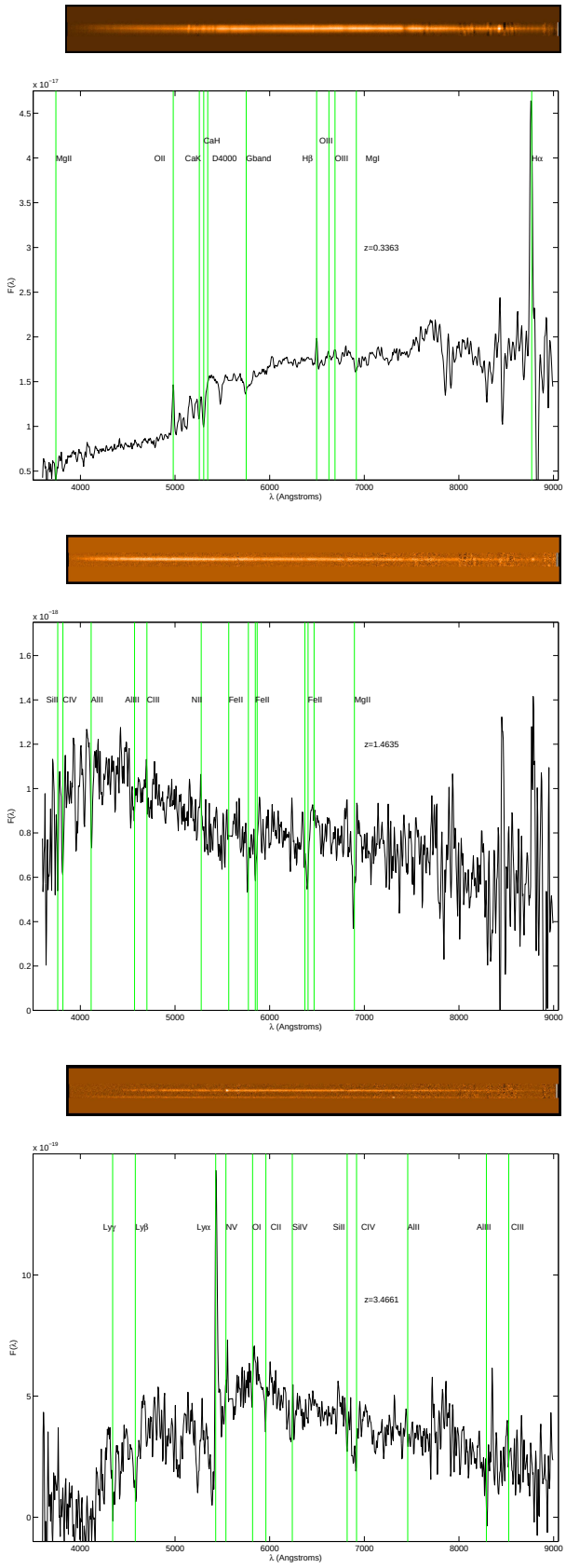

Figure 4.3. Three examples of very good flag 4 objects. With 1D and 2Ds of objects 29871 (v5Q1) $z = 0.3363$, 61380 (v3Q1) $z = 1.4635$ and 61651 (v2Q1) $z = 3.4661$.

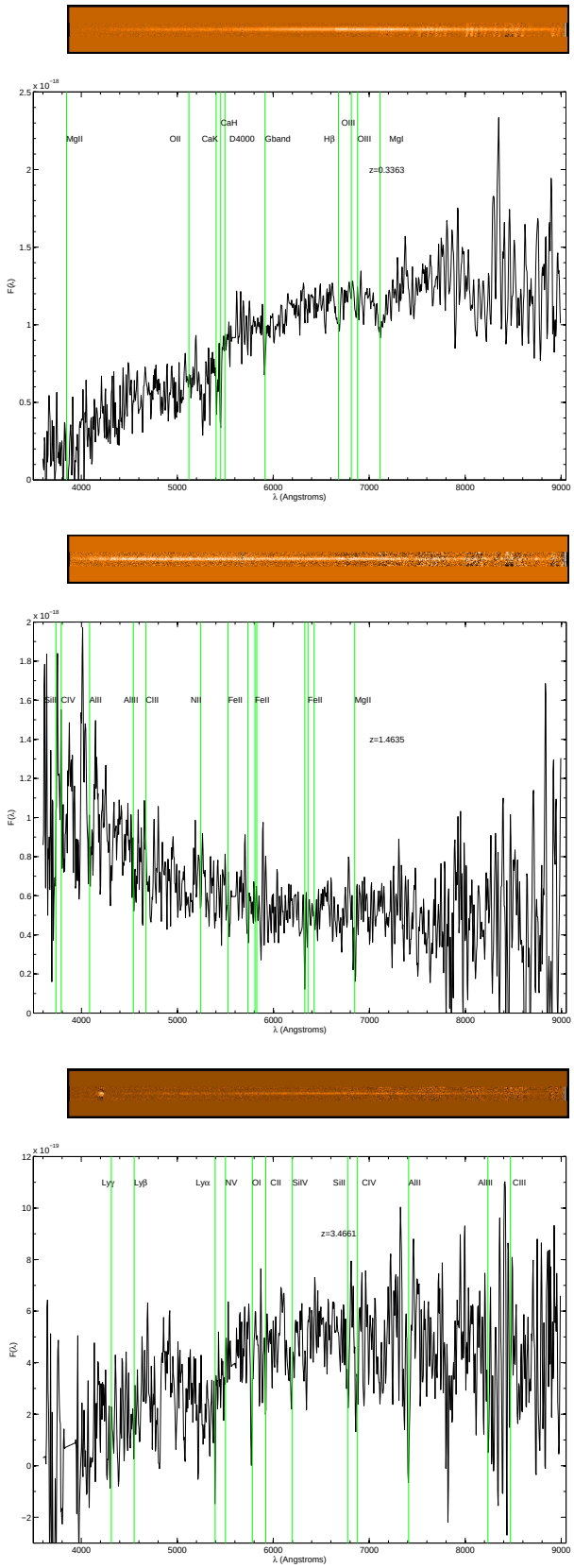

Figure 4.4. Three examples of 'typical' flag 3 objects. With 1D and 2Ds of objects 70121 (v3Q2) $z = 0.374$, 72458 (v1Q2) $z = 1.446$ and 19360 (v8Q3) $z = 3.4374$.

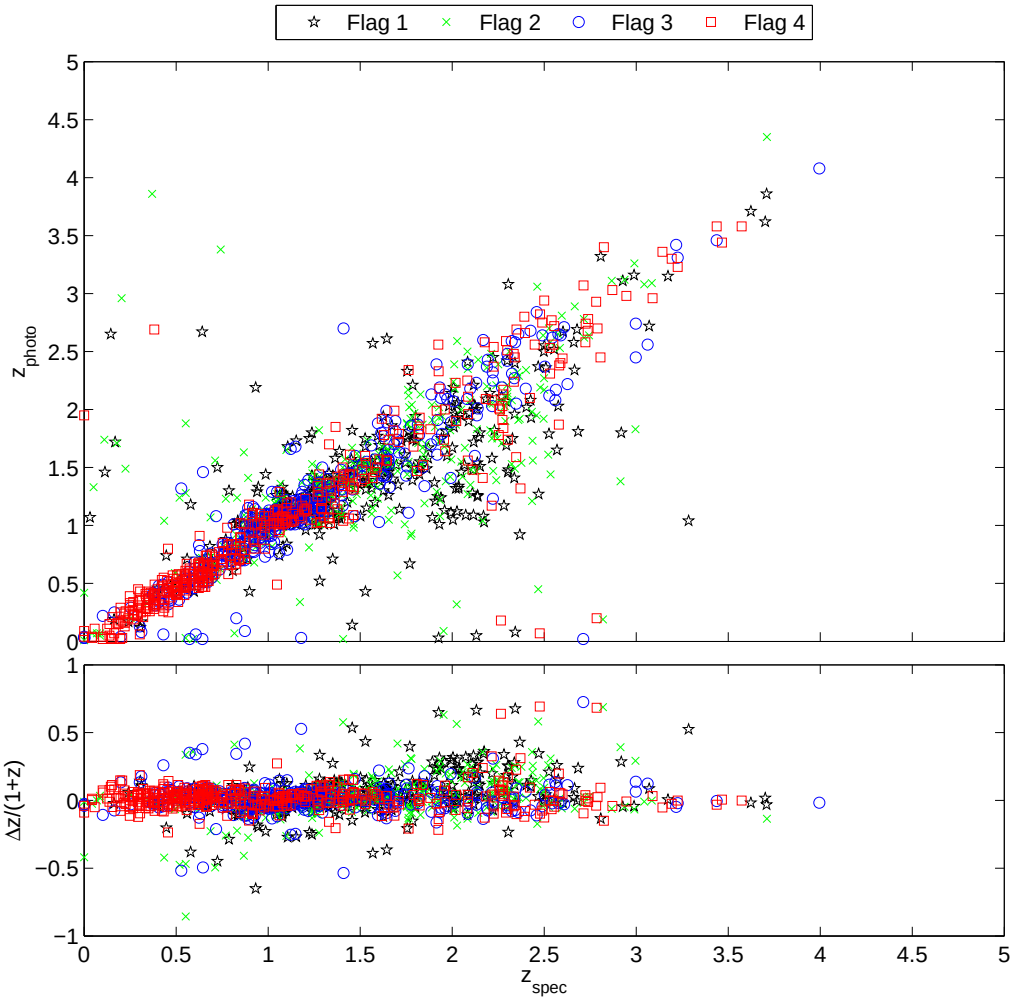

Figure 4.5. Plot of the VIMOS spectroscopic vs photometric redshifts for the primary objects, with flag 4 and 3 defined as good flags (red squares and blue circles respectively) and flag 2 and 1 defined as less secure and good guess (green cross and black star) respectively.

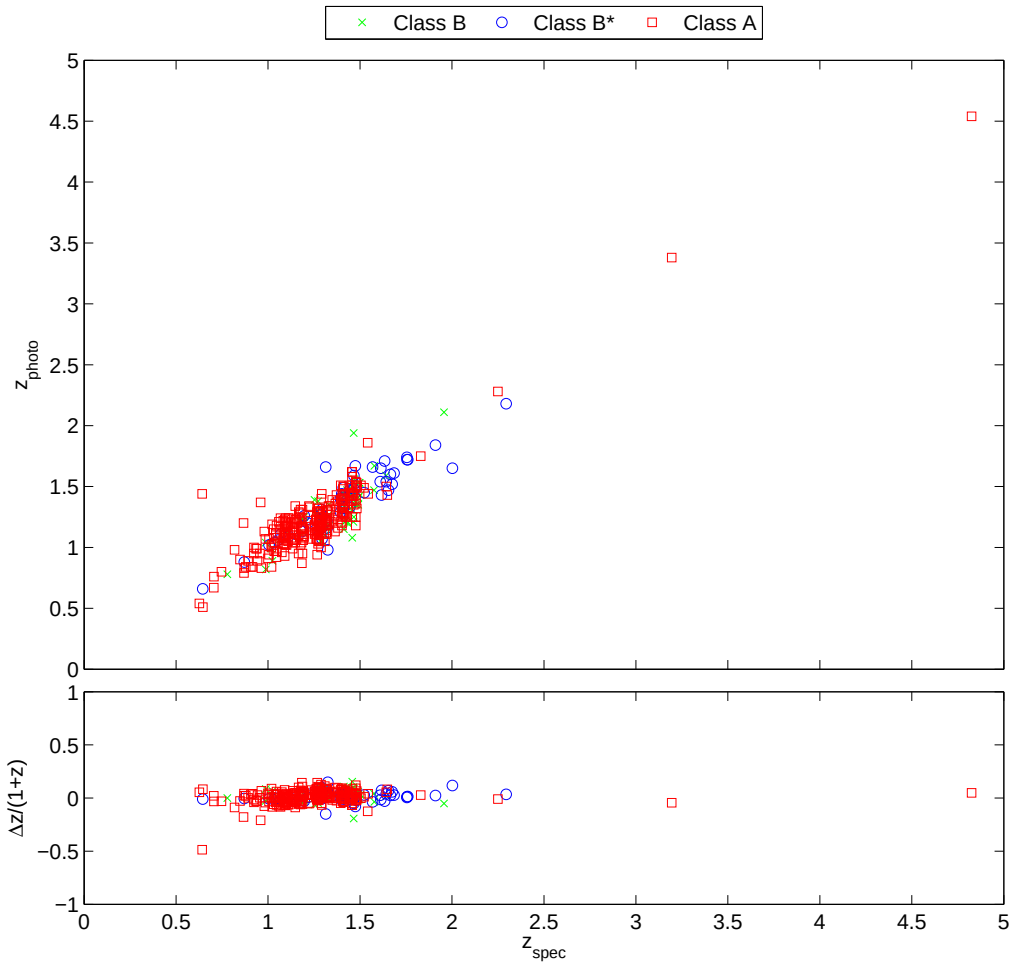

Figure 4.6. Plot of the FORS2 spectroscopic vs photometric redshifts for the primary objects, with class A defined as a good flag (red squares) and Class B* and B defined as less secure and good guess (blue square and green cross) respectively.

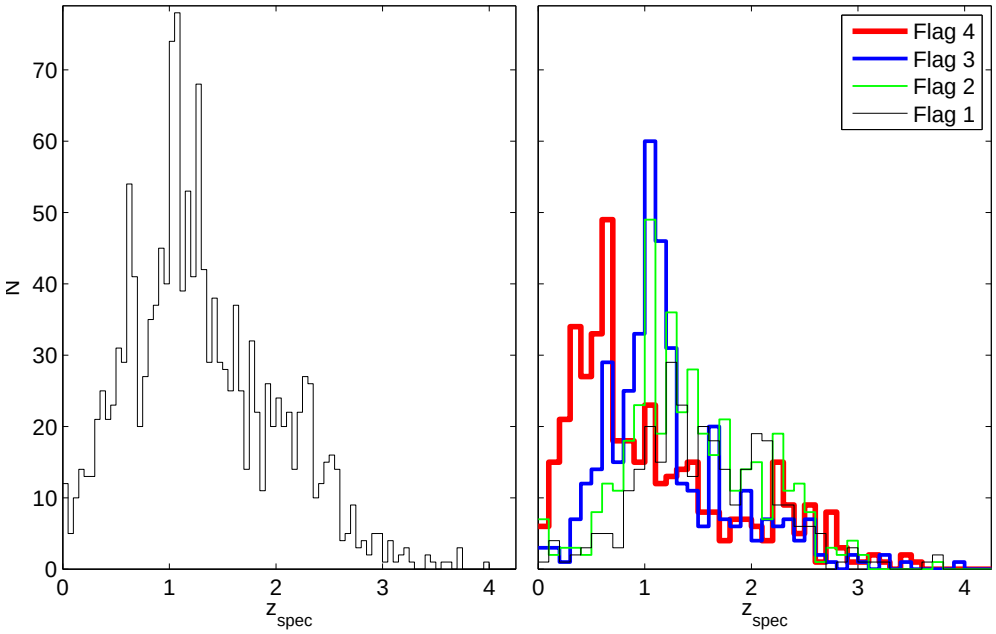

Figure 4.7. Histogram of all the primary VIMOS spectroscopic redshifts, without flags (left) and with flags (right).

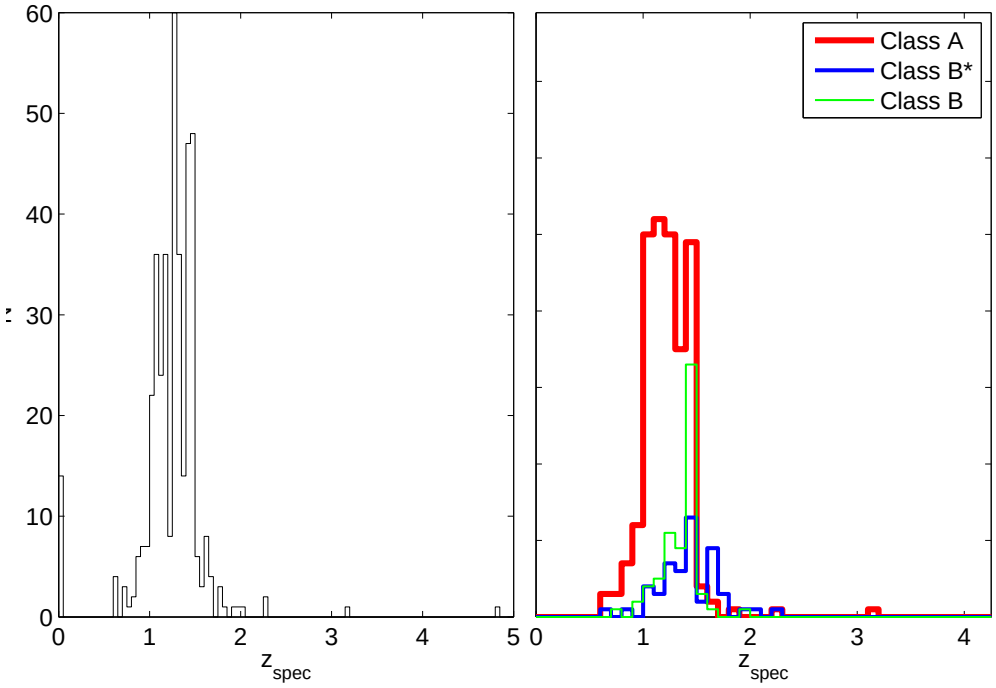

Figure 4.8. Histogram of all the primary FORS2 spectroscopic redshifts, without classes (left) and with classes (right).

Chapter 5

The Effect of Environment on the Spectral Properties of Galaxies

In this chapter I present some preliminary work using the spectra taken with VIMOS and FORS2 (see Chapter 4) to investigate the properties of galaxies in different environments. I further developed the MATLAB code of Chapter 2 to calculate the environments of the spectroscopic galaxies and used IRAF to stack the spectra into different subsets of density, colour and absolute magnitude. I then passed these stacked spectra through STARLIGHT, a spectral template fitting code, to calculate the ages of these averaged spectra. I measured several line indices and spectral features from both the individual and stacked spectra to search for any correlations with local galaxy density and used them to infer the ages and metallicities of the galaxies.

5.1 Introduction

As outlined in Chapter 2, we have performed a study of galaxy environments to $z \sim 2$. Here we have used reliable spectra (flag 3 and 4) from the UDS Spectroscopic survey (UDSz), described in Chapter 4, which used VIMOS and FORS2 on the VLT to provide reliable redshifts and the best S/N spectra for ∼1500 galaxies in the UDS field. We take the spectra of galaxies in 'high' and 'low' density environments and compare their individual and stacked properties.

As the previous chapters have illustrated, it is well established that galaxies in more dense environments are redder than galaxies in low density environments up to redshifts of $z \sim 1$ (Cooper et al. 2007). This colour-density relation has been studied up to $z \sim 2$ (Grützbauch et al. 2011 and Quadri et al. 2011), with varying conclusions in the critical redshift range of $z \sim$ 1-2. High redshift protoclusters allow the study of high redshift environments and their evolution to $z \sim 1$. Steidel et al. (2005) have done this work at $z = 2.3$ and found that galaxies in one candidate protocluster have stellar masses and ages that are ∼2 times larger than identically UV selected galaxies outside the structure. To allow a closer study of the galaxies that live in over-dense and under-dense environments and to further understand the properties of these galaxies, spectra needed to be taken. The UDSz was designed to study the higher redshift universe and redshift desert, but inevitably this yields typical spectra with low signal to noise. To try and mitigate these problems we stack the spectra so that the average properties of the galaxies could be studied.

Previous studies have looked at the effect of environment on the strength of the 4000Å break, [OII] equivalent width and H_δ. Balogh et al. (1999) used the Canadian Network for Observational Cosmology 1 (CNOC1) sample of 15 X-ray luminous clusters to study the effect of the cluster and in the field environment on the properties of the individual galaxies. Their sample of ∼1800 galaxies between $0.18 < z < 0.55$ showed that those in cluster environments have weaker [OII] and H_δ lines and stronger D4000 indices than those in the field. The strength of D4000, which is an indicator for galaxy age, decreased as the cluster centric radius increased, whilst the [OII] and H_δ lines increase. This indicates that current star formation (indicated by the [OII]) and number of A-type stars (indicated by the H_δ) are lower in the cluster-centre than in the field. Similar work has also been done by Kauffmann et al. (2004) using SDSS data and Moresco et al. (2010) using zCOSMOS.

Kurk et al. (2009) used a cluster in the GMASS sample at $z = 1.6$ to compare the properties of the members of the cluster with those outside it. Of interest here is that they made composite spectra in high and low densities in a similar way to what we use in this study. They found that the high-density stacked spectra were far redder and had a much lower [OII] equivalent width than the low-density composite. They also looked at the MgUV index (defined and discussed in more detail later) and found that galaxies in the high density composite had a higher value of the MgUV index than in the low density composite. This indicates much older stellar populations in the cluster than in the field. Another study (Rosati et al. 2009) looked at a spectroscopically confirmed galaxy cluster at $z = 1.39$ and by fitting models also found that there is a strong dependancy of galaxy age on the cluster radius, such that older galaxies are in the core. A similar study using SDSS (Cooper et al. 2008) analysed the metallicity of the galaxies in a sample of ∼57,000 galaxies, concluding that more metal rich galaxies favour higher density regions.
In this chapter we aim to further this and other work by looking at higher redshift and studying more spectral features. The use of FORS2 data also allows us to more reliably study red/passive objects to higher redshifts.

5.1.1 Spectral Features

In this work we use many spectral measures and indices to determine the properties of the galaxies. Here is an outline of what each of the spectral measures mean and what they indicate.

The equivalent width of the [OII]λ3727 (EW[OII]) emission line is measured using IRAF FITPROFS and gives a measure of the intensity of the [OII] line relative to the continuum, giving a negative value for emission lines. This is a reasonable proxy for the star formation rate of more distant galaxies (Rosa-González et al. 2002 and Kewley et al. 2004).

The 4000Å break is measured as:

$$D(4000) = \frac{F_\lambda(4000 - 4100)}{F_\lambda(3850 - 3950)} \tag{5.1}$$

which is the ratio of the average flux density in the 3850-3950Å and 4000-4100Å bands (Balogh et al. 1999 and Kauffmann et al. 2003). This break arises from the

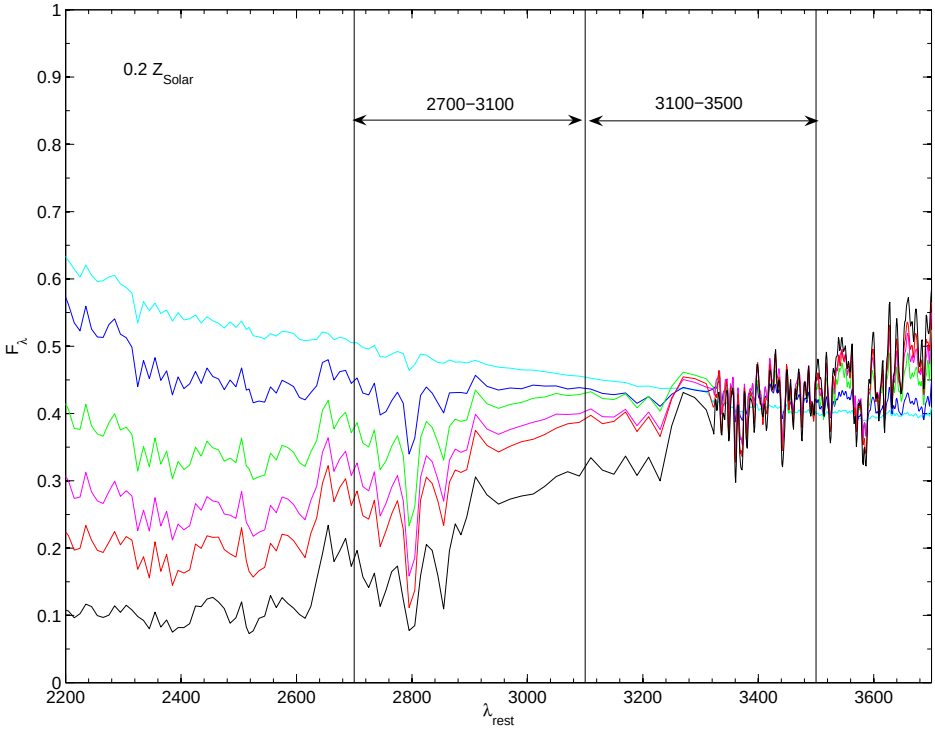

Figure 5.1. Six synthetic spectra (Bruzual & Charlot 2003) showing six different ages; 0.1, 0.3,0.6,0.9, 1.4 and 11 Gyrs (cyan,blue,green,magenta,red and black respectively). All synthetic spectra shown for $0.2Z_{\odot}$. The flux ranges for the C(29-33) index are shown to illustrate the shape of the spectra in those regions.

lack of blue light from the older stellar populations, the end of the Hydrogen Balmer series and from the accumulation of a large number of absorption lines mainly from ionised metals. The older and more metal rich populations are cooler stars with a higher opacity, meaning that the break gets larger as the population gets older (Kauffmann et al. 2003).

Cimatti et al. (2008) define a UV colour, using the ratio of the mean spectral flux between 2700-3100Å and 3100-3500Å rest frame wavelengths such that:

$$C(29-33) = -2.5\log[F_{\nu}(2900)/F_{\nu}(3300)] \tag{5.2}$$

which is an indication of the ratio between very young stars and young stars. Higher values of the C(29-33) index indicate fewer very young stars. Figure 5.1 shows six synthetic spectra of different ages taken from Bruzual & Charlot (2003). It illustrates the effect that the UV slope and MgII feature at 2799Å have on the index; the slope steadily increases as the galaxy gets older. They combine this with the MgUV index which uses a prominant 2600-2900Å feature, which is in turn a combination of breaks at 2640Å and 2900Å and rich metal absorptions (MgI, MgII and FeI and FeII lines) and is defined as:

$$Mg_{UV} = \frac{2\int_{2625}^{2725} f_{\lambda}\, d\lambda}{\int_{2525}^{2625} f_{\lambda}\, d\lambda + \int_{2725}^{2825} f_{\lambda}\, d\lambda} \tag{5.3}$$

where the integration ranges are defined in Å. The presence of this feature ensures that very little if any star formation has occurred in the last ∼0.5 Gyr and that the galaxy's stellar population is consequently passively evolving. This feature is not present in young dust-reddened star forming galaxies, which would make the galaxy look red without having to be old, thus breaking the age/dust degeneracy (Daddi et al. 2005).

We have also measured the individual breaks at 2900Å and 2640Å (Spinrad et al. 1997) which are defined as:

$$B(2900) = \frac{F_\lambda(2915 - 2945)}{F_\lambda(2855 - 2885)} \tag{5.4}$$

$$B(2640) = \frac{F_\lambda(2645 - 2675)}{F_\lambda(2600 - 2630)} \tag{5.5}$$

respectively. Both are the ratios of the mean flux density over a narrow band wavelength interval. The narrow bands mean that they are largely independent of reddening and are related to the opacities of the metal absorption lines and are again used to estimate the age of the stellar population. Higher values of these indices indicates older stellar populations measuring redder colours and stronger metal absorptions, in analogy to the D4000 described earlier.

Two final measures were made; these were of the prominant MgII and FeII absorption lines. These are very clear features in the redshift desert galaxies that we observed in Chapter 4. Again we used IRAF FITPROFS to measure the equivalent widths between 2785-2812Å for MgII and 2572-2613Å for FeII taken from Leitherer et al. (2011) who produced an "atlas" of UV lines.

5.1.2 Data and Sample Selection

Here we use the DR3 sample discussed in Chapter 2, including the same (U-B) red and blue colour cut. We utilise the spectra taken on VIMOS and FORS2 as part of the UDS spectroscopic survey (UDSz) as previously discussed in Chapter 4.

5.1.3 Environmental Measurement

We calculated the projected number density for each galaxy in the spectroscopic sample using the full DR3 catalogue of galaxies with photo-zs, using the spectroscopic redshift if we have one. Only the spectra with the most secure redshift (flag 3 and 4 in VIMOS and class A in FORS2) are used, as incorrect redshifts could hide subtle trends. For each galaxy we use the counts in a 500kpc radius aperture, collapsing a redshift interval, Δz of ±1Gyr calculated according to the equation:

$$\tau = {H_0}^{-1} \int_0^z (1+z)^{-1}[(1+z)^2(1+\Omega_M z) - z(2+z)\Omega_\Lambda]^{-1/2}\, dz \tag{5.6}$$

to minimise contribution from foreground or background objects. This yields a surface density Σ_{AP} in galaxies per Mpc^2. To account for the field edges and any holes in the mask we count the number of images pixels in the mask image within the same aperture and normalise Σ_{AP} by this. This effectively accounts for differences in aperture area. The density is then defined as:

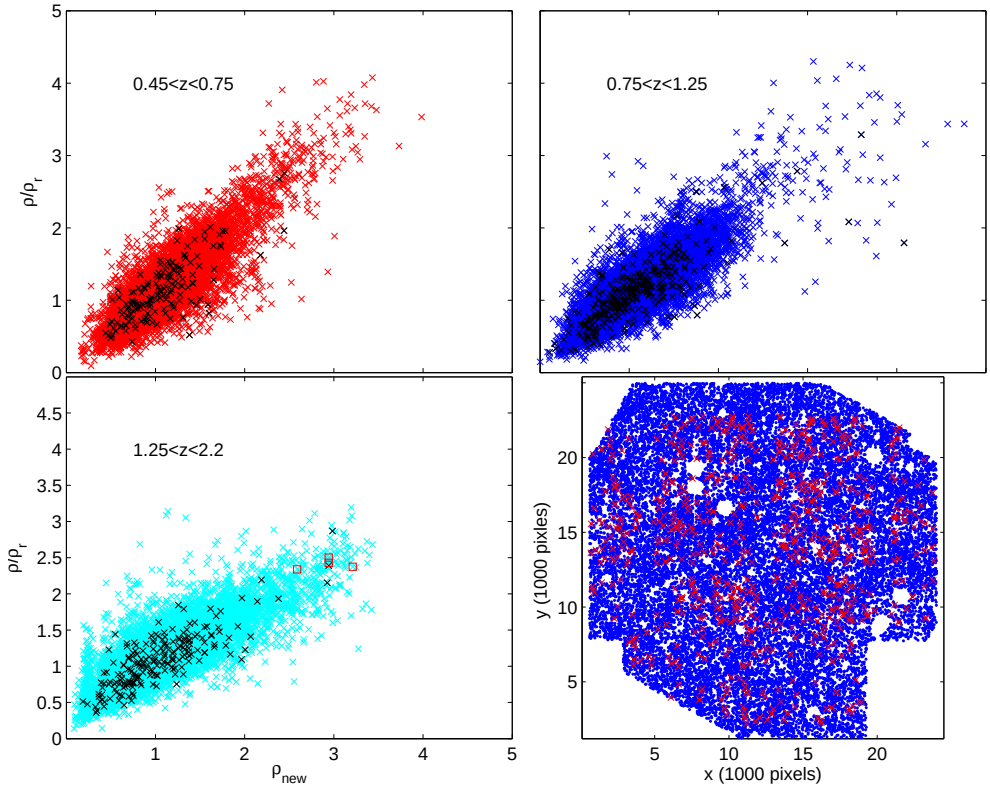

Figure 5.2. New densities using the pixel mask and 1Gyr bins against the density measures from Chapter 2. Galaxies in the UDSz are shown with black crosses and the Papovich et al. (2010) cluster shown with red squares. Also showing the DR3 field (bottom right) with the primary flag 3 and 4 objects indicated by red crosses

$$\rho_{new} = \frac{(N_g^{Aper})_{\Delta z}}{N_{mask}^{Aper}} \times \frac{N_{mask}^{Tot}}{(N_g^{Tot})_{\Delta z}} \tag{5.7}$$

The method described here was used in place of the method used in Chapter 2 as the 1 Gyr interval gives a more physical meaning to the redshift interval used. The use of the mask pixels instead of the random distribution of galaxies to renormalise the galaxy counts also reduces the statistical noise introduced by that method. A plot of these values against the density measures shown in Chapter 2 are shown in Figure. 5.2. This figure also shows that the local densities investigated here inevitably do not span the full range of galaxy environments (black crosses). We are only taking a small subset of the galaxies and due to the mask design we are likely to only sparsely sample the cluster regions. Figure 5.2 also shows the effect of using the 1 Gyr bin in redshift instead of the $z = \pm 0.25$ from Chapter 2. This causes the new density measure to be slightly greater at higher redshift as the redshift bin becomes significantly larger than $z = \pm 0.25$.

5.2 Stacking the Spectra

Before the spectra were used for this work they were all visually inspected to check that they contained no AGN, skylines that were missed or badly extracted, and to ensure the redshifts were as accurate as the data allow. Once any bad objects were

Figure 5.3	NHiρ	NLowρ		
$0.45 < z < 0.75$	56	49		
$0.75 < z < 1.25$	105	100		
$1.25 < z < 2.2$	75	85		
Figure 5.4	NRedHiρ	NRedLowρ	NBlueHiρ	NBlueLowρ
$0.45 < z < 0.75$	18	16	16	21
$0.75 < z < 1.25$	53	37	51	31
$1.25 < z < 2.2$	37	8	24	28
Figure 5.5	NBrightHiρ	NBrightLowρ	NFaintHiρ	NFaintLowρ
$0.45 < z < 0.75$	14	12	24	28
$0.75 < z < 1.25$	60	47	79	64
$1.25 < z < 2.2$	61	36	43	74

Table 5.1. Table showing the number of primary spectroscopic galaxies with flag 3 and 4 in each composite spectra. These are the numbers once the AGN have been removed, the redshifts checked and any objects with spurious emission lines removed. The corresponding Figure is shown in the top left of each subtable.

removed and the redshifts were refined the edges were trimmed from the VIMOS spectra to remove any residuals introduced at the edge of the detector as well as fringing at the red end. This was not done for the FORS2 galaxies as the there is not a significant amount of fringing and the signal to noise is generally low, making it hard to determine where to cut. The spectra were then over-sampled to 1Å pixelscale to ensure that no spectral information was lost during the stacking phase. Finally, the spectra were de-redshifted to enable them to be stacked in their various redshift bins. The spectra were subsequently combined using the average SCOMBINE routine with both no scale and a mean scale applied to the spectra before the stacking. This was done to allow us to study the difference between the galaxies where they all count equally (mean scale) and where the brighter ones counted more (no scale). Scaling the spectra by their mean value results in equal contributions from each single galaxy spectrum irrespective of its total magnitude. The scaled, stacked spectrum is then representative of the average galaxy in the population, rather than being biased towards the brighter galaxies in the sample. Furthermore, it was found that the scaled spectra gave a more reliable smoother spectra than a pure mean stack. All stacks discussed in the following chapter are combined with an average scaling. The number of spectra that go into each stack are shown in Table 5.1.

5.3 Results

5.3.1 High and Low Density Spectra

Firstly we stack the spectra in high and low density thirds. This was done in three redshift bins and is illustrated in Figure 5.3 with two columns, the first displaying the [OII] and D4000 region and the second showing the FeII/MgII region. The left hand panel of the plot is always normalised between 3400-3600Å and the right hand panel is normalised between 2900-3100Å, to allow easier comparison. The lowest density bin shows that the break (top left) is slightly stronger in the high density

third ($\rho \gtrsim$1.25, red line) than in the lowest density third ($\rho \lesssim$0.8, blue line). This indicates that the redder, older galaxies with a stronger D4000 reside in denser environments but is not really apparent in the higher redshift bins. Interestingly the [OII] strength is very similar in both of composite spectra, i.e. it does not appear to depend strongly on on environment. The [OII] strength in the final redshift bin (bottom left) does show some dependence on environment, with the [OII] being stronger in the lowest density bin. There are no visible differences between the highest and lowest density stacks in the MgII/FeII region but this will be analysed further later. Similar stacks were made using only galaxies with -24< M_K <-22 to remove any effect due to luminosity. This luminosity range was chosen as it give a reasonable number of galaxies but was narrow enough not to have an effect. These were very similar to the plots shown here and do not change any of the conclusions. We conclude that the stacked spectra of our high-z galaxies do not appear to depend strongly on environment. As discussed later in the chapter, this conclusion may be strongly influenced by the limited dynamic range of environment that we can probe (see Figure 5.2), or by the limited number of very red galaxies in our spectroscopic sample at $z > 1.5$, but from this crude test the relationship between typical spectra and environment appears to be quite subtle for 'typical' galaxies in the UDS.

5.3.2 Red and Blue Spectra

Throughout this thesis we have separated the sample into red and blue as a proxy for age and morphological type. This has been done by using rest frame (U-B) colour to divide the galaxies into the red sequence and blue cloud. Here we have the chance to see how well this represents the true stellar age using spectral features to show whether out cut is valid or not. The spectra were divided into red and blue objects according to $(U - B) = -7.09 \times 10^{-3} M_K + 0.52$ from our DR3 catalogue and into high ($\rho > 1.1$) and low ($\rho < 1.1$) density. They were also selected to be $-24 < M_K < -22$ to remove any effect introduced by the luminosity/mass of the galaxy. Figure 5.4 shows these stacks in three redshift bins and two interesting sections of the spectra. The first column shows the [OII] and break region whilst the second column shows the various features around the MgII and FeII region. Four spectra are shown in each section, these are the high density blue (blue line), low density blue (green line), high density red (black line) and low density red (red line) galaxies. These data demonstrate that in the lowest redshift bin the break (top left) is strongest for the high density red galaxies (see Section 5.4.1 for further analysis), indicating that red objects in dense environments are on average older than in low density areas. This is also shown by the low [OII] strength in the high density red sample. The blue galaxies seem to show no dependence on environment, both the high density and low density blue galaxies have very similar spectra (blue and green lines). The Fe-Mg region (top right panel) shows that the high density red objects have a steeper UV slope than the low density red objects, again indicating that they are older, more evolved objects, which fits with conventional wisdom.
The second redshift bin still shows a larger break for the red galaxies in the high density bin (black line - left centre) but smaller than in the previous redshift bin as would be expected; galaxies look younger in the earlier universe. In the final redshift bin (bottom left) the spectra look very similar as there are few red objects due to the nature of the survey and at this redshift range the break and [OII] line move beyond the clean spectral range of the instruments. However this panel does show there is less [OII] flux for the red objects. The differences between high and low density are

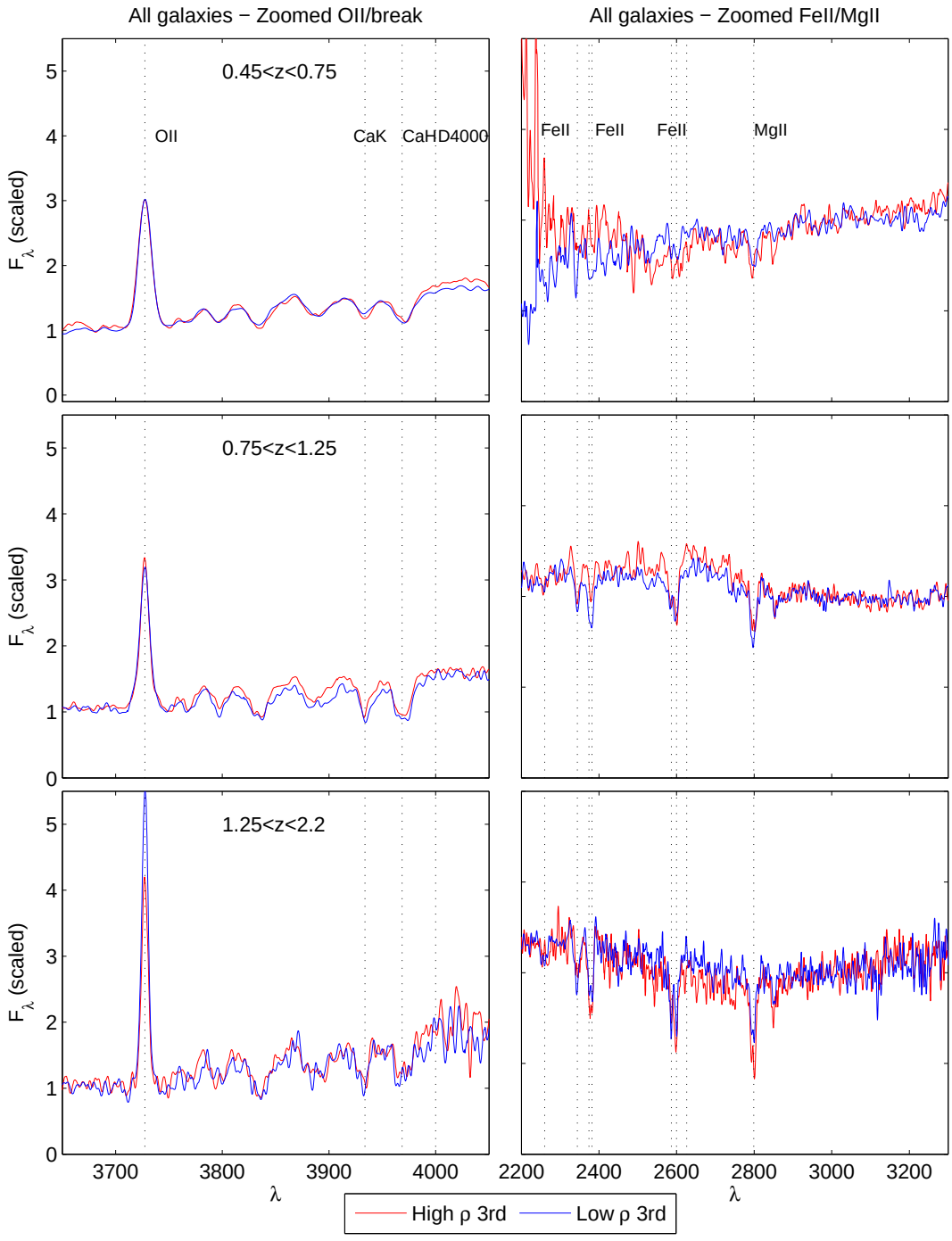

Figure 5.3. Stacked spectra into highest and lowest density thirds in the three redshift ranges and two interesting spectral regions.

Redshift bin	Colour	Density	Age (Gyr)
0.45 - 0.75	Red	High	5.79
0.45 - 0.75	Red	Low	3.61
0.45 - 0.75	Blue	High	1.36
0.45 - 0.75	Blue	Low	1.35
0.75 - 1.25	Red	High	3.83
0.75 - 1.25	Red	Low	1.4
0.75 - 1.25	Blue	High	1.16
0.75 - 1.25	Blue	Low	1.31
1.25 - 2.2	Red	High	1.42
1.25 - 2.2	Red	Low	2.41
1.25 - 2.2	Blue	High	1.16
1.25 - 2.2	Blue	Low	1.09

Table 5.2. Table showing the ages of the stacked spectra. Shows the red and blue spectra in high and low density, with the ages calculated from STARLIGHT (Cid Fernandes et al. 2005; Cid Fernandes et al. 2009) at $1Z_{\odot}$

much more pronounced if the sample is split into red and blue populations and are now visible up to $z \sim 1.25$ for the red sample. This suggests that red galaxies are more affected by environment and stopped forming stars earlier in higher density environments. The features discussed in this section plus the ones in the second column of Figure 5.4 will be discussed further later in the Chapter.

We used STARLIGHT (Cid Fernandes et al. 2005; Cid Fernandes et al. 2009) to fit the ages of the high and low density red and blue spectra. This package adds up a number of pre-defined base spectra to match the input spectra as closely as possible. We use ∼20 base spectra taken from BCO3 (Bruzual & Charlot 2003) all with solar metallicity and varying in ages. In this preliminary analysis a fixed metallicity is chosen for all of the spectra so that the age/metallicity degeneracy does not lead to unreliable ages. A mask file is used to remove any emission lines from the fit and an estimate for the velocity shift (v_0=0 km/s) and velocity dispersion (v_d=150 km/s) of the spectra are also put into the grid file, from which the code is run. A reddening law is chosen and in the first instance the curve from Cardelli et al. (1989) (CCM) was utilised. This gave sensible results in the two highest redshift bins but gave surprising results in the lowest redshift bin resulting in unrealistic old ages for the blue low density galaxies. This is due to the degeneracy between age and dust content. To try and improve the ages given in the lowest redshift range the extinction was set to be zero at all wavelengths. This gave much more sensible answers in the lowest redshift bin and values that are similar to the values obtained using CCM in the higher redshift bins. The ages given by STARLIGHT at fixed solar metallicity ($1Z_{\odot}$) are shown in table 5.2. The consistently older ages of the red galaxies in high densities up to $z \sim 1.25$ confirm the visual impression gained from Figure 5.4.

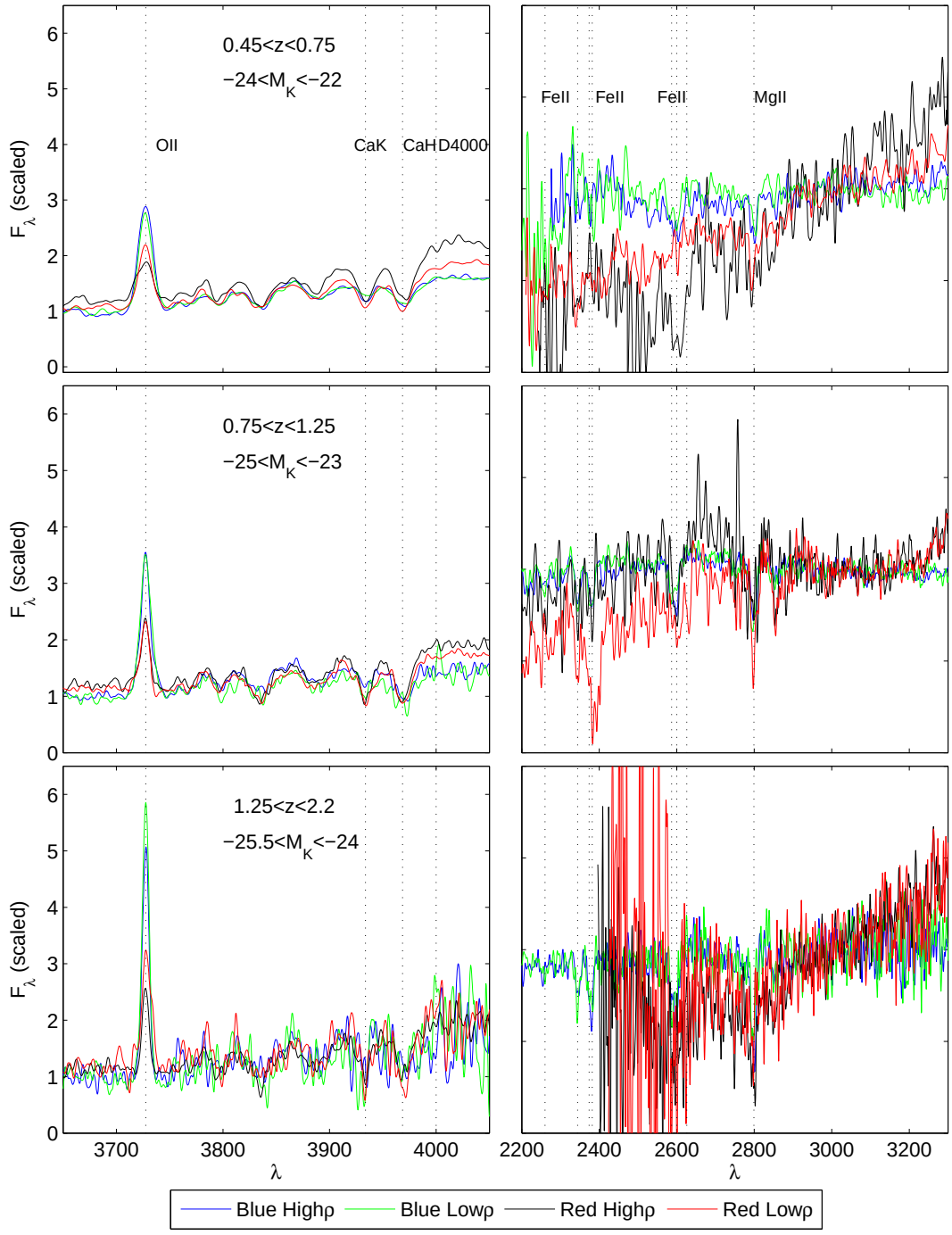

Figure 5.4. Stacked spectra in two density bins and divided into red and blue in the three redshift ranges and two interesting spectral regions.

5.3.3 Bright and Faint Spectra

Finally, we stack the spectra according to the galaxy's K-band luminosity (Figure 5.5). We combine all objects with -25.5< M_K <-24 and -24< M_K <-22.5 to investigate whether there is any relationship between the galaxies' environment and its luminosity. In the lowest redshift bin (top) there seems to be a small effect on the size of the break (top left) in that the faint objects differ, with the faint higher density objects having a higher break than the lower density ones. This difference does not seem to occur for the brighter objects. This suggests that as well as red galaxies, faint galaxies are significantly affected by the environment, at least up to $z \sim 0.75$. Figure 5.5 also shows that bright, low density objects in the redshift range $0.75 < z < 1.25$ have much stronger MgII/FeII absorption and weaker [OII] emission than for any other spectrum. The [OII] emission at higher redshifts also appears to increase for fainter systems, which is consistent with downsizing, i.e. the more massive galaxies have already 'switched off'. One last observation of interest is that the galaxy K-band luminosity (a good proxy for stellar mass) appears to have a stronger effect on the galaxy spectra than the environment, with only subtle changes between the high and low density spectra for both the bright and faint galaxies.

5.4 Fitting the spectra

To analyse the stacked and single spectra more throughly we measured the many indices that were discussed in Section 5.1.1. Figures 5.7 to 5.14 show eight of these spectral measures against density. They all display three redshift bins except for the D4000 which only shows the lowest two as at the highest redshift this is no longer measureable. The left hand column in each figure shows the spectral measure against density for each single spectrum. The single points are divided into red (red points) and blue (blue points) galaxies, brighter objects ($M_K \leq$-24) are highlighted by the filled points. The right hand column shows the average spectral measure in bins of density, once again divided into red (red line) and blue (blue line) objects. The same measure from the stacked spectra are over-plotted to illustrate the average spectral measure in both the high and low density and red and blue galaxies. The density values used for these are the mean of all the spectra that went into the stack. In each figure the result from a Spearman's rank correlation coefficient (S.R.) of the raw data is shown in the lower right. This value ranges between 1 and -1 where 0 is no correlation at all and 1 and -1 are total positive or negative correlation respectively.

5.4.1 Spectral Measures - Red and Blue

As mentioned earlier, the spectra, amongst others things, provide an opportunity to test whether the red/blue cut in U-B colour that we use is robust. Each of these plots (Figures 5.7 to 5.14) show galaxies divided into red and blue. Some of them show a significant bimodality between the two colour subsets. For example the D4000 (Figure 5.7) shows that red objects have higher D4000 than blue objects with a reasonably distinct line between the two populations at about 1.2. This is as expected, as redder galaxies U-B filters straddle the D4000 break (see Section 5.1.1). The equivalent width of the [OII] line also shows a significant bimodal nature between the red and blue populations with most of the red objects having little or no [OII] emission. Passive, red galaxies are expected to have little or no [OII] emission

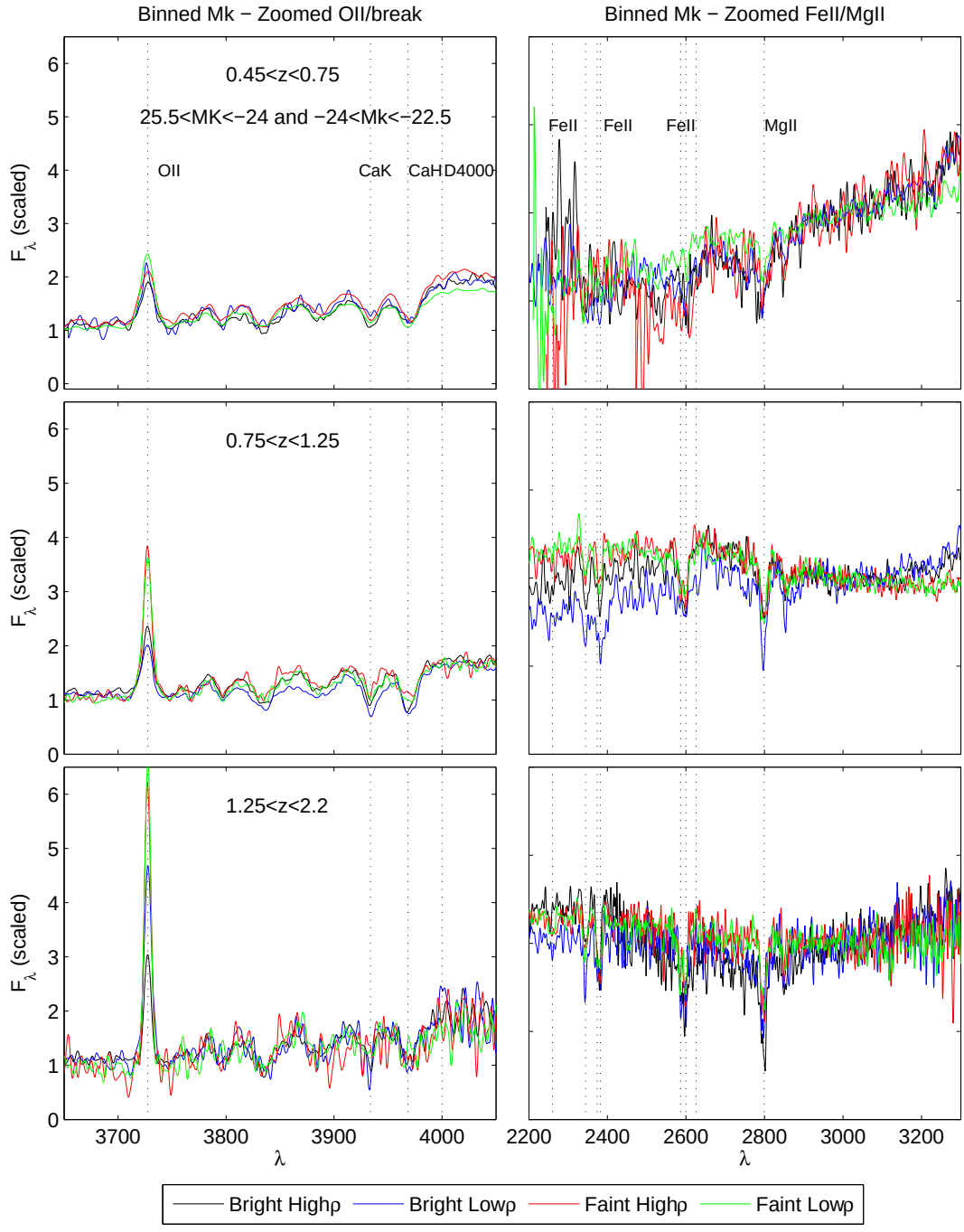

Figure 5.5. Stacked spectra in two M_K bins and two density bins in the three redshift ranges and two interesting spectral regions.

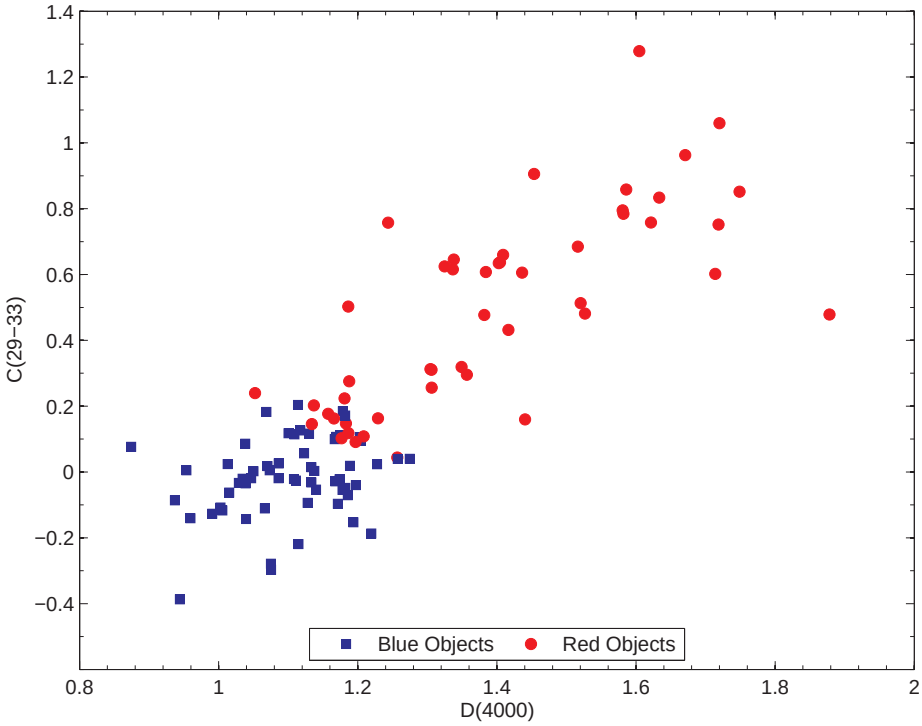

Figure 5.6. The D4000 index against the C(29-33) index, showing objects that are either red or blue in rest frame U-B colour.

as it is a sign of ongoing star formation (although AGN activity may also produce [OII] in an otherwise passive galaxy; Kocevski et al. 2010). The other measures show some signs of a difference between red and blue galaxies but the most striking bimodality is in the C(29-33) index which at all redshifts displays a distinct difference with little overlap between the populations. This is a good sign that the red and blue subsets are robust as the region around 3000Å which the C(29-33) measures is not used in the definition of red and blue objects, unlike the D4000 break. Figure 5.6 shows the D4000 index verses the C(29-33) index to indicate the relationship between the two and to illustrate the separation between the red and blue objects in rest frame U-B colour. It shows a good correlation between the D4000 and C(29-33) indices and illustrates the clear separation between red and blue in both indices.

5.4.2 Spectral Measures - Analysis

To look at any relationships that may occur between the spectral features and density for red and blue objects we now take a more in depth look at the various features studied:

(a) D(4000) - Figure 5.7 shows that at $0.45 < z < 0.75$ (upper plot) the red galaxies break strength increases with increasing density, so that red galaxies in higher densities have stronger breaks. For the blue galaxies there appears to be no trend. This is also apparent in the stacked spectra in Figure 5.4. The relationship between D4000 and density for red galaxies does not seem to be present at higher redshift ($0.75 < z < 1.25$), with both the red and blue galaxies exhibiting a flat profile with density. The results from the stacked spectra displayed in the

right hand panels (coloured stars) also show the same correlation. The measured D4000 strength from the high density red stack (red star) is higher than for the low density red stack (magenta star) . This indicates that older galaxies lie in denser environments.

(b) EW[OII] - Figure 5.8 shows that there is no significant trend of the [OII] strength with environment. There is a marginal trend shown in the stacked spectra (Figure 5.4, upper left) and coloured star points on Figure 5.8 that in higher densities red objects have less [OII] emission but this may not be significant. Studies at similar redshifts (Cooper et al. 2008; Poggianti et al. 2008) have found that denser environments suppress star formation and that this continues up until at least $z \sim 1$. We only see a hint of this in the stacked spectra, one possible cause for this that we are more likely to give an object with an [OII] emission line a high flag (3 or 4) as it is a strong feature. This may cause the denser environments to have greater [OII] emission present.

(c) C(29-33) - Figure 5.9 shows that the $0.45 < z < 0.75$ bin displays a trend with density, such that higher densities have a greater C(29-33) index. In the binned data this seems to turn over at $\rho \sim$1.5, then decreasing with increasing density but does not look significant for the individual spectra (left hand column). The increase in the C(29-33) index is also clear in the stacked spectra plot (Figure 5.4) and in the measured values from the stacks (coloured stars in Figure 5.9). These both show a large value of the C(29-33) index for the denser red objects. This is another age indicator and shows that there are very few young stars in the red objects, with even fewer at higher densities. Interestingly at $0.75 < z < 1.25$ this does not seem to be the case, with even the opposite happening; denser galaxies having lower values of the C(29-33) index. If true this would indicate that there was a more significant number of very young stars in the higher densities. The highest redshift bin (lower plot) shows a trend more similar to the trend seen at $0.45 < z < 0.75$, that higher density galaxies have less very young stars.

(d) MgUV - Figure 5.10 the MgUV feature is an indication of the lack of ongoing star-formation and the presence of this feature indicates that there has been little if any star formation within the last ∼0.5 Gyr. Red galaxies on the whole have a stronger MgUV feature and in the lowest redshift bin (upper plot) the strength of this feature increases with density. This is shown in both the left and right plots as well as in the stacked spectra and measurements from them. The high density red stack (red star) indicates a higher MgUV index than the low density red stack (magenta star). Once again the blue objects show very little trend with density.

(e) B2900 - Figure 5.11 this feature is a break feature but is only present in very old galaxies (Cimatti et al. 2008). Once again the red galaxies exhibit a stronger break than the blue galaxies as can be seen. There is little significant trend with environment for either the blue or red galaxies, as can also be seen with the measures from the stacked spectra (right column - star points).

(f) B2640 - Figure 5.12 this feature is very similar to the B2900 feature. It too shows little significant trend with density maybe with the hint of an increase at high densities in the lowest redshift bin.

(g) EW MgII and EW FeII - Figures 5.13 and 5.14. Both of these features are very prominent in the spectra but show no relationship with environment and do not significantly separate with colour either.

5.4.3 Spectral Measures - [OII] vs D4000 and MgUV vs C(29-33)

From the above analysis it is clear that four spectral measures are most significant. The equivalent width of [OII], the D4000 break, MgUV and the C(29-33) index all seem to show some interesting trends. Studies in the past have investigated correlations between equivalent width of [OII] and the D4000 break strength (for example Mignoli et al. 2005 and Franzetti et al. 2007) and the MgUV index against the C(29-33) index (Cimatti et al. 2008). We do the same here to investigate any environmental trends. Figures 5.15 to 5.17 show these plots with our data, separated into high and low density. The upper plot shows the EW[OII] against the D4000 break and the lower plot shows the MgUV index against the C(29-33) index. For each plot there is an apparent magnitude cut in which the feature would appear at that redshift (indicated by the filled points). This is done to try and highlight the higher signal to noise objects with more robust measures. On each plot (as before) we show the same measure from the stacked spectra, indicated by the coloured stars. Measures from the high and low density red and blue objects are indicated by the red, magenta, blue and green stars in each plot. Finally in the lower right of each plot is the significance (from a KS test) between the high and low density galaxies for that spectral feature.

Figure 5.15 shows the lowest redshift bin that we studied. The top panel shows the relation between the EW[OII] and the 4000Å break. We find that galaxies with strong breaks have little or no [OII] emission and as the break strength weakens the range of equivalent widths of [OII] increases. This therefore places red passive objects in the top right of the diagram and blue star-forming objects to the bottom left. From the plot it is clear that high density objects (magenta points) tend to occupy the top right hand corner whilst the low density objects (cyan points) tend to group at the bottom left of the plot. The bottom panel of Figure 5.15 shows the MgUV vs C(29-33) indices. This plot was used by Cimatti et al. (2008) to identify high-z passive galaxies as these group in the upper right region of the plot. High values of both indices indicate that there has been little star-formation in the last $\sim$0.5 Gyr and that there are few very young stars in the galaxy. So we expect galaxies in denser environments to group towards the upper right of the plot as galaxies in denser regions are on average redder/more passive. This is generally what we see, with the high density (magenta) galaxies tending towards the top right of the plot, with the low density (cyan points) grouping towards the lower left. This is also confirmed by the measures taken from the stacked spectra, for example the high density red stack (red star) is in the top right of the plot where as the blue high density stack (yellow star) is in the bottom left. The low density red objects (magenta star) have a similar amount of [OII] to the higher density objects but significantly weaker D4000 breaks. The low density blue objects (green star) are similar to the high density blue objects (blue star).

Figure 5.16 shows the $0.75 < z < 1.25$ redshift range. This shows a less clear distinction between the high and low density objects than in Figure 5.15. There

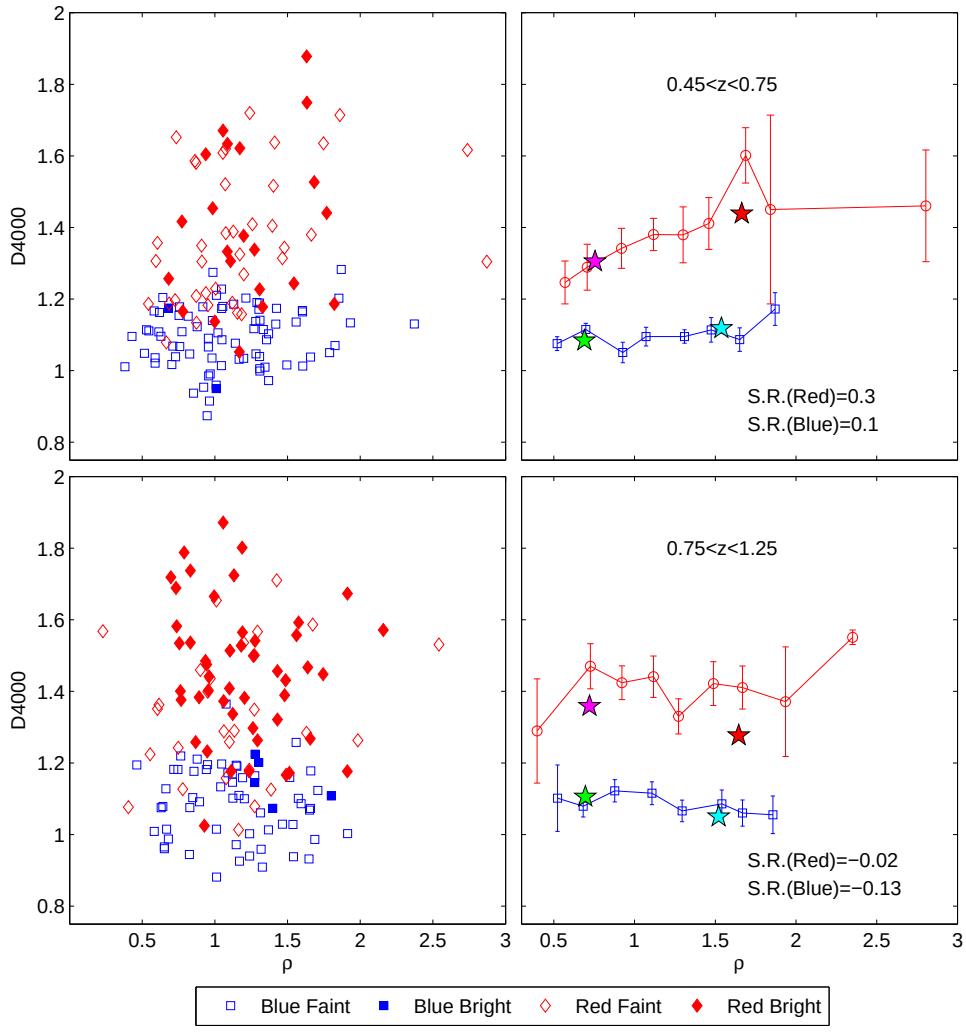

Figure 5.7. Density versus the D4000 break strength in two redshift bins. Showing both the raw data points (left) and the average of break strength in bins of density (right). The left figure shows the red and blue objects, where the filled points indicate that the objects have an $M_K \leq$-24. The values from the stacks are also included on the right-hand plot, where the coloured stars indicate high density red galaxies (red star), low density red (magenta), high density blue (cyan star) and low density blue galaxies (green star). The error bars shown here are the error on the mean. The values shown in the lower right are the Spearman's rank correlation coefficient of the raw data for the red and blue galaxies.

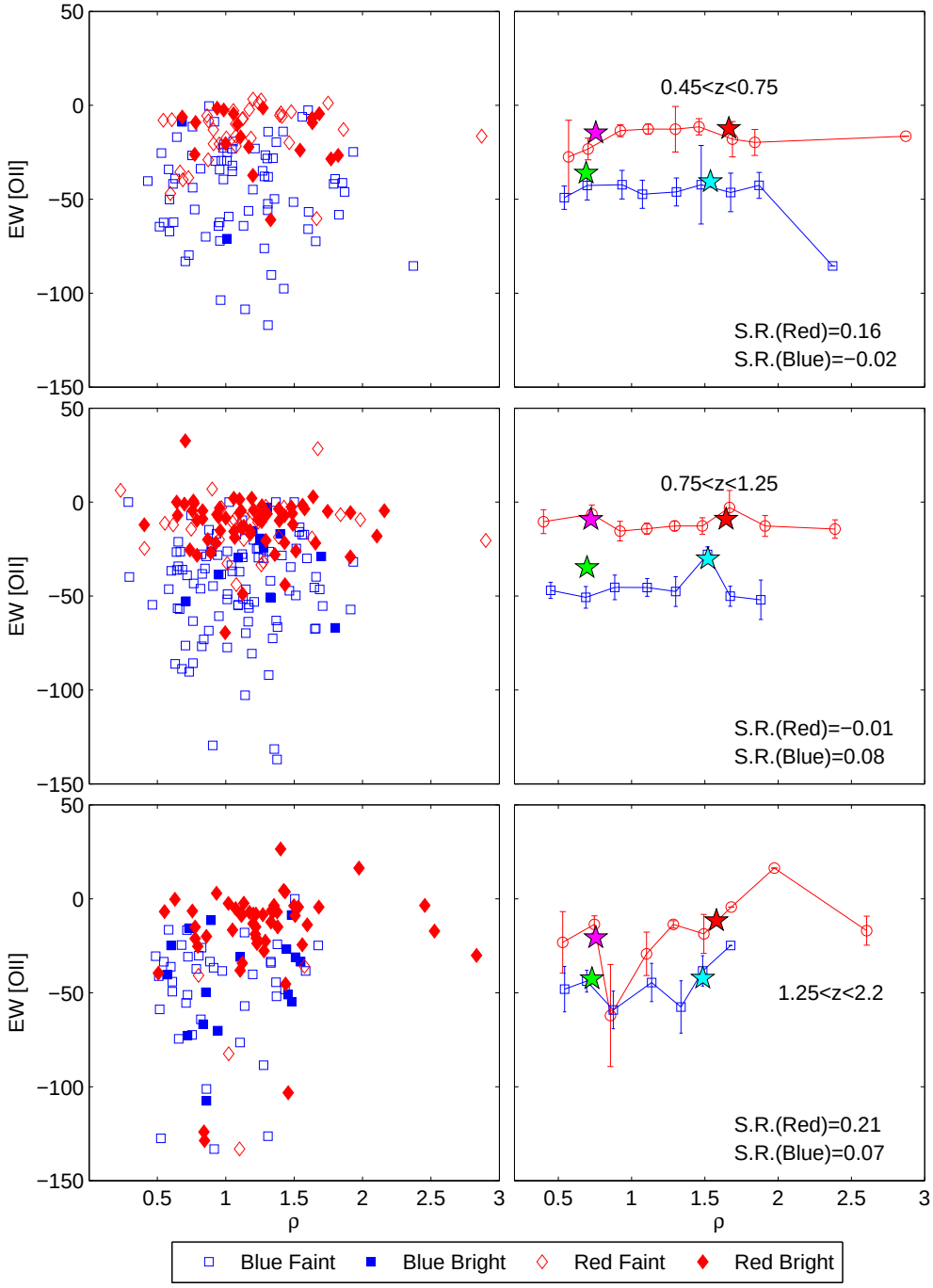

Figure 5.8. Density versus the equivalent width of [OII] in three redshift bins. Showing both the raw data points (left) and the average [OII] width in bins of density (right). The left figure shows the red and blue objects, where the filled points indicate that the objects have an $M_K \leq$-24. The values from the stacks are also included on the right-hand plot, where the coloured stars indicate high density red galaxies (red star), low density red (magenta), high density blue (cyan star) and low density blue galaxies (green star). The error bars shown here are the error on the mean. The values shown in the lower right are the Spearman's rank correlation coefficient of the raw data for the red and blue galaxies.

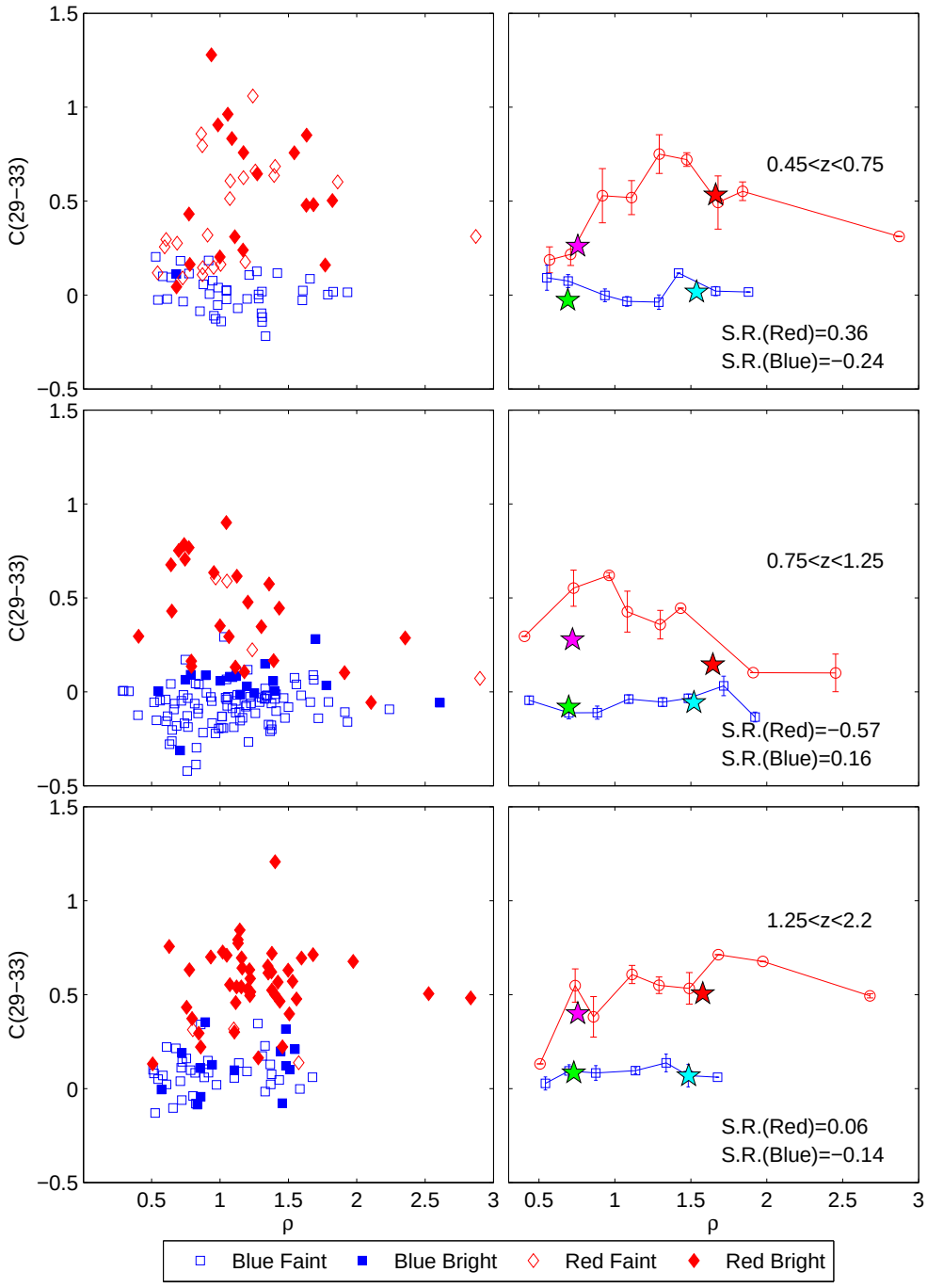

Figure 5.9. Density versus the C(29-33) index in three redshift bins. Showing both the raw data points (left) and the average C(29-33) index in bins of density (right). The left figure shows the red and blue objects, where the filled points indicate that the objects have an $M_K \leq$-24. The values from the stacks are also included on the right-hand plot, where the coloured stars indicate high density red galaxies (red star), low density red (magenta), high density blue (cyan star) and low density blue galaxies (green star). The error bars shown here are the error on the mean. The values shown in the lower right are the Spearman's rank correlation coefficient of the raw data for the red and blue galaxies.

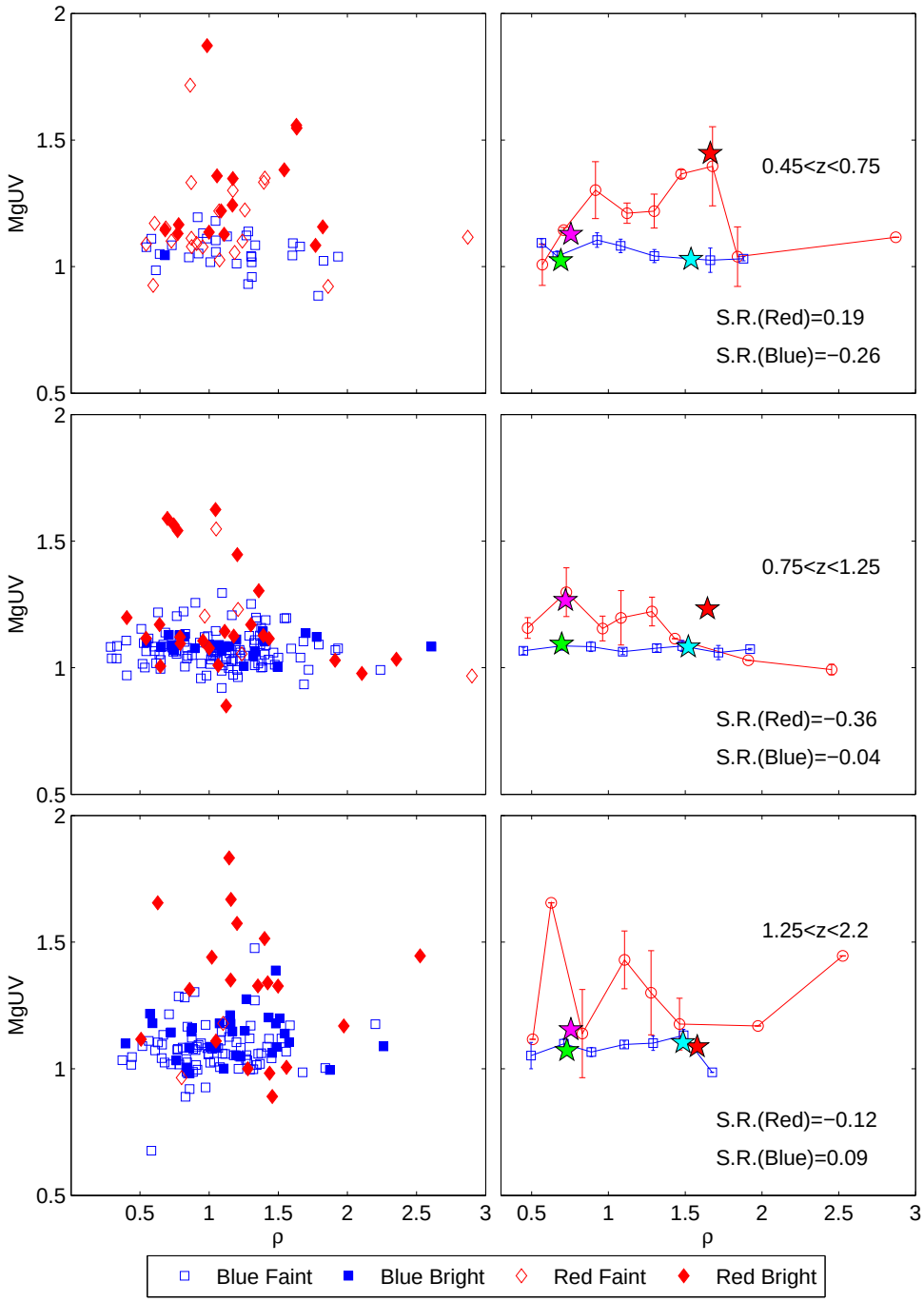

Figure 5.10. Density versus the MgUV index in three redshift bins. Showing both the raw data points (left) and the average MgUV index in bins of density (right). The left figure shows the red and blue objects, where the filled points indicate that the objects have an $M_K \leq$-24. The values from the stacks are also included on the right-hand plot, where the coloured stars indicate high density red galaxies (red star), low density red (magenta), high density blue (cyan star) and low density blue galaxies (green star). The error bars shown here are the error on the mean. The values shown in the lower right are the Spearman's rank correlation coefficient of the raw data for the red and blue galaxies.

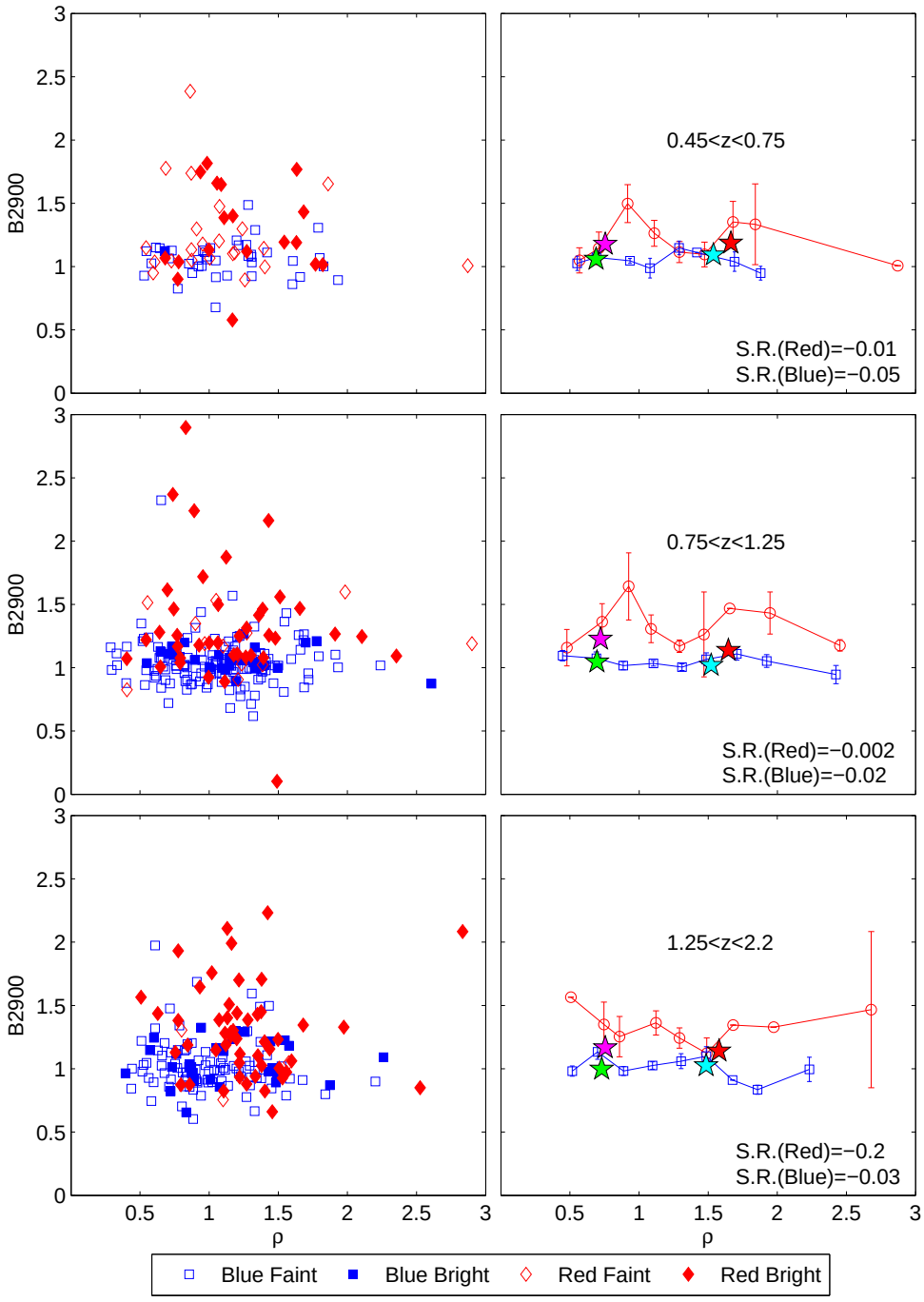

Figure 5.11. Density versus the B2900 break strength in three redshift bins. Showing both the raw data points (left) and the average B2900 index in bins of density (right). The left figure shows the red and blue objects, where the filled points indicate that the objects have an $M_K \leq$-24. The values from the stacks are also included on the right-hand plot, where the coloured stars indicate high density red galaxies (red star), low density red (magenta), high density blue (cyan star) and low density blue galaxies (green star). The error bars shown here are the error on the mean. The values shown in the lower right are the Spearman's rank correlation coefficient of the raw data for the red and blue galaxies.

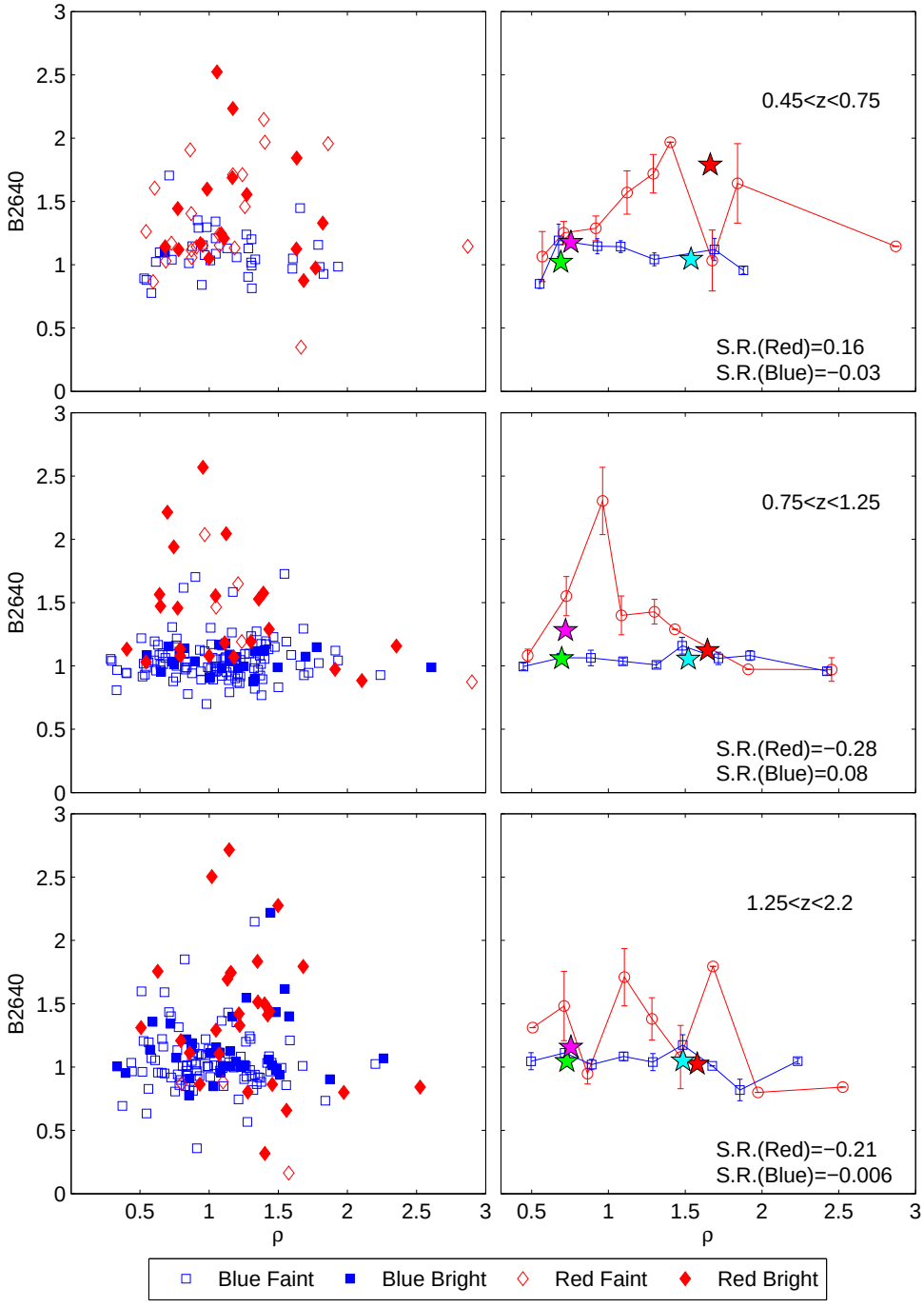

Figure 5.12. Density versus the B2640 break strength in three redshift bins. Showing both the raw data points (left) and the average B2640 index in bins of density (right). The left figure shows the red and blue objects, where the filled points indicate that the objects have an $M_K \leq$-24. The values from the stacks are also included on the right-hand plot, where the coloured stars indicate high density red galaxies (red star), low density red (magenta), high density blue (cyan star) and low density blue galaxies (green star). The error bars shown here are the error on the mean. The values shown in the lower right are the Spearman's rank correlation coefficient of the raw data for the red and blue galaxies.

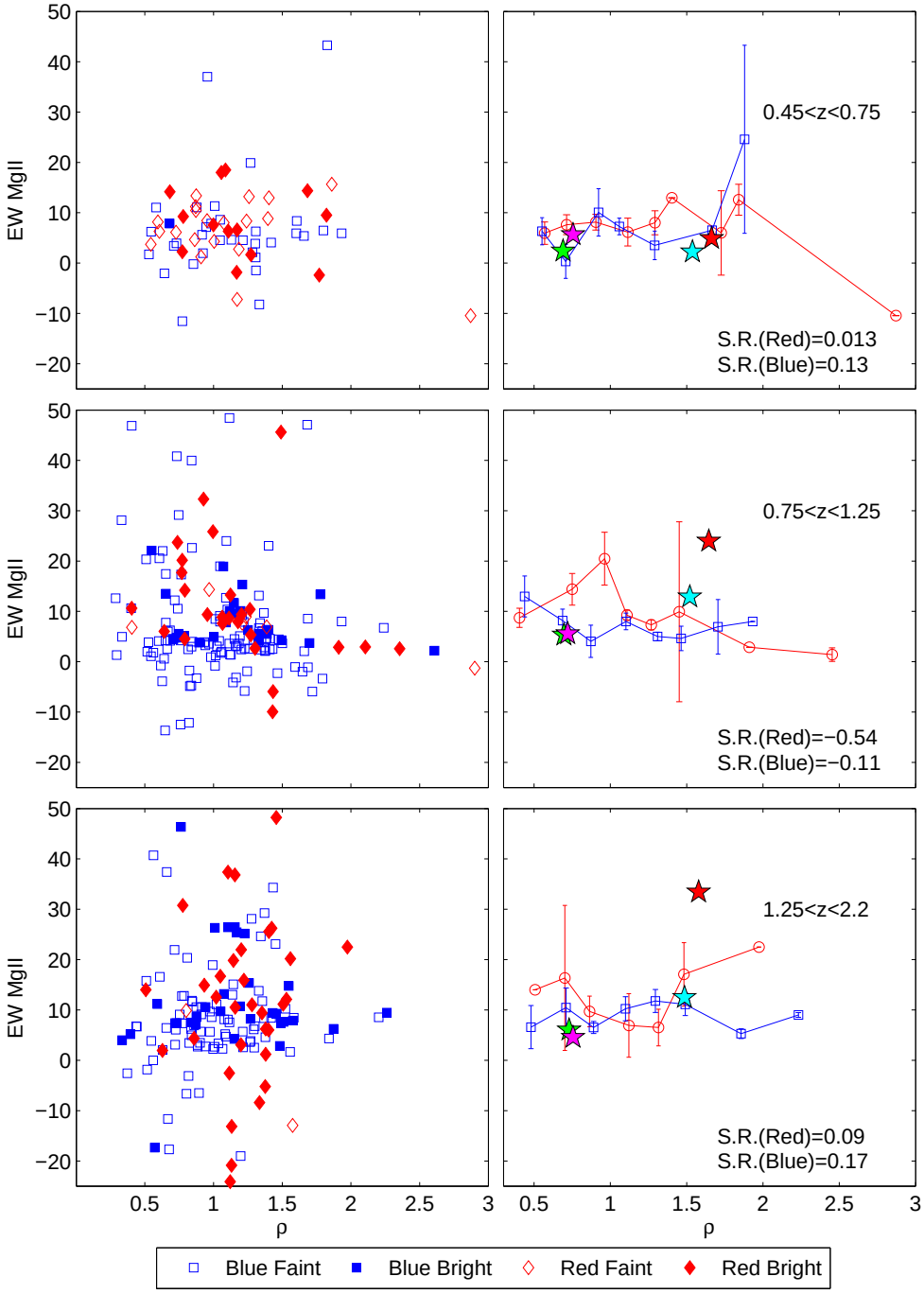

Figure 5.13. Density versus the MgII EW in three redshift bins. Showing both the raw data points (left) and the average MgII EW in bins of density (right). The left figure shows the red and blue objects, where the filled points indicate that the objects have an $M_K \leq$-24. The values from the stacks are also included on the right-hand plot, where the coloured stars indicate high density red galaxies (red star), low density red (magenta), high density blue (cyan star) and low density blue galaxies (green star). The error bars shown here are the error on the mean. The values shown in the lower right are the Spearman's rank correlation coefficient of the raw data for the red and blue galaxies.

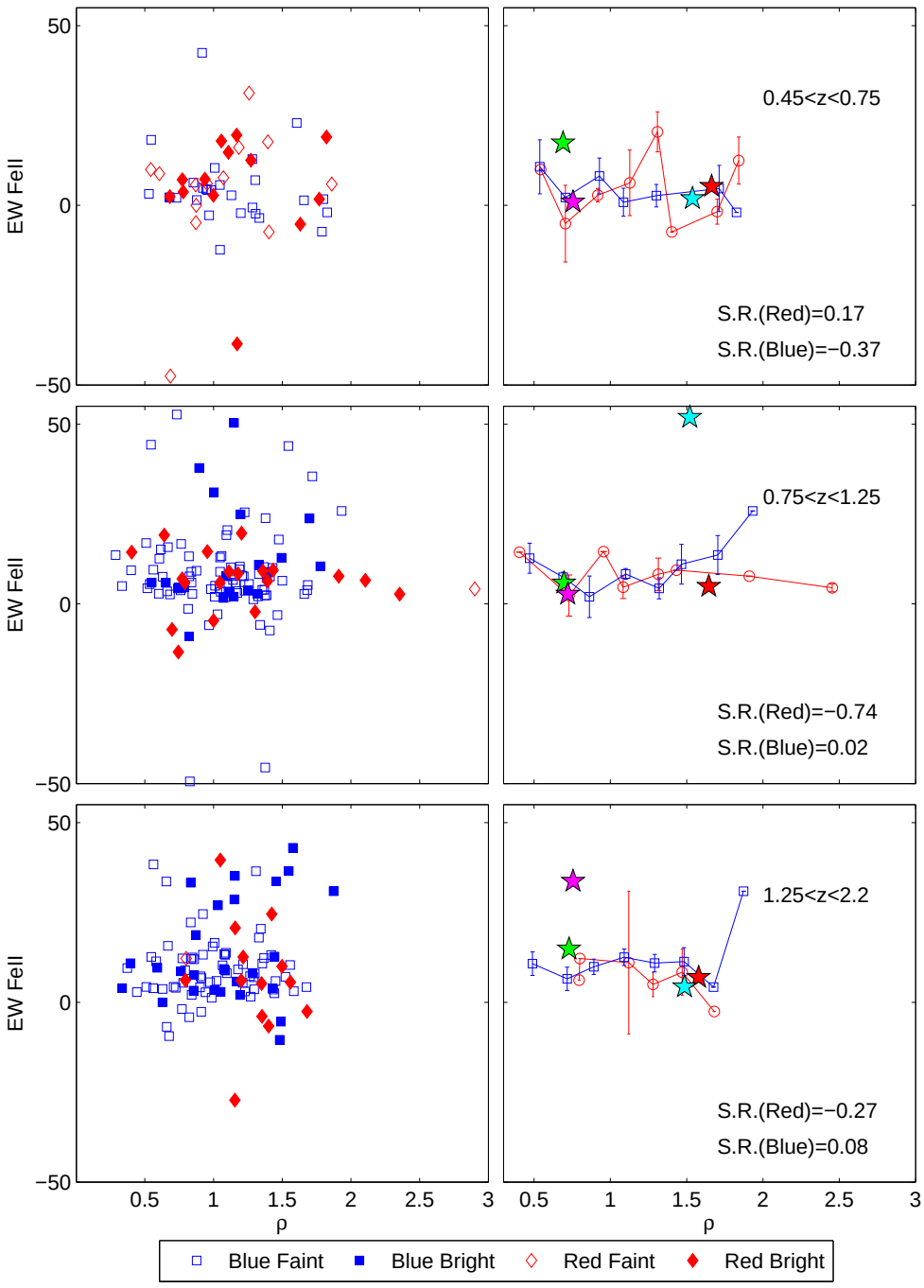

Figure 5.14. Density versus the FeII EW in three redshift bins. Showing both the raw data points (left) and the average FeII EW in bins of density (right). The left figure shows the red and blue objects, where the filled points indicate that the objects have an $M_K \leq$-24. The values from the stacks are also included on the right-hand plot, where the coloured stars indicate high density red galaxies (red star), low density red (magenta), high density blue (cyan star) and low density blue galaxies (green star). The error bars shown here are the error on the mean. The values shown in the lower right are the Spearman's rank correlation coefficient of the raw data for the red and blue galaxies.

are a reasonable fraction of low density (cyan points) in the passive region (upper right) of the [OII] vs D4000 plot. The values for the stacked spectra also seem to show a weaker separation, even showing that the low density red objects (magenta star) have a higher D4000 than the high density galaxies (red star). Although the red galaxies are still more grouped towards the passive top right corner than the blue objects (green and blue stars). The MgUV vs C(29-33) plot (lower plot) shows a similar correlation to the [OII]/D4000 plot (top) than low density galaxies do not seem to separate as much as in the low redshift bin. Here the stacked spectra measures show that the low density red objects exhibit more passive indices than the high density red objects. However they still separate from the blue objects (green and blue stars). This indicates that although red and blue objects still separate well in these diagrams, the colour-density relation is weaker, as seen before.

In the highest redshift bin studied here (Figure 5.17) we are unable to study the D4000 as it is no longer detectable. As a proxy for this we have used the B2900 as this is a break that is known to indicate age/passivity (as discussed earlier in the Chapter). Although no direct conclusions can be drawn from this, reassuringly the red stacked spectra (red and magenta stars) do show a stronger B2900 break and less [OII]. Interestingly in the MgUV vs C(29-33) plot the high density objects once again tend to occupy the passive top right of the plot. However at this redshift range we have few red spectra and any objects that are classified as red are likely to be very luminous objects and at the lower end of the redshift range.

5.5 Conclusions

Here we have studied the effect of environment on the spectra taken from the UDSz survey. Using over 700 spectra in the redshift range $0.45 < z < 2.2$ we have measured eight spectral features including the important EW[OII], D4000, MgUV and C(29-33) indices. These are all features that are used to determine the age and star-formation fate of galaxies. This chapter presents a preliminary analysis, and will be investigated further by our team, but the preliminary conclusions so far are as follows:

1. The U-B colour cuts that we use to select red and blue objects show strong separations in many of the spectral features. The stacked spectra also show that red galaxies have a much stronger D4000 break feature and weaker [OII] emission than their blue counterparts. These trends are expected as the rest frame U-B filters are designed to straddle the break. However, it is interesting to note that the red and blue galaxies also separate well in the C(29-33) index which is not used in the determination of red and blue galaxies. The C(29-33) index appears to be a good way of dividing up red and blue galaxies using the bluer wavelengths.

2. Higher density red galaxies have stronger D4000 breaks than low density red galaxies, meaning that galaxies in denser environments tend to be older/more passive than lower density galaxies. Fainter galaxies also seem to exhibit stronger breaks in higher densities than ones in lower densities, whereas the bright sample do not show any difference. This may be because the fainter objects are less massive so can be more easily affected by the surrounding gravitational potential or by stripping.

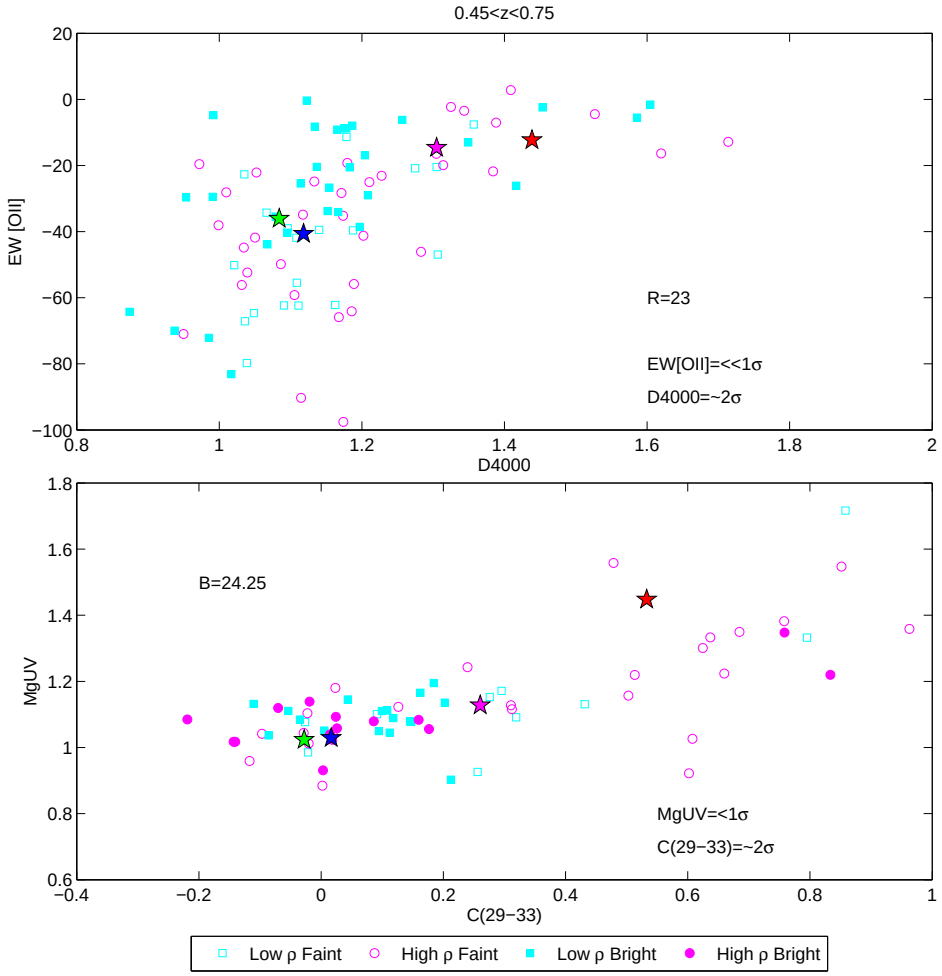

Figure 5.15. [OII] against D4000 and MgUV against C(29-33) index in high and low density for $0.45 < z < 0.75$. Filled symbols show objects brighter than the cut indicated in the figure. The measures from the stacked spectra are shown by the red, magenta, blue and green points which correspond to the high density red galaxies, low density red, high density blue and low density blue galaxies respectively. The σ values are obtained by performing a KS test, representing the significance in rejecting the null-hypothesis that the samples are drawn from the same underlying population.

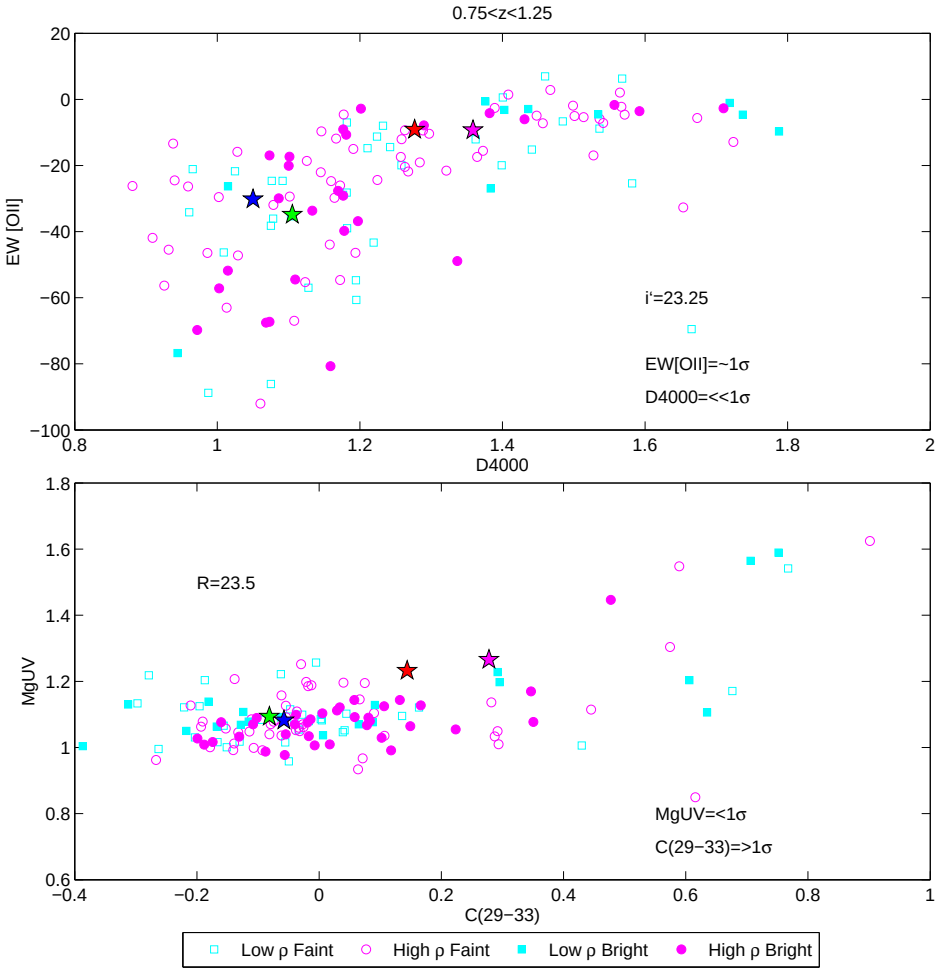

Figure 5.16. [OII] against D4000 and MgUV against C(29-33) index in high and low density for $0.75 < z < 1.25$. Filled symbols show objects brighter than the cut indicated in the figure. The measures from the stacked spectra are shown by the red, magenta, blue and green points which correspond to the high density red galaxies, low density red, high density blue and low density blue galaxies respectively. The σ values are obtained by performing a KS test, representing the significance in rejecting the null-hypothesis that the samples are drawn from the same underlying population.

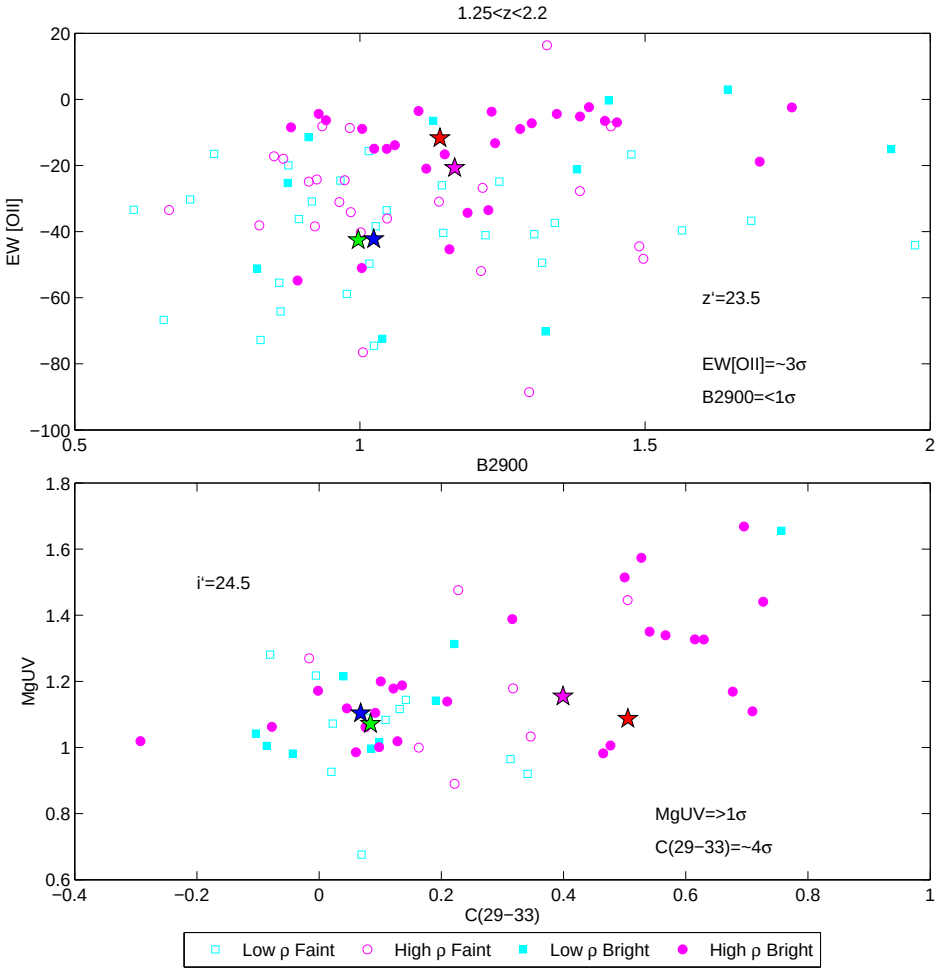

Figure 5.17. [OII] against D4000 and MgUV against C(29-33) index in high and low density for $1.25 < z < 2.2$. Filled symbols show objects brighter than the cut indicated in the figure. The measures from the stacked spectra are shown by the red, magenta, blue and green points which correspond to the high density red galaxies, low density red, high density blue and low density blue galaxies respectively. The σ values are obtained by performing a KS test, representing the significance in rejecting the null-hypothesis that the samples are drawn from the same underlying population.

3. Further work needs to be done to fully determine the effect environment has on these spectra features. We have only found significant differences with a few features at certain redshifts. The most interesting and significant are in the high redshift ($1.25 < z < 2.2$) range. Here we saw a 4σ difference between high and low density in the C(29-33) and a 3σ difference in the strength of the [OII] emission (as shown in Figure 5.17). The C(29-33) index indicates the ratio of the number of very young stars to the number of young stars, with higher numbers indicating fewer very young stars. The results here show that at higher densities the galaxies are on average older, with little if any recent star formation. This high redshift bin ($1.25 < z < 2.2$) also shows a significant difference in the strength of the [OII] emission, with higher densities having less [OII] emission than in the lower density environments, as is seen at lower redshift (for example Kauffmann et al. 2004; Cooper et al. 2008). The correlations that we found in Section 5.4 were only weak but as Cooper et al. (2010) pointed out it is much easier to wash out a signal than it is to erroneously detect one between independent variables.

4. From Figures 5.7 to 5.14 it appears that local environment only has a subtle effect on the typical spectral characteristics of galaxies. These figures tend to show a large separation in colour but only a very weak trend with density, if any. It also tentatively indicates that if there is any trend with environment it tends to be more pronounced in the lower redshift bin ($0.45 < z < 0.75$) as in Figures 5.7 and 5.9. This may indicate that environment only plays a small roll in the evolution of galaxies, with halo mass and time being more significant drivers. It may also be the case that the relative significance of these drivers may change with redshift.

A note of caution must be added to these conclusions due to a few selection effects that this investigation suffers from. For example, as mentioned earlier we have a relatively limited dynamic range in environment due to the mask preparation and because we are only sampling a small fraction of the galaxies in the UDS field. We may be missing the effects that occur in the more extreme environments, as we undersample these regions and because they are rare objects. We are also missing the oldest, reddest objects at $z > 1.5$ as these are beyond the reach of optical spectrographs. Setting these caveats aside, however, we have been able to investigate the possible influence of environment on the spectral features for a wide range of galaxies to $z < 1.5$, and at least the unobscured star-forming population at higher redshifts.

Chapter 6

The Colour-Density Relation up to $z \sim 3$ in the UDS DR8

6.1 Introduction

In this chapter I expand upon the work of Chapter 2 with the Data Release 8 (DR8) of the UDS. I utilise a slightly different method for estimating galaxy environments, using redshift bins around each galaxy of 1Gyr and use a new renormalisation method to try and speed up the code, and remove any uncertainty introduced by the random galaxies that may be present in the original method (see Chapter 2). I use the UDS DR8 catalogue constructed by the UDS team and the photometric redshifts, colours and absolute magnitudes calculated by Ruth Grützbauch. The DR8 is approximately one magnitude deeper in K than in the DR3, with additional U-band and IRAC photometry, which allows us to probe much fainter galaxies resulting in more meaningful local densities. Additionally we use the UDSz redshifts (Chapter 4) to refine the photometric redshifts which will further refine the environment measurement and allow a robust study of environments at $z \sim 2$. For this chapter I have calculated the environments and carry out all the subsequent work.

6.1.1 DR8 Data

The Data Release 8 (DR8) consists of all the UKIDSS UDS data taken up to the end of January 2010, more than doubling the exposure time. This plus a refinement in the data reduction pipeline at CASU, which alone gives a ∼0.3 magnitude improvement, leads to the exposure times and depths (5σ, $2''$ diameter) shown in Table 6.1. The catalogue produced from this data consists of 147,455 objects (194,508 in total) at the limit of K=24.6 (AB) with a spurious fraction of ∼1.5% (∼0.87% for the total number of sources). All saturated objects were classed as stars, bright but unsaturated stars were removed by $K_{3"} <20$ and $K_{3"} - K_{1"} >$ -0.7. These were adopted as they define a clear and distinct stellar locus to K<20. Fainter stars were removed if Sextractor's class_star > 0.8 and if the following colour ($2''$) cuts were satisfied: $(z - K) < 0.3(B - z) - 0.5$ and $(B - J) > 7.5(J - 3.6\mu m) + 10$. The two colour cuts were used to try and mitigate against misclassification of compact galaxies with star-like colours in one or the other selection diagrams. Cross-talks were also identified given the known offset pattern from bright stars and then checked manually, giving a cross-talk fraction of ∼1% (see Almaini et al. in preparation for more detail). A K band cut at 24 was then applied to the remaining galaxies giving 68,629 out of a total of 143,305 objects with photometric redshifts. The cut at

	DR3 AB Depth	DR8 Exposure time	DR8 AB Depth	DR8 Vega Depth
J	23.7	173 hours	24.9	24.0
H	23.5	92 hours	24.2	22.8
K	23.7	192 hours	24.6	22.7

Table 6.1. Table showing the exposure time, Vega and AB depths for the three bands. With the DR3 depths shown for comparison.

K=24 was made as this was the measured completeness of the data and removed faint objects with more unreliable magnitudes.

6.1.2 Photometric Redshifts

The photometric redshifts used here were determined by Ruth Grützbauch using the HYPERZ package (Bolzonella et al. 2000). This was done by fitting templates to the optical and near-IR filters UBVRizJHK and IRAC (3.6 and 4.5μm) photometric data. The response function of each filter is convolved with the CCD-efficiency, the reflectivity of the mirror as well as the transmission curve of the instrument including atmospheric transmission.
HYPERZ uses a standard χ^2 minimisation technique to determine the best-fitting spectral energy distribution (SED) from a range of SEDs with different stellar population ages, star-formation histories and dust extinction.The synthetic spectra used by HYPERZ are constructed with the Bruzual & Charlot evolutionary code (Bruzual A. & Charlot 1993). The model SEDs are characterised by a Salpeter initial mass function (IMF) and an exponentially declining star-formation rate, where the timescale τ ranges from 1 to 15 Gyr and is chosen to resemble the morphological types of galaxies found in the local universe (E,S0,Sa,Sb,Sc,Sd and Im). Additionally we use a single burst SED, i.e., without any star-formation happening after the initial burst. The SEDs are evolved in age ranging from 10^6 to 2×10^{10} yr and extincted by dust using the reddening law from Calzetti et al. (2000) with steps in A_V of 0.2 magnitudes. The metallicity is fixed to the solar value due to the degeneracy between age, reddening and metallicity. Bolzonella et al. (2000) showed that changing the metallicity of the stellar population does not affect or improve the resulting photometric redshifts and that changes in age and reddening are sufficient to produce model SEDs that fit the observed photometry. A similar process also calculates the absolute magnitudes and colours used here.

To estimate the quality of the new DR8 photometric redshifts we compare them to secure spectroscopic redshifts (see Chapter 4 and Figure 6.10.). In this work we also use the recent UDSz redshifts (flag 3 and 4) which gives greater coverage above $z > 1$ compared to the DR3, especially increasing the number of red galaxies due to the high sensitivity of the FORS2 instrument at red wavelengths. We carefully exclude possible AGN from the sample by matching the spectroscopic catalogue to catalogues of X-ray and radio detections as well as removing galaxies with broad emission lines identified during the visual inspection of the spectra. This gives a photometric redshift outlier-clipped $\Delta z/(1+z) = 0.038$, with 3% outliers with a $\Delta z/(1+z) > 0.15$. We do not apply a χ^2 cut to the sample since the above statistics do not improve significantly after applying cuts at different values of χ^2.

6.1.3 Red and Blue Definition

The red and blue galaxies are separated using rest frame (U-B) colour using the slope from Hartley et al. (2010) as in Chapter 2 but in this work we consider an evolving cut. This leads the dividing line in the colour-magnitude diagram to be: $(U-B)_{rest} = -7.09 \times 10^{-3} M_K + A$, where A is the boundary at each redshift. This boundary was measured empirically by fitting a double gaussian to the data in the redshift bins used. This gave a $(\text{U-B})_{rest}$ $\sim$0.24 magnitude difference in the rest frame colour cut between $0.25 < z < 0.75$ and $2.75 < z < 3.25$ which is in agreement with Cassata et al. (2008). A theoretical colour cut based on the expected passive evolution of the stellar population following Kriek et al. (2008) was also calculated and gave a Δ(U-B)=0.16 over the same range. Throughout this paper the empirical cut is used unless otherwise stated.

6.1.4 Environmental Measurement

We primarily use the counts in an aperture method with apertures chosen at three radii, 500kpc, 250kpc and 125kpc (physical) to study the local environments of the galaxies. Around each galaxy a redshift interval of Δz= $\pm$1Gyr is collapsed onto a 2D plane to minimise the contribution from background and foreground objects. The number of galaxies within the aperture and redshift interval are counted, $((N_g^{Aper})_{\Delta z})$ giving a density of:

$$\rho = \frac{(N_g^{Aper})_{\Delta z}}{N_{mask}^{Aper}} \times \frac{N_{mask}^{Tot}}{(N_g^{Tot})_{\Delta z}} \tag{6.1}$$

where N_{mask}^{Aper} is the number of mask pixels within the aperture of the galaxy and N_{mask}^{Tot} is the total number of mask pixels. The mask pixels, used in the catalogue formation replaces the "randoms" used in Chapter 2 to renormalise the galaxy counts and to take account of the edges and masked regions. This was done to reduce the computational time and to minimise the statistical error introduced by the random distribution of galaxies in the original DR3 method.

As a secondary measure we use the nearest neighbour approach, calculating the distance to the third (D_3), fifth (D_5) and seventh (D_7) nearest galaxy within Δz=$\pm$1Gyr. The number of image pixels within the area ($N_{pixels}(D_n)$) is then calculated to determine the area covered in Mpc^2 around each galaxy. In analogy to the method described above and the randoms used in Chapter 2 this is then multiplied by the total number of pixels in the mask (N_{mask}^{Tot}) divided by the total number of galaxies in the respective redshift slice ($(N_g^{Tot})_{\Delta z}$) to give:

$$\rho_{NN} = \frac{n}{N_{pixels}(D_n)} \times \frac{N_{mask}^{Tot}}{(N_g^{Tot})_{\Delta z}} \tag{6.2}$$

where n=3,5 or 7 for the nearest neighbour of interest. The distance to an edge or a hole is also calculated and if the distance to the nth nearest neighbour is greater than the distance to the edge then the object is removed. This is done to ensure that the edges and holes, to which this method is very sensitive, are removed. The aperture densities are used throughout this work (unless otherwise stated) due to its simplicity and better reliability near holes and edges than the nearest neighbour method.

6.2 Results

Here we study the environments of red and blue galaxies as a function of redshift in bins of 1Gyr. This was chosen to give the redshift interval a more physical meaning than in the original work shown in Chapter 2 but wide enough that photo-z errors are minor.

6.2.1 Red and Blue Environments

Figure 6.1 shows a histogram of all the densities in each redshift bin of the red and blue galaxies. The figure demonstrates simply the difference between the densities of the red and blue populations. This difference is clearly apparent in the first two redshift bins, becoming increasingly less apparent to higher redshift. A KS test shows that the differences between the two populations are significant at $>3\sigma$ until $1.25 < z < 1.75$ where red galaxies are consistently found in more dense environments that blue galaxies. At higher redshifts the differences are not significant any more with $\sigma \sim$1-2. The significance levels are given in each panel of Figure 6.1.
Figure 6.2 shows a plot of the mean aperture density of red and blue galaxies in bins of absolute K-band magnitude, which is used as a proxy for stellar mass. Three columns are shown displaying the three aperture sizes used, 500kpc, 250kpc and 125kpc radius. Six bins of redshift are plotted with the fourth bin also showing star-forming and passive BzK galaxies defined by Daddi et al. (2004). The error bars are calculated from the error on the mean density of galaxies within a given magnitude bin. This plot shows that at a given K-band magnitude red galaxies reside in significantly denser environments at lower redshifts. This marked difference progressively weakens at higher redshift and beyond $z \sim 1.5$ it is no longer apparent. As seen in Chapter 2, Figure 6.2 also indicates a general trend of increasing galaxy density with luminosity, particularly for the blue galaxies and on smaller scales. This is most apparent between $z \sim 1.5$ and $z \sim 2.5$, seemingly weaker before and after this epoch. This is interesting as this is the epoch when the bulk of the galaxy red sequence is established (Bell et al. 2004; Cirasuolo et al. 2007) and when it is thought massive galaxies merge (Conselice et al. 2008). The pBzKs and sBzKs follow the red and blue population respectively, with no significant differences between them. The lowest redshift bin of Figure 6.2 shows that faint red galaxies are strongly affected by environment, this was also tentatively seen in Chapter 5 where Figure 5.5 shows that fainter galaxies at low redshift seem to be more strongly affected by environment that brighter objects.

The DR8 allows us to extend the study of environments of red and blue galaxies to fainter or higher redshift galaxies. As a result of the extra magnitude in depth we have gained a large amount of objects in the interesting $1.75 < z < 2.25$ range. The DR3 data hinted that the differences between red and blue may disappear at this redshift. The DR8 data seemingly agree with this conclusion and tentatively shows this convergence out to $z \sim 3$.

6.2.2 Colour-Density Relation

Figure 6.3 shows the average density as a function of the $(U - B)$ rest frame colour with faint ($-22 < M_K < -20.5$) and bright ($-24 < M_K < -22$) galaxies shown in green and black respectively. The colour-density relation is shown in three aperture

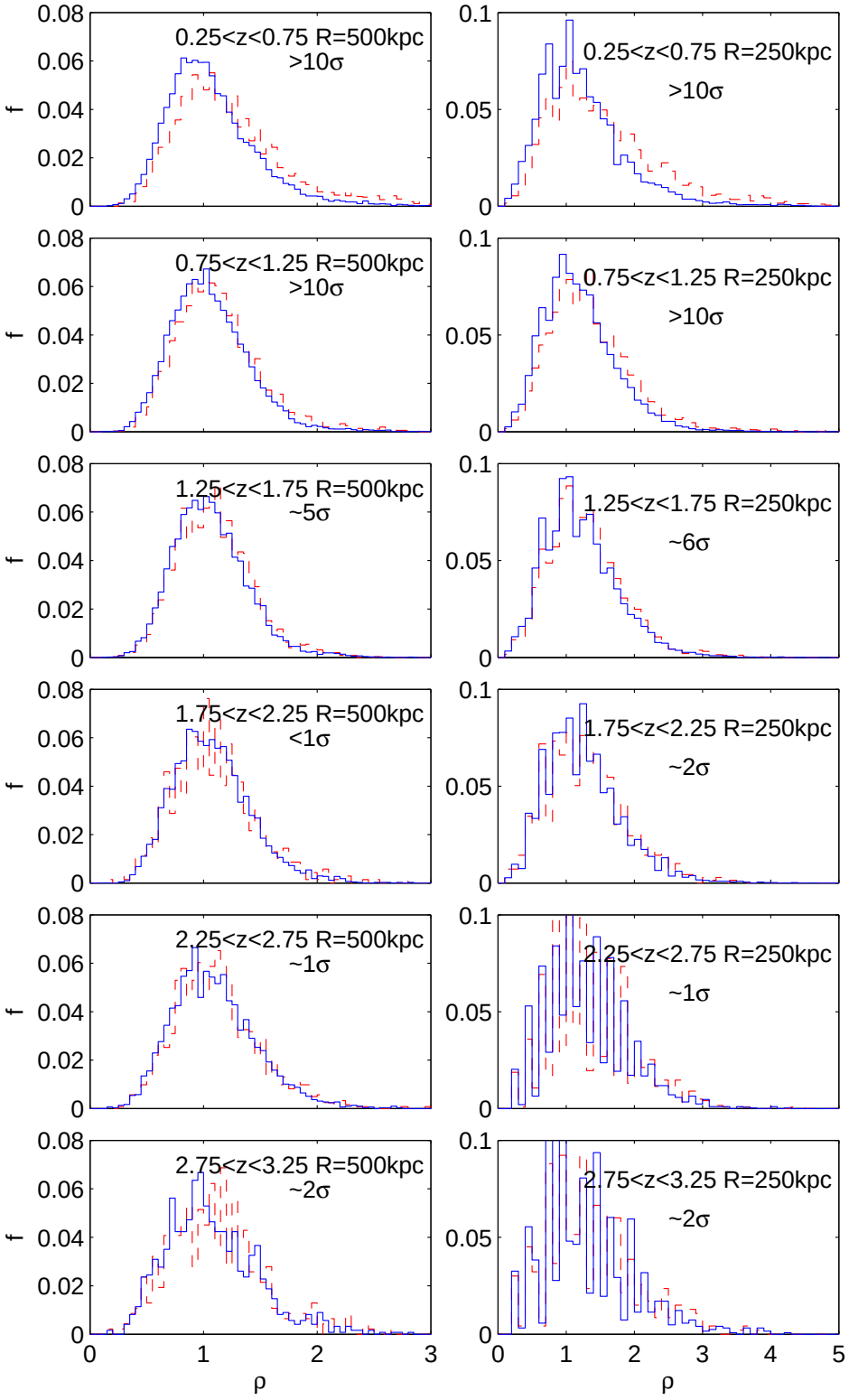

Figure 6.1. Histograms of the density of red (dashed line) and blue (solid line) galaxies in six redshift bins and two apertures. The σ values are obtained from a KS test, showing the significance in rejecting the null-hypothesis that the samples are drawn from the same underlying population.

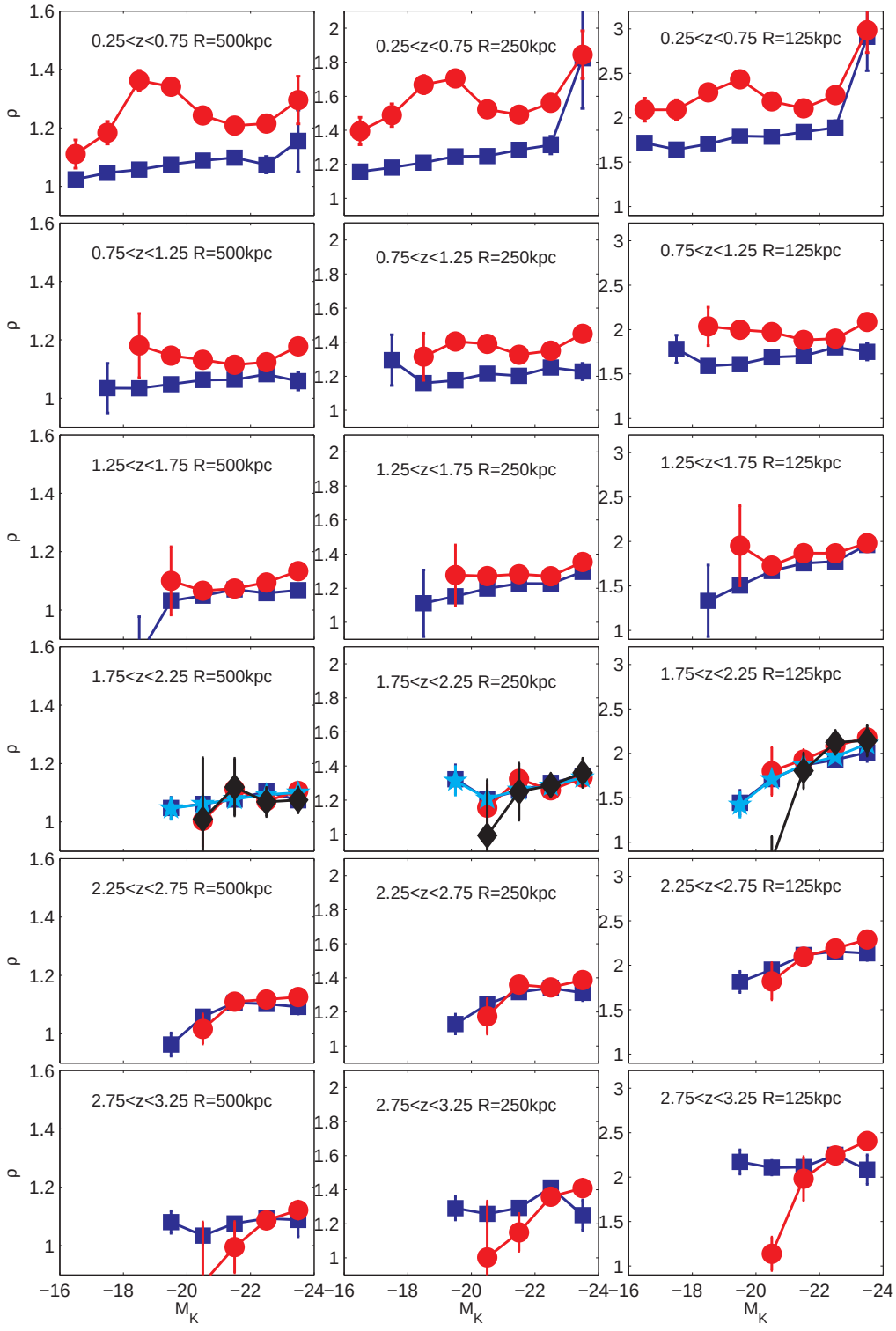

Figure 6.2. Plot of the average galaxy density against M_K, a proxy for mass, showing six redshift bins and three different aperture radii. Each panel shows the red (red line) and blue (blue line) galaxies with sBzKs (cyan line) and pBzKs (black line) (Daddi et al. 2004) shown in $1.75 < z < 2.25$. Note the change in y-axis values between the different apertures sizes.

columns and six redshift rows. This shows that bluer galaxies are in less dense environments than redder galaxies, with the density increasing steadily the redder a galaxy gets. This trend progressively weakens towards higher redshift until at $z \sim 2$ the trend is only apparent for the reddest galaxies and at smaller scales, although even this may not be significant. In the final redshift bin ($2.75 < z < 3.25$) there are only 1,898 objects with few red objects, so no solid conclusions can be drawn from this redshift bin. As also seen in the DR3 there is an abrupt change in the density of the lowest redshift galaxies at $(\text{U-B})_{rest}$ $\sim$0.7, indicating a sharp density change between red and blue galaxies. This may persist to higher redshift too but the sharp change is washed out due to less reliable colours, into the steady increase that we see. There is also a general trend that more luminous galaxies occupy denser environments. This is especially clear at $1.75 < z < 2.25$ where the luminosity rather than the colour seems to correlate with the density, in particular in the smallest aperture. An interpretation of this is that the luminosity-density relation may be present before the colour-density relation, in that more massive galaxies are at high density before their stellar populations are influenced by the environment. The massive galaxies may then become red due to the environmentally driven processes, although internal processes could also drive this. The luminosity density relation then weakens at lower redshift due to the accretion of fainter galaxies which later become red. For interest a similar plot to Figure 6.3 is shown in Appendix B plotted in 1 Gyr bins of redshift.

In summary we confirm what is seen at low redshift in the DR3 that red galaxies are on average in denser environments than blue galaxies, extending this to even higher redshift with the DR8. We find a significant difference between red and blue galaxies up to $1.25 < z < 1.75$, weakening or disappearing at higher redshift. In contrast, Cooper et al. (2007) found that at $z \sim 1.3$ that the environments of red and blue galaxies are indistinguishable. However this is likely to be due to their survey being selected in the R-band, meaning that they will be missing many red, passive objects at higher redshift. We find a similar result to Quadri et al. (2011) who found that the star-formation density relation exists out to at least $z \sim 1.5$.

6.3 Investigating Sources of Error

Here we investigate the various sources of error that can be introduced to this work through the definition of red and blue, the choice of method and sample used, cosmic variance and the photometric redshifts. Although the photo-zs have a very small uncertainty they can still dilute any environmental signal. To try and investigate the effect of the photometric redshift errors we perform Monte Carlo simulations of the data explicitly taking into account the fraction of outliers.

6.3.1 Colour Cut

To see if the empirical choice of rest frame (U-B) colour cut effects our results a theoretical colour cut was used (see Kriek et al. (2008) for more details). Figure 6.4 shows how this affects the environments of the red and blue galaxies in one aperture and six redshift bins. In comparison with Figure 6.2 it indicates that there are minor effects on the results of the different colour cuts but no effect on the conclusions drawn.

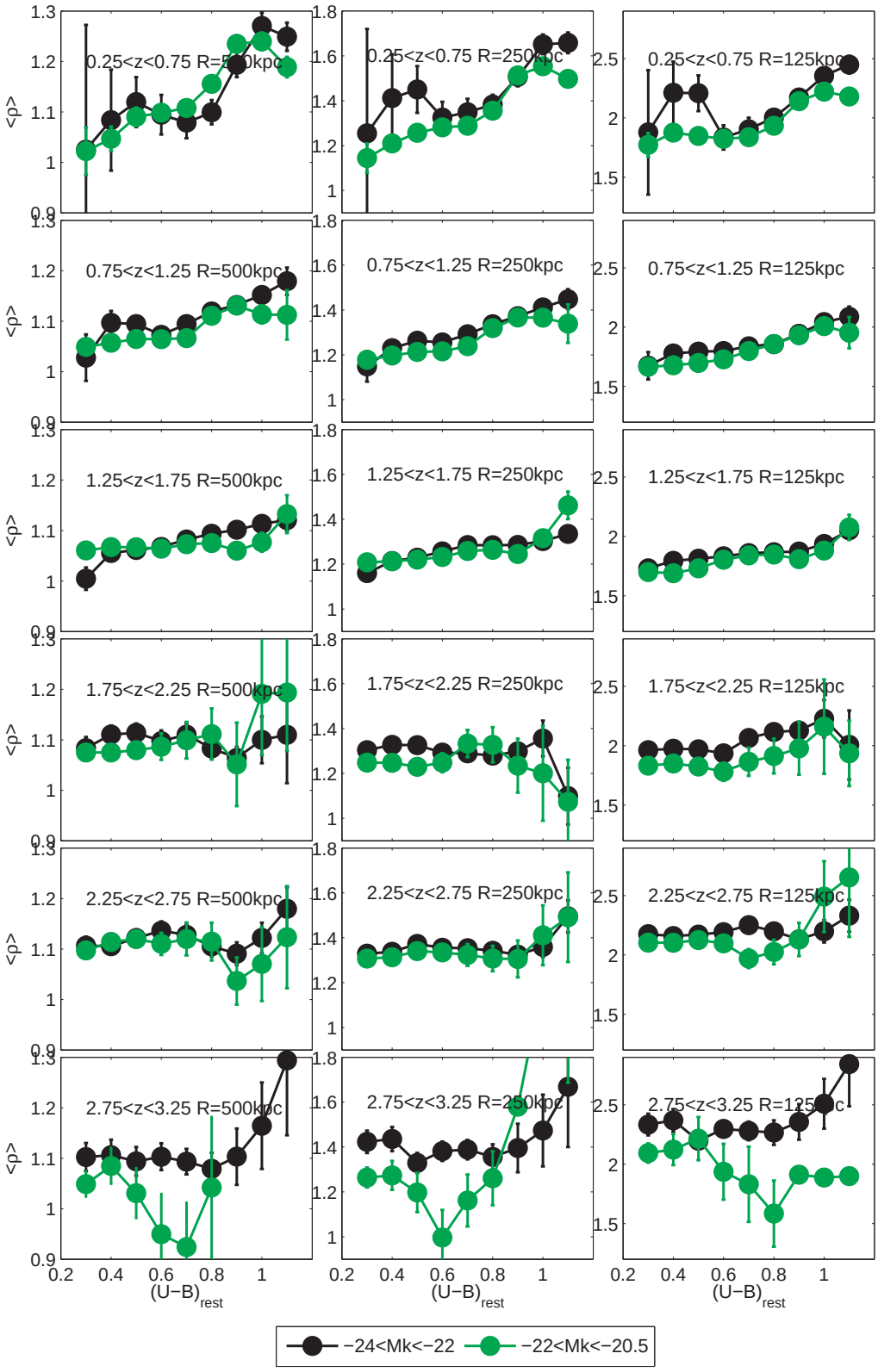

Figure 6.3. Average density of galaxies against (U-B) rest frame colour in six redshift bins and three apertures. Divided into bright and faint objects with -24< M_K <-22 and -22< M_K <-20.5 respectively.

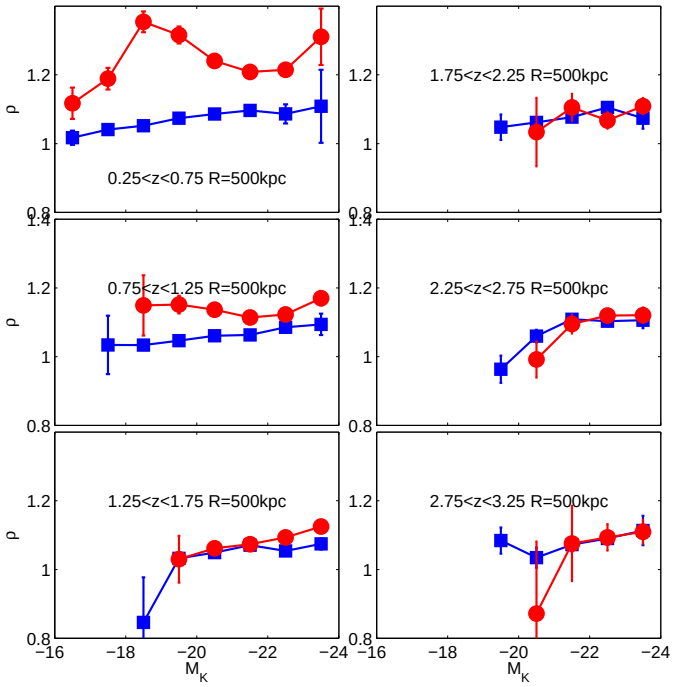

Figure 6.4. Average density of galaxies against M_K with a theoretical evolving $U-B$ cut calculated using Kriek et al. (2008). Only showing one aperture size and six redshift bins for clarity.

6.3.2 Volume Limited Sample

To investigate the influence of the flux-limited sample used throughout this study, we reduce the sample to only the brightest galaxies with $M_K \leq$-21.5. The environmental analysis is then repeated using only this volume-limited sample, which allows a fairer comparison between the redshift bins. This compares to the bright end of the galaxy distribution plotted in Figure 6.2. Figure 6.5 shows the red and blue galaxies in three apertures and six redshift bins. The measurements agree with the conclusions that red galaxies are in denser environments than blue galaxies up to $z \sim 1.5$.

6.3.3 Cosmic Variance

To try to quantify the effect of cosmic variance on our results we divide up the UDS field into four quadrants, with the median values of x and y used to divide up the field, as in Chapter 2. The results for two redshift ranges, $1.25 < z < 1.75$ and $1.75 < z < 2.25$ are shown in Figures 6.6 and 6.7 respectively. The average density of the red and blue galaxies is shown in each quadrant against M_K. The field is shown in the bottom left panel whilst the bottom right panel shows the overall result for the whole field. The error bars given are the error on the mean of the results in the four quadrants. In each quadrant of Figure 6.6 the densities of the red galaxies are comparable to those of the blue galaxies. However the red galaxies are on average higher than the blue galaxies especially at the bright end. Figure 6.7 shows a large amount of scatter with no significant difference between the red and blue galaxies in either quadrant. We conclude from this that although there is significant variation

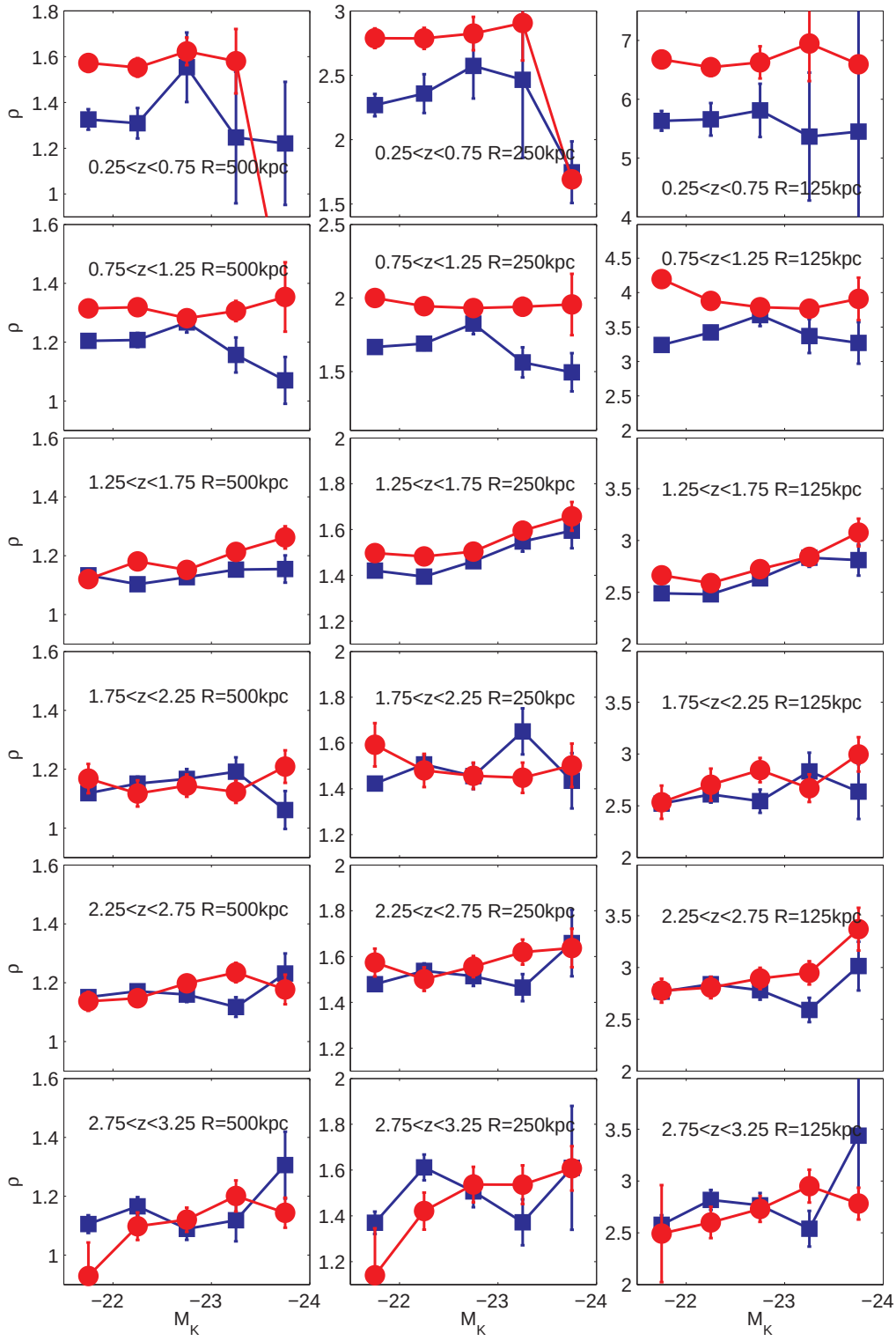

Figure 6.5. Plot of the density of galaxies with $M_K \leq$-21.5 in six redshift bins and three different apertures. Shows the red and blue galaxies in each subplot. Note the variable limits on the y-axis as they change to more clearly display the data.

over the field that the overall conclusions remain robust.

6.3.4 Environment Measures

To investigate the effect of using a different environment method, Figure 6.8 shows the results of using a 500kpc aperture with the density measurement from Chapter 2, Section 2.1.4. Once again this does not have a significant effect on the conclusions drawn form Figure 6.2. To test this further we use a nearest neighbour approach as defined in Section 6.1.4, shown in Figure 6.9. This generally illustrates the same as in Figure 6.2 but using third, fifth and seventh nearest neighbours as the density measure. One interesting difference between the apertures method and the nearest neighbour (NN) method is that in the NN method the luminosity-density relation for the blue galaxies is much stronger. This is particularly clear in the $0.75 < z < 1.25$ redshift range. This is in agreement with what was seen in the DR3 environments. This indicates that the method chosen to measure the environment does not effect the broad conclusions drawn.

6.3.5 Monte Carlo Simulations

To investigate the effect of photometric redshift errors on the environments derived we conduct Monte Carlo simulations. The photometric redshifts are randomised in two stages. Firstly all of the redshifts are given a random offset around zero with a standard deviation, $\sigma_{s.d} = 0.038(1 + z)$. This value was used as it is the spread calculated from the comparison between spectroscopic and photometric redshifts from Section 6.1.2. Figure 6.10 shows the photometric redshifts described earlier against spectroscopic redshifts from a variety of sources (Yamada et al. 2005; Simpson et al. 2006; Akiyama et al., in prep; Simpson et al., in prep; Smail et al., in prep) with a large proportion ($\sim$50%) from the UDSz described in Chapter 4. This accounts for the small errors in the photometric redshift calculations.
A second stage accounts for the photometric redshifts with large errors, the outliers. In this stage we randomly assign objects as outliers (objects with $\Delta z/(1+z) > \pm 0.15$) according to the outlier fraction determined from the comparison with the spectroscopic redshifts (see Figure 6.10). For objects with $z < 1.25$ we compute an outlier fraction of 3%, for $1.25 < z < 1.75$ we have 11% outliers and for objects with $z > 1.75$ we use an outlier fraction of 30%. In each regime 3%, 11% or 30% of the objects are randomly assigned a higher or lower redshift to simulate the large outlier fraction at these redshifts and the effect of scattering galaxies in and out of the redshift bins used for the local density calculation. These randomised redshifts were used to repeat the environment calculations with an aperture of 500kpc, 100 times for each galaxy.

The results of this are shown in Figures 6.11, illustrating the $0.75 < z < 1.25$, $1.25 < z < 1.75$ and $1.75 < z < 2.25$ redshift bins respectively. These demonstrate that photometric errors tend to dilute the distinction between red and blue but this dilution is comparable to the errors displayed previously. For the $0.75 < z < 1.25$ redshift range the simulations do not show much effect at all, with the red and blue galaxies still clearly separated. In the $1.25 < z < 1.75$ redshift bin the washing out due to the photometric redshift errors is comparable to that at $0.75 < z < 1.25$ but is not sufficient to undermine the conclusion that there is a convergence in

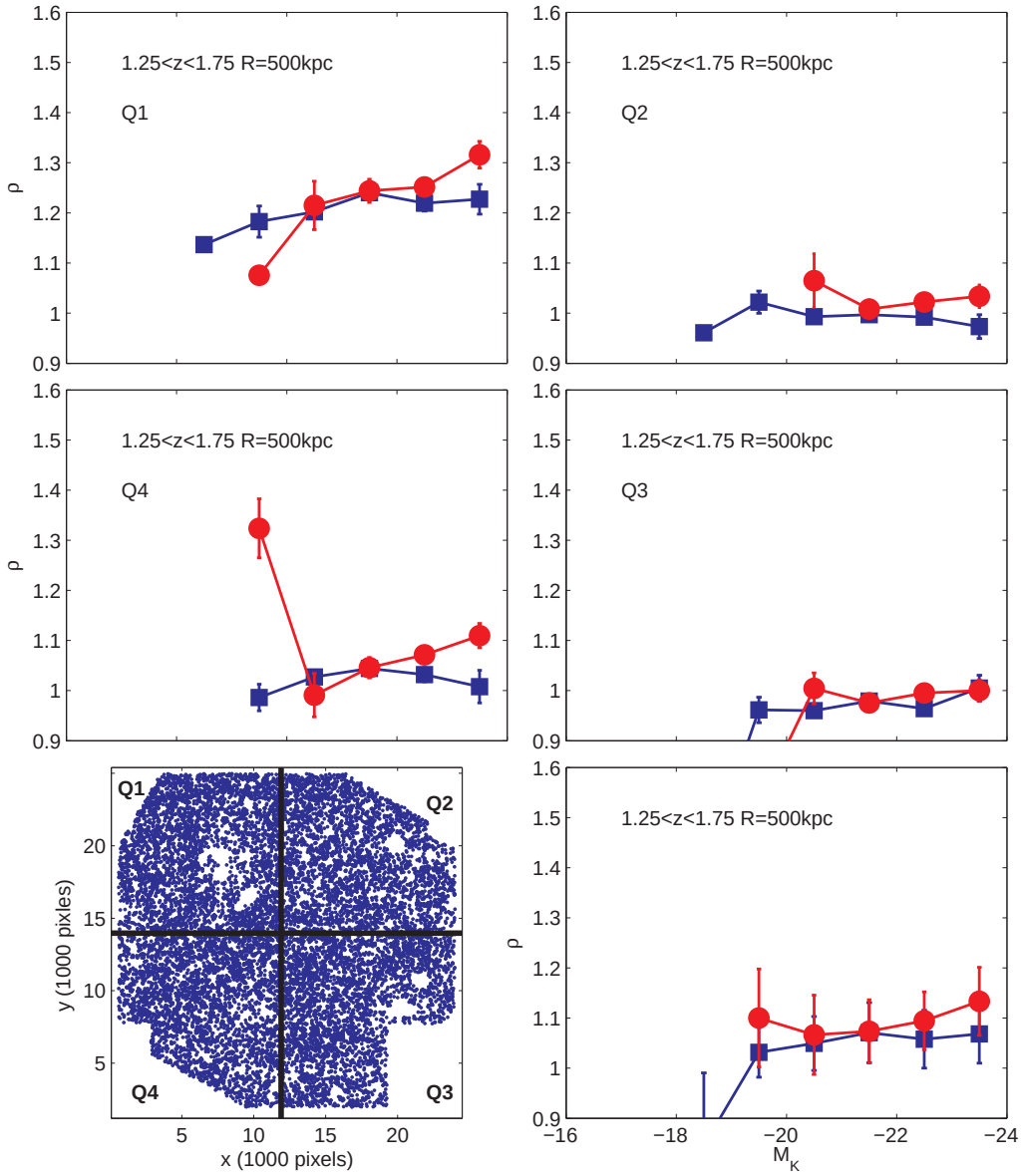

Figure 6.6. Plot showing the density of red and blue galaxies against K-band luminosity in four quadrants of the full UDS field (shown in the bottom left). The overall result for the field at $1.25 < z < 1.75$ is shown in the bottom right with error bars calculated from the error on the mean of the four quadrants to give an estimate for the cosmic variance.

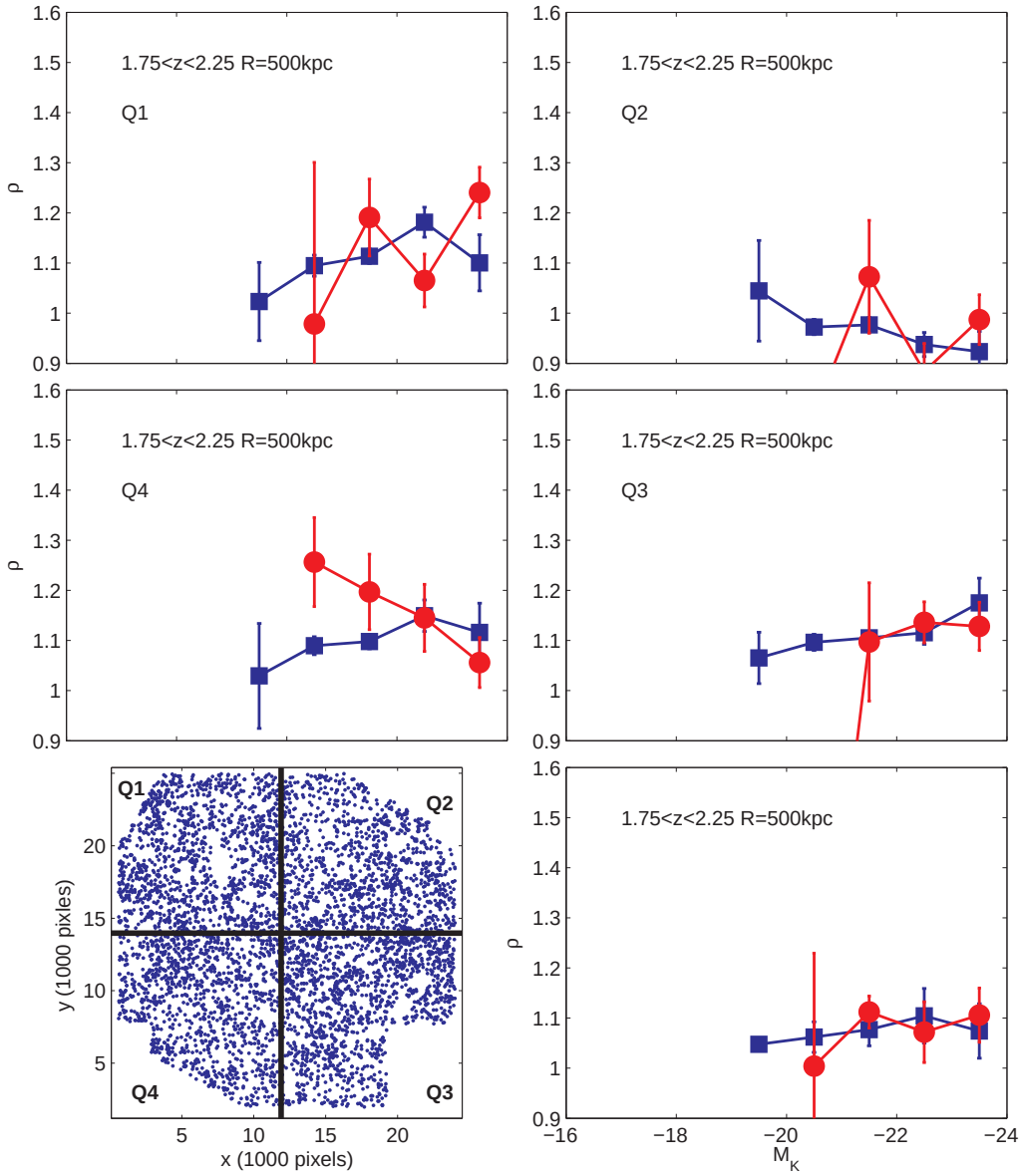

Figure 6.7. Plot showing the density of red and blue galaxies against K-band luminosity in four quadrants of the full UDS field (shown in the bottom left). The overall result for the field at $1.75 < z < 2.25$ is shown in the bottom right with error bars calculated from the error on the mean of the four quadrants to give an estimate for the cosmic variance.

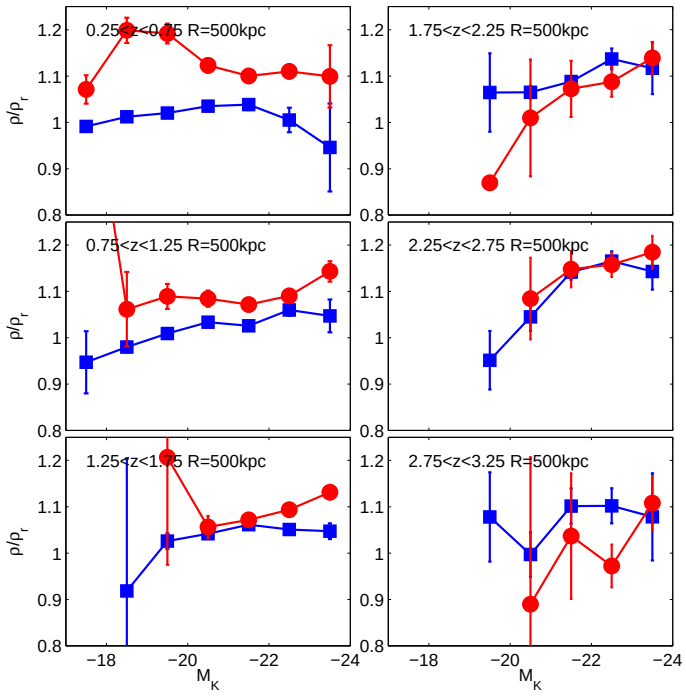

Figure 6.8. Density of galaxies against M_K using the same environments method as introduced in Chapter 2. Only showing one aperture size and six redshift bins.

environment. Even at the brightest end the difference with environment is still only a few percent even taking the most extreme simulations. At $1.75 < z < 2.25$ the simulations show that the washing out due to the photometric redshifts is larger but that there is still no visible distinction between the red and blue populations.

6.4 Conclusions

In this Chapter we have presented a study of the environment of over 68,000 K-band selected objects, furthering the work of Chapter 2. With the deeper DR8 data we have been able to go deeper in redshift, look at fainter objects and generally improve the analysis of the previous work of the DR3. The spectroscopic data (UDSz) has enabled us to use improved photometric redshifts and meant that we can, through the use of Monte Carlo simulations, constrain the errors induced by these to higher redshifts and with greater accuracy. We once again divided the galaxies into red and blue based on $(U - B)$ rest frame colours and used a more developed counts in an aperture to improve the density estimate. We find the following principal results:

1. We find a strong relationship between rest-frame $(U - B)$ colour and galaxy environment to $z \sim 2$, with red galaxies in denser environments than blue galaxies at fixed M_K. Beyond $z \sim 2$ the environments of red and blue galaxies become comparable, with a flat colour-density profile (see Figure 6.3). This agrees largely with work done by Quadri et al. (2011) who studied the star formation-density relation in the UDS. This work also broadly agrees with the

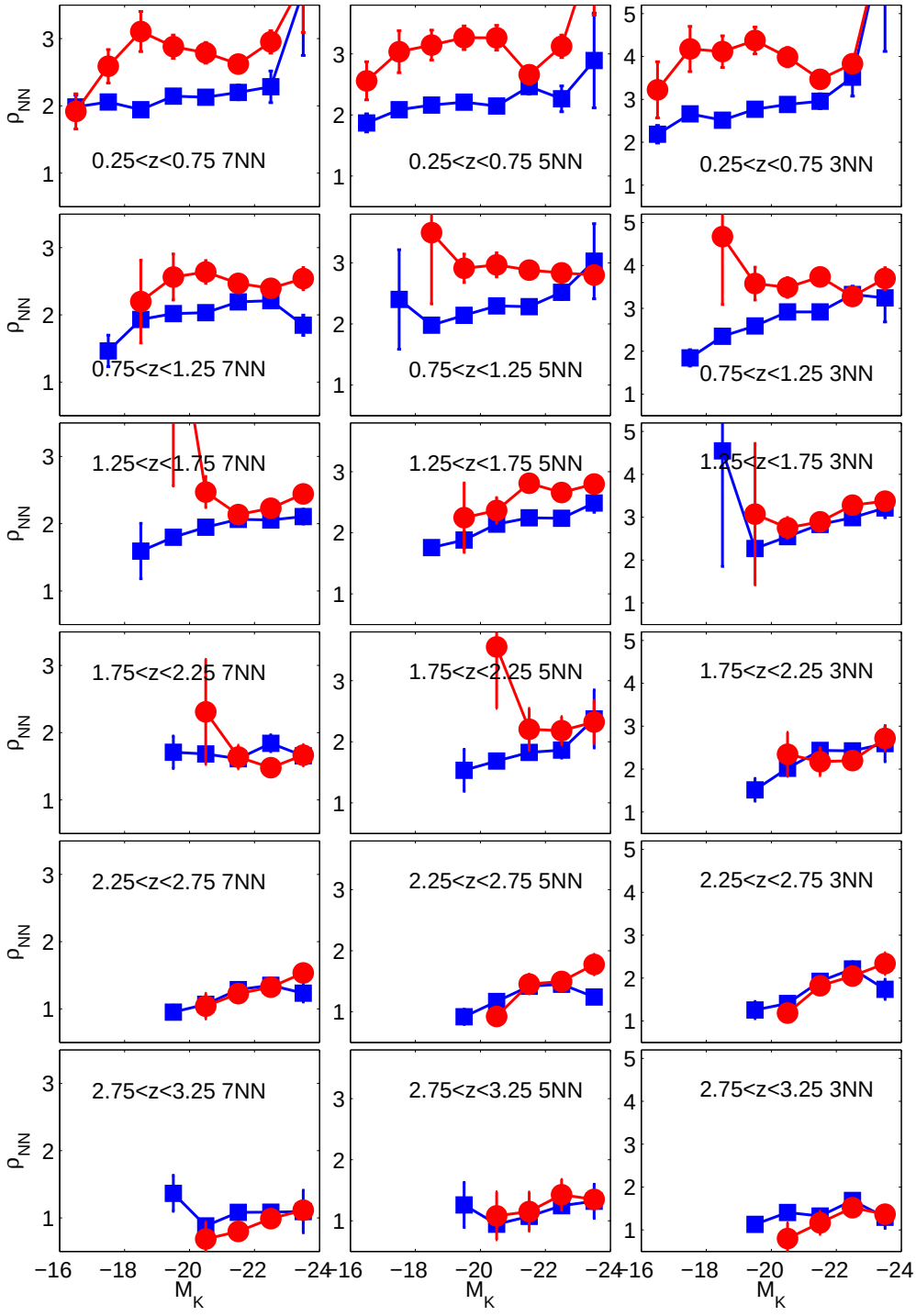

Figure 6.9. Plot of the nearest neighbour density of galaxies in six redshift bins and three nearest neighbour measures. Shows the red and blue galaxies in each subplot in the redshift range $1.75 < z < 2.25$.

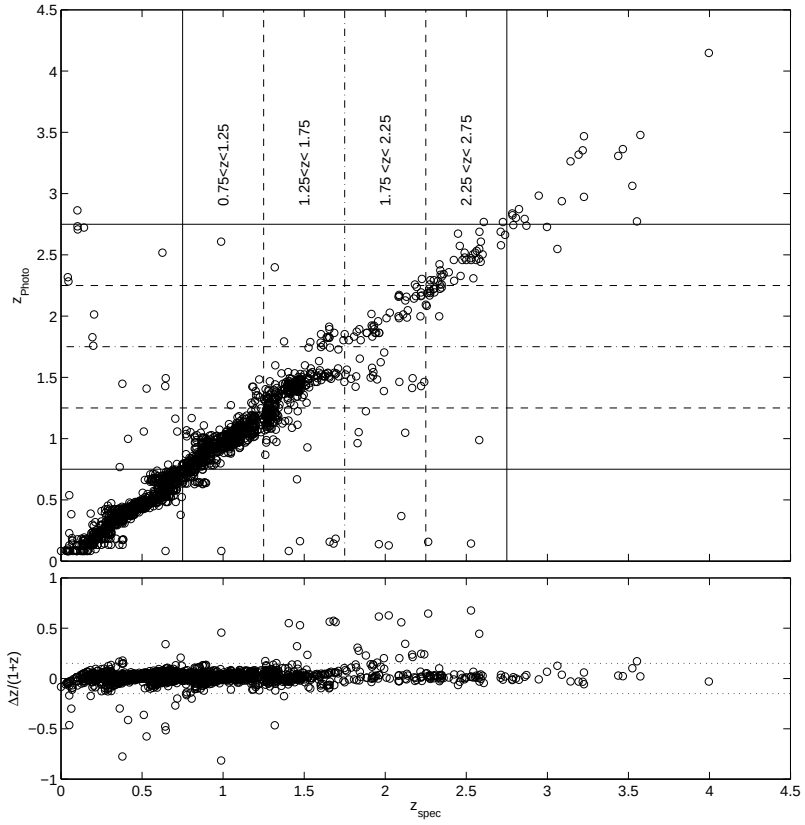

Figure 6.10. Plot of reliable spectroscopic redshifts against photometric redshifts highlighting the important redshift bins. The spectroscopic redshifts are from Yamada et al. 2005; Simpson et al. 2006; Akiyama et al., in prep; Simpson et al., in prep; Smail et al., in prep, with ∼50% from the UDSz described in Chapter 4. The difference that the UDSz data makes can be seen by comparing this figure with Figure 2.8.

conclusions of Chapter 3, that there is no strong colour-density relationship at $z > 1.5$.

2. We find only a slight correlation between the K-band luminosity and local density with the correlation strengthening on smaller scales. The relationship becomes very strong for the blue population on small scales at $1.25 < z < 1.75$ and $1.75 < z < 2.25$. Something similar to this was seen in the DR3 environments. These appear in good agreement with Cooper et al. (2007). This may be because we are observing the epoch at which star-forming galaxies become quenched, particularly in denser environments.

3. Faint galaxies seem to be strongly affected by their local environment at $z < 0.75$ with those in high density environments preferentially red. This is in good agreement with what was found from the spectral analysis of Chapter 5 and Quadri et al. (2011). For red galaxies in the local universe a similar effect has been seen, with faint and bright galaxies occurring in high density environments whilst more intermediate galaxies occupy lower density regions (for example Hogg et al. 2003). This maybe due to different processes occur-

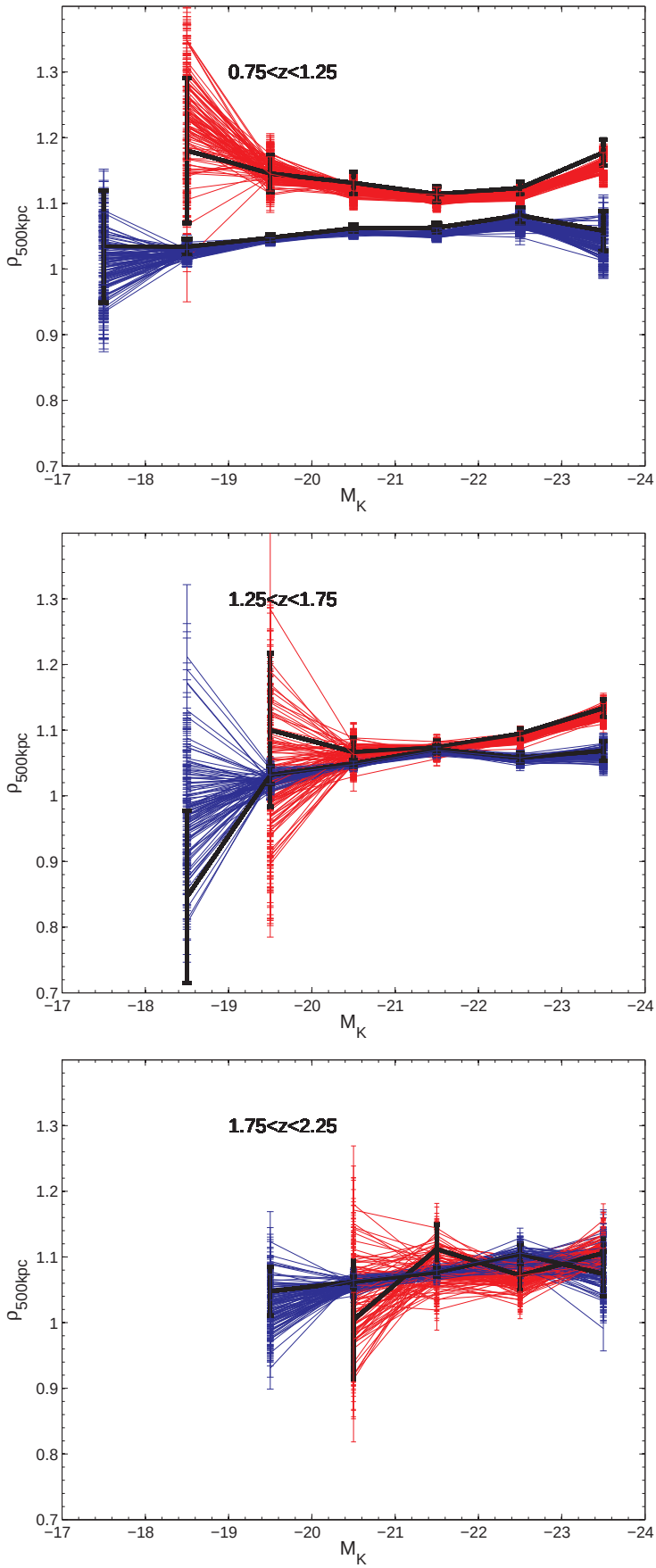

Figure 6.11. Plot of the Monte Carlo simulations using a 500kpc aperture for the $0.75 < z < 1.25$, $1.25 < z < 1.75$ and $1.75 < z < 2.25$ redshift bins. Showing all 100 simulations divided into red and blue galaxies with the thick black line indicating the original result (see Figure 6.2).

ring in different environments, for example faint, lower mass galaxies may be turned red by ram-pressure stripping in denser environments, removing their gas and thus source of star-formation, whereas for galaxies with intermidiate absolute magnitude this may not be the case, with maybe quenching from AGN becoming more dominant.

4. The volume limited sample (Figure 6.5) illustrates that even if only the brightest galaxies are used to calculate the environment, there remains a significant difference between the average environment of red and blue objects up to $z \sim 2$; with red galaxies in denser environments than blue galaxies. This figure also shows the strong luminosity-density relation for the objects in the $1.25 < z < 1.75$ redshift range. This shows that at this redshift and particularly at smaller scales the luminosity/stellar mass of a galaxy is strongly related to its environment. This is so strong that it is even larger than the difference in environment between red and blue objects at this redshift, maybe indicating that the stellar mass is the dominant driver here.

Chapter 7

Conclusions and Further Work

7.1 Conclusions

The primary aim of this thesis was to investigate the effect environment has on galaxies up to higher redshift than has been undertaken in the past. In Chapter 1 I discussed the work of other groups in this area and examine the various processes that have been proposed to explain observational data. I then investigate the effect environment has on colour in both the UDS and GNS fields up to redshifts of $z \sim 2$ and $z \sim 3$ respectively (Chapters 2 and 3). It is important in studies of environment to have robust redshifts in order to recover the distribution of galaxies along the line of sight. However the redshift range above $z \sim 1$ is only poorly covered by spectroscopic redshift surveys so far. The UDS Spectroscopic (UDSz) survey was undertaken to increase the number of secure redshifts in the critical redshift range above $z \sim 1$ and to improve the photometric redshifts for this and other work. I first describe the data reduction and redshift determination and then utilise the spectra from the UDSz to tentatively study if environment affects the spectral properties of galaxies up to $z \sim 2$. The study of environments is then brought to a close with the study of the colour-density relation between $0.25 < z < 3.25$ using the latest UDS data release (DR8). In each chapter I conclude what was found within that specific section. Here I will discuss the broader conclusions and summarise my work. Finally I shall look ahead to the directions in which this work could be developed and extended in the short and long term future.

7.1.1 Colour and Environment

Throughout this work we have investigated the relationship between colour and environment over a wide range of redshift ($0.25 < z < 3.25$) using both the UDS and GNS surveys. We have shown that there is a strong relationship between rest-frame (U-B) colour and local galaxy environment up to $z \sim 1.5$, with red galaxies residing in significantly denser regions than blue galaxies on scales of 1Mpc. The study of the galaxies within the GNS survey showed that between $1.5 < z < 3$ a galaxy's colour is barely influenced by environment, indicating that at $z > 1.5$ the colour-density relation is very weak, if it exists at all. These two studies were brought together in Chapter 6 using the deeper DR8 data from the UDS. We find that the colour-density relation weakens with increasing redshift until $z \sim 2$ where is becomes undetectable in our data. Figure 7.1 shows the colour-density relation for all three data sets used in this thesis; the UDS DR3 and DR8 (red and blue lines respectively) and GNS (black line). It shows the average density against (U-B) rest frame colour for the

full range of magnitudes avaliable in that redshift range. The colour and density were measured differently between the UDS DR3 and DR8, meaning that there are subtle differences between the two data sets, for example in the lowest redshift bin the DR8 goes much fainter than the DR3 and the change in redshift interval over which the environment is calculated is different (see Sections 2.1.4 and 6.1.4 for more details). Despite these differences this figure shows that the broad conclusions from each of the chapters agree, this strongly indicates that the result arises from astrophysical rather than some undiagnosed selection bias as the methods and selection criteria between the three data sets are different. The conclusion that at $z \sim 1.5$ the colour-density relation has weakened, if not disappeared is present in all three of the data sets.
Interestingly this is the epoch in which McGee et al. (2009) predict that galaxy groups and clusters will display little or no environmental effects. They use semi-analytic models to examine accretion of galaxies into groups and clusters. They argue that strangulation, the slow removal of gas from galaxies as they fall into a cluster or group, is responsible for changing the properties of the galaxies. This process is supposed to be independent of halo mass and occurs over time scales of several Gyr so that at high redshift this will not have had time to affect the galaxies until $z \sim 1.5$. It is also worth noting the hydrodynamic simulation by Kereš et al. (2005) who predict that lower star formation rates in the highest over-densities will be detectable up to $z \sim 2$ but not earlier. They study the cold gas accretion rates of galaxies in the early universe. They find that the different timescales of gas accretion and heating in different environments naturally produces the relations with local density we observe up to $z < 2$ as well as the strengthening of those relations with cosmic time.
Other mechanisms proposed to explain the observed relationship between environment and colour such as ram-pressure stripping, galaxy harassment and global tidal interactions occur preferentially in cluster environments. Since we do not probe a large number of clusters it is unlikely that these processes can explain our findings. Note also that we see the environmental dependence of galaxy colour over all scales of environment we study here, suggesting that the extreme cluster environment is not needed to produce the colour-density relation.

In the study of environments using the DR3 we selected 'passive' and 'star-forming' objects using template fitting. This showed that passive objects occupy slightly denser environments than the red population at all epochs. This indicates that the passive subset of the red galaxies are responsible for the enhanced environments compared to blue galaxies. The remainder of the red galaxies may either be not as old/slightly star-forming or be dusty star-forming objects but it is hard to comment on these with the current data.

7.1.2 Luminosity and Environment

We observe a positive correlation between galaxy K-band luminosity (a good proxy for stellar mass) and local density, especially on smaller scales (aperture radius of 125kpc) and for galaxies at $z \sim$1.5. It also seems to be strongest for blue galaxies in this regime, with the most luminous blue galaxies at $z \sim$ 1-2 showing average environments comparable to red galaxies. The results from the GNS survey also showed that there is a large population of blue galaxies in the most over-dense regions at a redshift of $z \sim$1.5. The results agree with, for example, Cooper et al.

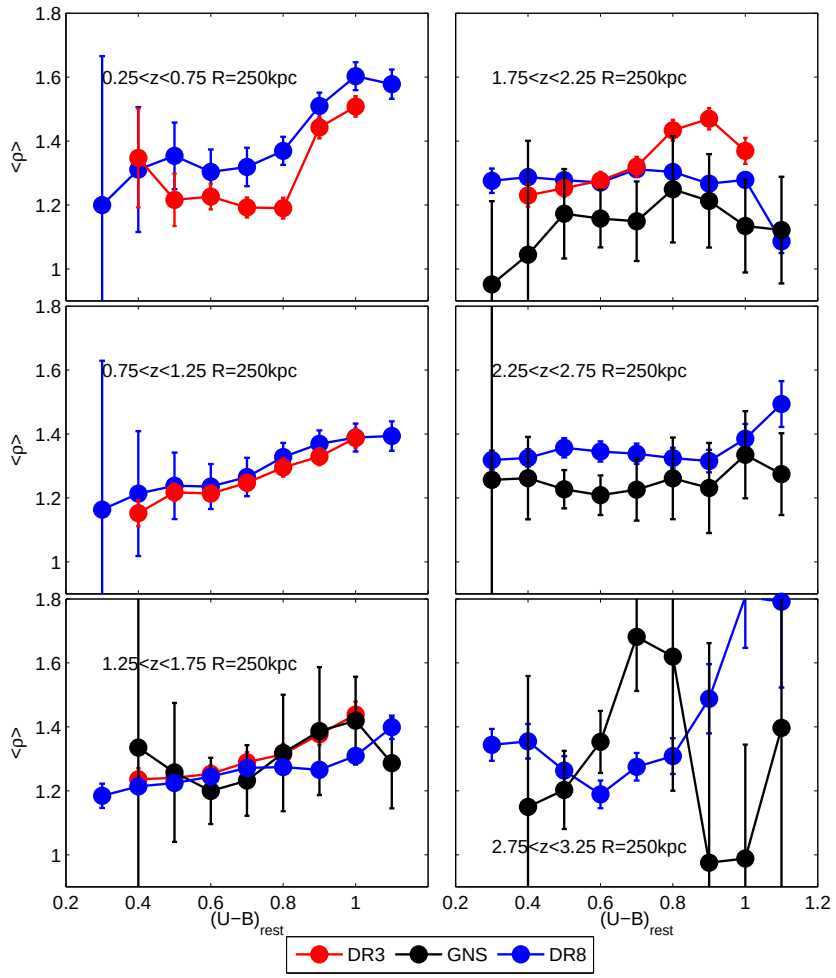

Figure 7.1. Average density of galaxies against (U-B) rest frame colour for the DR3 (red line, Chapter 2), GNS (black line, Chapter 3) and DR8 (blue line, Chapter 6) data sets. Using the full range of magnitudes within the data and showing six redshift bins and the 250kpc aperture only.

(2006) who found a similar relationship with DEEP2 data.

Another interesting result is that for the red galaxies the brightest and faintest objects have a similar average environment, whereas the intermediate luminosity galaxies are in lower density environments (see Figures 2.3 and 6.2). This is known in the local universe (e.g. Hogg et al. 2003) and has recently been seen at higher redshifts by Quadri et al. (2011). They argue that this is due to different processes shutting off the star-formation in different densities, for example in intermediate masses AGN feedback may play a larger role. They also suggest that environment may play a greater role in the build up of the red sequence at lower masses (van den Bosch et al. 2008) as their study of satellite galaxies indicates that they were red even before they became satellite galaxies. It may also indicate that for the faint red galaxies a cluster-specific process like ram-pressure stripping is key, acting most efficiently on the faint galaxy population falling into clusters.

7.1.3 Spectral Properties and Environment

In Chapter 5 we undertook a preliminary investigation of the effect environment has on the spectral properties of galaxies. Using the spectra described in Chapter 4 we explore whether there are any correlations between features like the 4000Å break (D4000), the strength of [OII] (EW[OII]) and other age/metallicity indicators. From measuring the strength of the D4000 we can confirm that our U-B colour selection is robust, in that red galaxies have a larger break strength, as expected. What is suprising is the ability of the C(29-33) index to separate the red and blue objects. This index is an indicator of the number of very young stars compared to the number of young stars, with higher values indicating fewer very young stars. This index is a very good way of separating red and blue galaxies at bluer wavelengths, where the colour information given by the Balmer break is not available.
The results of this work are very tentative, with only four statistically significant differences between high and low densities. In the $0.45 < z < 0.75$ redshift range both the D4000 and C(29-33) indices show a 2σ difference between high and low density samples, such that the higher density sample has significantly higher values for both indices. This trend also extends into the red objects, meaning that red galaxies in denser environments have stronger D4000 breaks. In the $1.25 < z < 2.2$ redshift bin we see that the EW[OII] and C(29-33) indices show 3σ and 4σ differences respectively, showing that at higher densities the [OII] intensity decreases and that the C(29-33) index increases markedly. The results in the intermediate redshift bin ($0.75 < z < 1.25$) seem to indicate that objects in lower density exhibit stronger breaks and larger C(29-33) indices than in the higher and lower redshift bins. The separation between red and blue objects is still strong, however, maybe indicating a weakening in the colour-density relation. This is not fully understood and could be due to lower signal to noise spectra or lack of a large enough statistical sample.

The work carried out here suffers from a few selection effects, for example we have a limited dynamic range in environment due to the mask design and because we are only sampling a small fraction of the galaxies in the UDS field. We may therefore be missing effects that occur in more extreme environments. We are also missing the oldest, reddest objects at $z > 1.5$ as these are beyond the reach of the VIMOS and FORS2 instruments. In the lowest redshift range ($0.45 < z < 0.75$) we may also be looking at a fainter subset of galaxies as slits were placed on galaxies that didn't already have a spectroscopic redshift from other surveys.

From this work on environment we can see that it is not just stellar mass that plays a roll in determining a galaxy's colour but also its environment. A galaxy's halo mass will also be strongly linked to a galaxy's environment and its stellar mass, as a more massive halo will accrete more gas/dust and is likely to affect other gravitational potentials around it. Cooper et al. (2010) also stated this and went on to say that it is the relative importance of these two evolutionary drivers that is now the difficult task. The relative importance of each effect may change with redshift, maybe becoming more mass driven at higher redshift for example.

7.1.4 The Spectroscopic UDS Survey (UDSz)

In Chapter 4 I discussed the data reduction and redshift determination for a sample of ∼3500 UDS galaxies observed with the VIMOS spectrograph on the VLT.

Including serendipitous detections we obtain 4679 K-selected spectra. Using template fitting and careful visual inspection we have been able to obtain ∼1600 reliable redshifts in the range $0 \leq z \leq 3.99$. The survey also used the FORS2 instrument, which is more sensitive at redder wavelengths, to obtain ∼290 highly secure spectra around the redshift desert, between $1.2 \lesssim z \lesssim 2$. The UDSz has increased the redshifts available at $z > 1.5$ by a factor of 10 and approximately doubled the redshifts avaliable at $z > 1$, making the derivation of photometric redshifts at higher redshifts much easier, as well as enabling us to understand their errors much better.

7.2 Future Work

Here I look ahead to the directions in which this work could be developed and extended in the short and long term future.

7.2.1 Short-term

In the short term this work can be developed and extended in a few simple ways. For example we could use the nearest neighbour method more extensively as it is widely used in the literature (e.g. Cooper et al. 2007; Grützbauch et al. 2011). We chose not to use it here as the aperture method is conceptually more simple and is less affected by the holes and edges in our survey. The choice of method makes no difference to the conclusions, as we have shown but it would allow better comparison to other peoples work and it may have a wider density range and be more sensitive to variations on small scales. The number of neighbours to count is open to debate and depends on the scale and characteristics of the structure you want to study (Cooper et al. 2005) but most groups use the third nearest neighbour.
Deeper J,H and K data is still being acquired as the UDS continues to at least 2013, which will improve the depth of the survey even further than was shown in Chapter 6. This will improve the photometry and increase the number of objects, especially for fainter galaxies and at higher redshifts. This improves the environments as it increases the number of tracer galaxies, constraining the environments further. The photometric redshifts within the DR8 are currently being improved by Ruth Grützbauch and collaborators. The reliability of photometric redshifts in studies like this are very important as a significant error in the photometric redshifts can easily wash out the environments. This process also allows us to derive stellar masses of the galaxies we study. The use of these stellar masses rather than galaxy luminosity may also be worth investigating. It is unlikely to have much effect but the stellar mass is a more fundamental quantity and may be important for more passive galaxies as they are more massive but are not as luminous as large star-forming galaxies.

A robust selection criterion for passive galaxies at higher redshifts would allow us to study the environments of passive and star-forming galaxies. This was done in Chapter 2 and it would be interesting to explore this in the DR8 and further data releases. Finally for the spectroscopic environments study shown in Chapter 5 it may be worth utilising the less robust 'flag 2' objects. This would increase the sample size and may help to improve the significance of the results and conclusions that can be drawn. The lower signal to noise of the individual spectra may, however, reduce their usefulness. In Chapter 5 we used the DR3 data; it would be worth exploiting the

DR8 data for this study to improve the environmental measures further, especially over a higher redshift range.

7.2.2 Long-term Outlook

In the longer term other surveys may hold the key to advancing the work undertaken in this thesis. In December 2009 the Visible and Infrared Survey Telescope for Astronomy (VISTA) instrument became operational and two of its projects are of particular interest to this work. UltraVISTA is the ultra-deep project for VISTA, with a target depth of K=25.6, it will go deeper (in J and H) than the UDS over a larger area (1 $\times$ 1.5 degree field). This will enable it to probe to high redshift and critically over a larger area, allowing a better understanding of the cosmic variance and increase the number of sources, thus reducing the Poisson errors of the measured values and improving the robustness of the environmental measure. The other project using VISTA of interest is the VIDEO (VISTA Deep Extragalactic Observations) survey. This is a much larger field covering $\sim$12 degrees^2 to a target depth of K$\sim$23.5. This would enable us to study a wider range of environments and thus investigate more extensively the cluster environment. Another survey of note here is the CANDELS (Cosmic Assembly Near-infrared Deep Extragalactic Legacy Survey) project. The observations have now been completed in the UDS field using the near-infrared WFC3 and optical ACS cameras on the HST. The extreme depth and resolution of this survey would enable us to develop this work to study the morphology-density relation and to explore if environment has any effect on the size evolution of galaxies.

Finally obtaining more spectra in the UDS field to increase the spectral sampling rate would improve the significance of the results in Chapter 5 and allow us to study a greater range of galaxies and galaxy environments. The FMOS (Fibre Multi Object Spectrograph) and KMOS (K-band Multi-Object Spectrometer) instruments will both revolutionise the acquisition of spectra needed to develop this study. They are both near infra-red instruments which will reduce selection biases compared to optical instruments and they both have the ability to cover a large number of targets in one observation.

The field of galaxy environments, much like the global environment, is set to get a lot hotter.

"Humour is something that thrives between man's aspirations and his limitations."

– Victor Borge

"I always wanted a quote in someone's thesis"

– Emma Bradshaw

Appendix A

Data Reduction Appendix

A.1 VIMOS Reduction

A more detailed, step by step analysis of the data reduction process is discussed below. The full manual for VIPGI can be found here: http://cosmos.iasf-milano.inaf.it/pandora/docs/vipgi/VIPGI_manual.pdf.

A.1.1 Unpacking

VIPGI needs a directory structure set up with archive, raw, parameter, tables, mos, catalogs and calibration directories within it. The software is then made aware of the data using the configuration panel in the Pipeline menu of the GUI. This also contains the Preferences section where other preferences can be set for example which programs it uses to load images in. The raw files are given the name VIMOS.yyyy-mm-ddThh:mm:ss.ddd.fits where the numbers represent the time when the file was written into the archive, for example VIMOS.2008-10-27T05:43:47.874.fits. For ease VIPGI unpacks these into the correct quadrant, catagorises and renames the files. The file types can be Bias, Flat field, Calibration Lamp, Standard star or Science frame, this information is stored in the header at the time of observation. The file types along with the name of the ADP file used to create the masks is used to create the new name, which is given the form CC_ADPname_Qn_m.fits where CC is the type code with: sc for science frames, ff for flat fields, lp for lamp frames, bs for bias and ms for master calibration files. The n indicates which quadrant it is from and the m is the exposure number of the sequence, for example sc_v8_LR_Red_Q1_1b.fits is a science frame, with a mask ADP called v8_LR_Red, is in quadrant one and is the first exposure. Once unpacked the data is displayed as shown in figure A.1. The calibration and stacking of the data can then commence quadrant and pointing at a time. This has to be done as each quadrant has its own response and thus needs to be treated separately from the others.

A.1.2 Standard Stars

For each observation a standard star is used to flux calibrate the final spectra. This is done so that the response of the CCD can be removed and the final spectra shape can be used as part of the redshift identification. VIPGI automatically identifies observations of standard stars and appends a table containing magnitudes vs wavelength; an SPHOT (spectrophotometric calibration) table. If this SPHOT table is not appended they can be obtained from http://www.eso.org/sci/observing/tools/standard

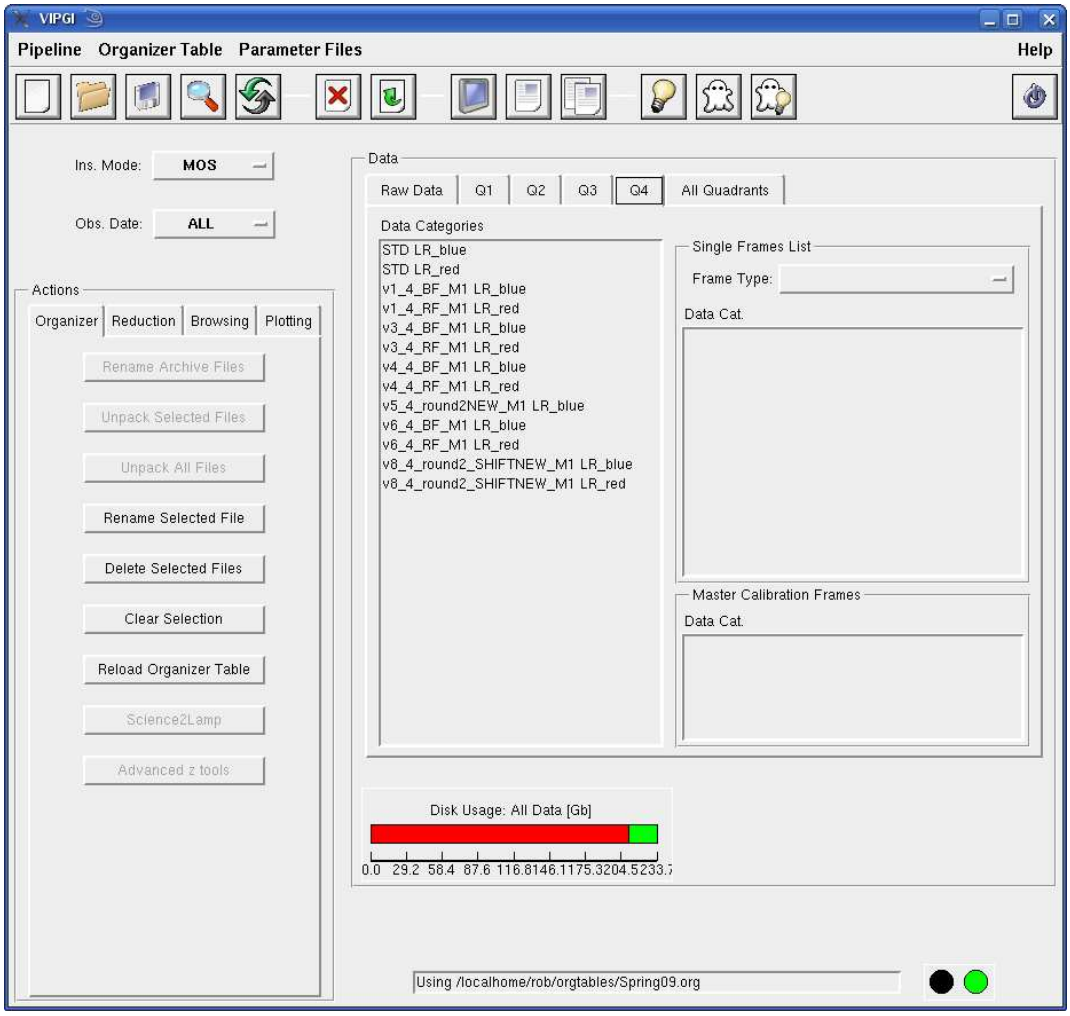

Figure A.1. A screen grab of the VIPGI GUI displaying some unpacked data and the setup of the GUI itself.

s/spectra/stanlis.html which gives an RA ordered list of targets. A ".dat" file can be downloaded from here, saved as an ascii file and using the pipeCreateSphotTable command it can be made into a ".fits" SPHOT table. These can then be appended to the Standard star file by using the command VmAppTable for example VmApptable VIMOS.2007-11-04T00:13:20.566.fits SPH_ngc7293.fits.

The raw standard stars are then corrected for bias and flat fielded, which gives a BFC file (see following sections for more detail). It is important when creating the msFlat and msLamp for the standard stars to set the Input type to STANDARD. These files must then go through the "preliminary reduction" step by selecting the BFC file, masterLamp (msLamp) of the standard star and pressing the Compute Spectrophotometry button under the Parameter Files menu. This process gives a "Tab" file which will be used to flux calibrate the reduced science spectra later in the process.

A.1.3 Science data

A Master Bias (msBias) file has to be created before commencing the rest of the reduction steps. Bias frames are taken to monitor the CCDs and are routinely taken every night (http://www.eso.org/observing/dfo/quality/VIMOS/pipeline/recipe_calib.html). The bias files are selected that are relevant to the observation and using the Create Master Bias button in the Reduction section of the GUI the msBias file is created. This is then displayed in the Master Calibration Frames section. The recipe for all of these steps can be edited in the Parameter Files menu and launched from there via the GO button.

First Guesses

The reduction recipes in VIPGI rely on a set of first guesses read from the primary header of the fits file. It is important that these first guesses are reasonable as it effects both the wavelength calibration and the extraction of the spectra. These checks are done by selecting Adjust First Guesses in the browsing menu. One flat frame and one lamp frame are selected that coinside with the science frame. In Adjustment type select "Check Line Cat" and hit Run. This brings up a ds9 window with the current line catalogue superimposed in red (and green). These can be moved around by going to the Region menu and Select All, once you have finished this go back to the menu and select Select None. Inspect the green lines and if they do not lie over an arc line delete it, making sure not to remove too many as these are used for fitting later. When this is done click YES in the Question panel, then exit the loop by clicking NO. You can then save this to the selected files by choosing Selected Frames in the Save results into section and clicking save.

The next thing to check is if there are any shifts between the first guesses and the data. This is done by choosing "Shift Only" in Adjustment Type and clicking Run. This again displays a ds9 window but with all the lines (in green) superimposed over the arc image. These can be moved until they lie over the according lines and spectra edges. To finish and save the results do the same as in the last adjustment. You then need to check if the data is rotated but choosing "Rotate" from the Adjustment type menu.

Next select "Choose Lines" from the menu. This allows the user to refine the first guesses on the dispersion by choosing some representative lines. Delete lines that are not needed for a rough first guess, it is best to leave the first and last lines and 4-5 lines in between which are well spaced and well aligned.

Next select "Complete Adjustment" from the menu. This allows a final check so the user can ensure that all the green lines fall on, or as near as possible to the real arc line in the ds9 image. Click YES and a new set of guesses will be calculated, when finished click NO. Once you have finished the first guesses stage you can either Save and Exit or Quit from the First Guesses Adjustment window.

Creating the Master Flat and Master Lamp

The flat files for each observation are then used to trace the spectra on the CCD and to create a master flat (msFlat) although in most cases a mock flat with all the pixel values set to 1 is used as otherwise this makes the fringing worse. To do this set the frame type to "flat", choose the flats that were taken in the observation that you are reducing and a msBias file. Then either go to the Parameter Files menu

to inspect the parameters used and press GO or simply click the Locate Spectra button in the Reduction Actions section of the GUI. To check that the spectra have been correctly traced, select a flat frame used in the last step and the msFlat file and click on "Check Spectra Location" in the Browsing section. This displays the flat frame with white lines overlaid which show the region containing the spectrum. Check that they correctly trace the spectra, if they don't you may have to re do the first guesses or increase the value of the parameter "Extra pixels from expected position of spectrum".

A Master Lamp (msLamp) can then be created using a lamp frame, the previously created msFlat and msBias, and then press "Create Master Lamp" button or go to the Parmeter Files menu. This uses the msFlat frame to find the spectra on the CCD with a maximum shift from expected position set in the parameter file. It uses the first guesses in the header of the msFlat to extract a window around the expected position of each line in the Line Catalogue and finds the peak of the arc lines. It then fits a 3rd degree polynomial and stores the results in the msLamp file. To check that the solution to the wavelength calibration is reasonable select the lamp frame and msLamp and click "Check Master Lamp" this displays a ds9 window with the solution overlaid over the arc image. Check the whole image to see whether is solution is reasonable. The wavelength calibration can be further refined and checked by selecting the msLamp file and clicking on the "Show Lambda Calibration" button in the Plotting section. This allows a slit by slit inspection of the wavelength calibration and allows you exclude a line from the lambda calibration, making sure to click refit when you are happy. A summary of all the slits RMS values can be seen by selecting Graph Type "Summary". It is important to make sure that the wavelength calibration is good ($\sim 1/7$ th of a pixel) so that the spectra are combined properly and it is also worth noting that it is important to make sure that there are as many calibration points as possible as this also makes the calibration more stable and accurate. For both the LR_Red and LR_Blue an average RMS of $\sim$1.1Å was obtained for our data. When you have created the msFlat and msLamp and you are happy with the result you can move to the next step.

Preliminary Reduction

The next step is the Preliminary reduction, this subtracts the bias frame, trims the pre- and over-scan and appends the extraction table from the Flat field to the specified frames. Select the science frames and the respective the msBias and msFlat and click the Preliminary Reduction button or choose it from the Parameter Files. This gives a file (or files) with the suffix BFC. Each science frame observation is treated with its own flat file to increase the reliability of the final stack.

Reduce Single Observation

The "Reduce Single Observation" section reduces science files that have already been located and bias subtracted. Select the science file or files that you want to reduce and select the standard star Tab file and msLamp and click the "Reduce Single Observations" or go to to the Parameter Files section. This outputs files with an extra R suffix. This section performs the following steps:

– If, as in this case the Shift lambda cal option is set to YES, the wavelength calibration is refined using some sky lines as references.

- Objects are then detected on the image. Each slit is collapsed along the dispersion axis (excluding the brightest parts to avoid zero orders etc) with the parameter "Spectrum fraction to be collapsed" defining the percentage of the spectrum used. From this a slit profile is created and a detection level is set by "Object detection level in units of sigma" above the mean profile level.
- The background is subtracted using (in this case) the median value of the profile outside the objects region.
- 1D and 2D spectra are extracted and are stored in the file extensions, EXR1D and EXR2D respectively.
- Sky residuals on either side of the object are extracted and quadratically combined with the Poissonian noise of the object to obtain a noise spectrum for each object.

Reduce Sequence of Observations

In the final step, all of the files from each of the observations (5 in the blue and 3 in the red) are combined together into one file, called the ".seq" file. All of the BFCR frames for this sequence, a master lamp and a dummy flux calibration file are selected. A dummy flux calibration file, with all the magnitudes set to zero is used to preserve the flux calibration from the Reduce Single Observation stage and to allow VIPGI to produce a flux calibrated spectra. In the parameter file set the "use already extracted spectrum" to YES so that it does not extract the spectra again. This reduction step does the Fringing correction, this uses the sky subtracted, wavelength calibrated images of each slit combined together. The object is masked out, then the slits are combined together without applying any shifts, so that the object is washed out and what remains is an image of the fringing, which is then subtracted.
The final ".seq" file contains all of the 2D and 1D calibrated spectra, information about the targeted objects, data about the signal to noise as well as some other less important parameters. Fifteen to twenty well exposed spectra are then selected (in the red only) using the "Show Single Spectrum" button in the Plotting section by ticking the box in the bottom left corner of the pop up window. This creates a ".slits" file which the Apply Atm. Correction button uses to identify and stack the bright objects and from them derives an atmospheric correction for the data. A summary file including the object data, S/N, magnitudes and other parameters can then be produced from VIPGI using the Show Reduction Results button in the browsing section. This requires a ".dat" file in the Catalogue directory with the format OBJID RA DEC MAGNITUDE to include the magnitude data in the summary file. A schematic of the whole pipeline is shown in Figure A.2

1D spectra can then be extracted using the Split 1D Spectra within VIPGI and the 2D spectra can be extracted using the split2DSpectra.py python script.

A.1.4 Redshift Determination

As p[art of the redshift determination we used EZ. This was run from the command line by using a list of all the spectra with the format 1Dspectraname.fits 1Dnoisespectraname.fits 2Dspectraname.fits in a ".list" file. The following commands were

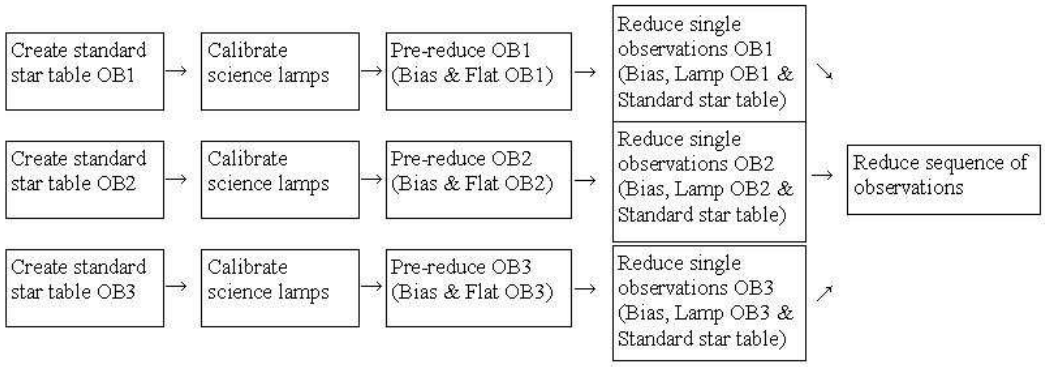

Figure A.2. Schematic of the VIMOS data reduction pipeline

then used to return a list of best redshifts and a GUI showing all of the solutions:

loadspectra spectrum=filenames.list
set lambda = 3800:8500
set overlap = 1
set ELfind = Pywin(cut=5)
set ELmatch = standard(zmax=5)
set lines_recognition = standard(cut=5)
set remove_cont = skip
set redshift = 0.01:5:0.001
set output = file(filename=redshifts.txt, mode=a)
solve
displaysession

These commands first load the spectra, set the wavelength range to use for the fitting and sets the minimum overlap between the template and spectrum. ELfind and Elmatch search for and match the emission lines to possible redshift values. Pywin is the algorithm used for searching for the emission lines and cut sets the threshold level for considering it as an emission line. In ELmatch the standard algorithm is used and the maximum redshift is set to 5. As we want to use the continuum information in determination of the redshifts we skip the continuum removal section of the code.

Appendix B

DR8 Appendix

This plot is similar to the one shown in Figure 6.3 but plotted in 1 Gyr redshift bins.

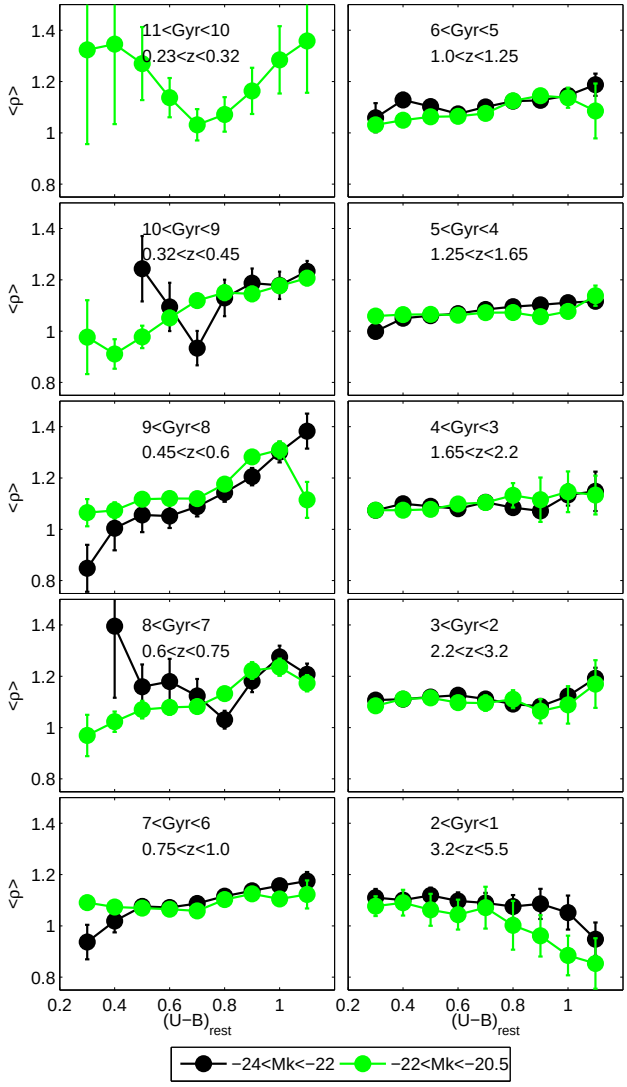

Figure B.1. (U-B) colour against density in Gyr bins. Showing bright (black line) and faint (green line) objects.

Bibliography

Baldry I. K., Glazebrook K., Brinkmann J., Ivezić Ž., Lupton R. H., Nichol R. C., Szalay A. S., 2004, ApJ, 600, 681

Baldwin J. A., Phillips M. M., Terlevich R., 1981, PASP, 93, 5

Balogh M. L., Baldry I. K., Nichol R., Miller C., Bower R., Glazebrook K., 2004, ApJ, 615, L101

Balogh M. L., Morris S. L., Yee H. K. C., Carlberg R. G., Ellingson E., 1999, ApJ, 527, 54

Bamford S. P., Nichol R. C., Baldry I. K., Land K., Lintott C. J., Schawinski K., Slosar A., Szalay A. S., Thomas D., Torki M., Andreescu D., Edmondson E. M., Miller C. J., Murray P., Raddick M. J., Vandenberg J., 2009, MNRAS, 393, 1324

Barger A. J., Cowie L. L., Wang W., 2008, ApJ, 689, 687

Bell E. F., Wolf C., Meisenheimer K., Rix H.-W., Borch A., Dye S., Kleinheinrich M., Wisotzki L., McIntosh D. H., 2004, ApJ, 608, 752

Benítez N., 2000, ApJ, 536, 571

Benson A. J., 2005, Royal Society of London Philosophical Transactions Series A, 363, 695

Birnboim Y., Dekel A., 2003, MNRAS, 345, 349

Blanton M. R., Hogg D. W., Bahcall N. A., Baldry I. K., Brinkmann J., Csabai I., Eisenstein D., Fukugita M., Gunn J. E., Ivezić Ž., others 2003, ApJ, 594, 186

Bolzonella M., Miralles J., Pelló R., 2000, A&A, 363, 476

Bower R. G., Lucey J. R., Ellis R. S., 1992, MNRAS, 254, 601

Brammer G. B., Whitaker K. E., van Dokkum P. G., Marchesini D., Labbé I., Franx M., Kriek M., Quadri R. F., Illingworth G., Lee K., Muzzin A., Rudnick G., 2009, ApJ, 706, L173

Brinchmann J., Ellis R. S., 2000, ApJ, 536, L77

Bruzual G., Charlot S., 2003, MNRAS, 344, 1000

Bruzual A. G., Charlot S., 1993, ApJ, 405, 538

Buitrago F., Trujillo I., Conselice C. J., Bouwens R. J., Dickinson M., Yan H., 2008, ApJ, 687, L61

Calzetti D., Armus L., Bohlin R. C., Kinney A. L., Koornneef J., Storchi-Bergmann T., 2000, ApJ, 533, 682

Cardelli J. A., Clayton G. C., Mathis J. S., 1989, ApJ, 345, 245

Casali M., Adamson A., Alves de Oliveira C., Almaini O., Burch K., Chuter T., Elliot J., Folger M., Foucaud S., Hambly N., Hastie M., Henry D., Hirst P., Irwin M., Ives D., Lawrence A., Laidlaw K., others 2007, A&A, 467, 777

Cassata P., Cimatti A., Kurk J., Rodighiero G., Pozzetti L., Bolzonella M., Daddi E., Mignoli M., Berta S., Dickinson M., Franceschini A., Halliday C., Renzini A., Rosati P., Zamorani G., 2008, A&A, 483, L39

Chuter R. W., Almaini O., Hartley W. G., McLure R. J., Dunlop J. S., Foucaud S., Conselice C. J., Simpson C., Cirasuolo M., Bradshaw E. J., 2011, MNRAS, 413, 1678

Cid Fernandes R., Mateus A., Sodré L., Stasińska G., Gomes J. M., 2005, MNRAS, 358, 363

Cid Fernandes R., Schoenell W., Gomes J. M., Asari N. V., Schlickmann M., Mateus A., Stasinska G., Sodré Jr. L., Torres-Papaqui J. P., 2009, in Revista Mexicana de Astronomia y Astrofisica Conference Series Vol. 35 of Revista Mexicana de Astronomia y Astrofisica, vol. 27. pp 127–132

Cimatti A., Cassata P., Pozzetti L., Kurk J., Mignoli M., Renzini A., Daddi E., Bolzonella M., Brusa M., Rodighiero G., Dickinson M., Franceschini A., Zamorani G., Berta S., Rosati P., Halliday C., 2008, A&A, 482, 21

Cimatti A., Daddi E., Renzini A., Cassata P., Vanzella E., Pozzetti L., Cristiani S., Fontana A., Rodighiero G., Mignoli M., Zamorani G., 2004, Nature, 430, 184

Cirasuolo M., McLure R. J., Dunlop J. S., Almaini O., Foucaud S., Simpson C., 2010, MNRAS, 401, 1166

Cirasuolo M., McLure R. J., Dunlop J. S., Almaini O., Foucaud S., Smail I., Sekiguchi K., Simpson C., Eales S., Dye S., Watson M. G., Page M. J., Hirst P., 2007, MNRAS, 380, 585

Conselice C. J., 2003, ApJS, 147, 1

Conselice C. J., Bluck A. F. L., Buitrago F., Bauer A. E., Grützbauch R., Bouwens R. J., Bevan S., Mortlock A., Dickinson M., Daddi E., Yan H., Scott D., Chapman S. C., Chary R.-R., others 2011, MNRAS, 413, 80

Conselice C. J., Bundy K., U V., Eisenhardt P., Lotz J., Newman J., 2008, MNRAS, 383, 1366

Conselice C. J., Rajgor S., Myers R., 2008, MNRAS, 386, 909

Cooper M. C., Coil A. L., Gerke B. F., Newman J. A., Bundy K., Conselice C. J., Croton D. J., Davis M., Faber S. M., Guhathakurta P., Koo D. C., Lin L., Weiner B. J., Willmer C. N. A., Yan R., 2010, MNRAS, 409, 337

Cooper M. C., Newman J. A., Coil A. L., Croton D. J., Gerke B. F., Yan R., Davis M., Faber S. M., Guhathakurta P., Koo D. C., Weiner B. J., Willmer C. N. A., 2007, MNRAS, 376, 1445

Cooper M. C., Newman J. A., Croton D. J., Weiner B. J., Willmer C. N. A., Gerke B. F., Madgwick D. S., Faber S. M., Davis M., Coil A. L., Finkbeiner D. P., Guhathakurta P., Koo D. C., 2006, MNRAS, 370, 198

Cooper M. C., Newman J. A., Madgwick D. S., Gerke B. F., Yan R., Davis M., 2005, ApJ, 634, 833

Cooper M. C., Newman J. A., Weiner B. J., Yan R., Willmer C. N. A., Bundy K., Coil A. L., Conselice C. J., Davis M., Faber S. M., Gerke B. F., Guhathakurta P., Koo D. C., Noeske K. G., 2008, MNRAS, 383, 1058

Cooper M. C., Tremonti C. A., Newman J. A., Zabludoff A. I., 2008, MNRAS, 390, 245

Cowie L. L., Songaila A., Hu E. M., Cohen J. G., 1996, AJ, 112, 839

Cucciati O., Iovino A., Marinoni C., Ilbert O., Bardelli S., Franzetti P., Le Fèvre O., Pollo A., Zamorani G., Cappi A., Guzzo L., McCracken H. J., Meneux B., Scaramella R., Scodeggio M., Tresse L., others 2006, A&A, 458, 39

Daddi E., Cimatti A., Renzini A., Fontana A., Mignoli M., Pozzetti L., Tozzi P., Zamorani G., 2004, ApJ, 617, 746

Daddi E., Renzini A., Pirzkal N., Cimatti A., Malhotra S., Stiavelli M., Xu C., Pasquali A., Rhoads J. E., Brusa M., di Serego Alighieri S., Ferguson H. C., Koekemoer A. M., Moustakas L. A., Panagia N., Windhorst R. A., 2005, ApJ, 626, 680

Daddi E., Röttgering H. J. A., Labbé I., Rudnick G., Franx M., Moorwood A. F. M., Rix H. W., van der Werf P. P., van Dokkum P. G., 2003, ApJ, 588, 50

Davis M., Faber S. M., Newman J., Phillips A. C., Ellis R. S., Steidel C. C., Conselice C., Coil A. L., Finkbeiner D. P., Koo D. C., Guhathakurta P., Weiner B., Schiavon R., Willmer C., Kaiser N., others 2003, in P. Guhathakurta ed., Society of Photo-Optical Instrumentation Engineers (SPIE) Conference Series Vol. 4834 of Presented at the Society of Photo-Optical Instrumentation Engineers (SPIE) Conference. pp 161–172

Dekel A., Birnboim Y., 2006, MNRAS, 368, 2

Dickinson M., Giavalisco M., GOODS Team 2003, in R. Bender & A. Renzini ed., The Mass of Galaxies at Low and High Redshift pp 324–+

Dressler A., 1980, ApJ, 236, 351

Elbaz D., Daddi E., Le Borgne D., Dickinson M., Alexander D. M., Chary R., Starck J., Brandt W. N., Kitzbichler M., MacDonald E., Nonino M., Popesso P., Stern D., Vanzella E., 2007, A&A, 468, 33

Faber S. M., Jackson R. E., 1976, ApJ, 204, 668

Fan L., Lapi A., De Zotti G., Danese L., 2008, ApJ, 689, L101

Farouki R., Shapiro S. L., 1981, ApJ, 243, 32

Foucaud S., Almaini O., Smail I., Conselice C. J., Lane K. P., Edge A. C., Simpson C., Dunlop J. S., McLure R. J., Cirasuolo M., Hirst P., Watson M. G., Page M. J., 2007, MNRAS, 376, L20

Franzetti P., Scodeggio M., Garilli B., Vergani D., Maccagni D., Guzzo L., Tresse L., Ilbert O., Lamareille F., Contini T., Le Fèvre O., Zamorani G., Brinchmann J., Charlot S., Bottini D., others 2007, A&A, 465, 711

Furusawa H., Kosugi G., Akiyama M., Takata T., Sekiguchi K., Tanaka I., Iwata I., Kajisawa M., Yasuda N., Doi M., Ouchi M., Simpson C., Shimasaku K., Yamada T., Furusawa J., Morokuma T., Ishida C. M., others 2008, ApJS, 176, 1

Gerke B. F., Newman J. A., Faber S. M., Cooper M. C., Croton D. J., Davis M., Willmer C. N. A., Yan R., Coil A. L., Guhathakurta P., Koo D. C., Weiner B. J., 2007, MNRAS, 376, 1425

Grützbauch R., Chuter R. W., Conselice C. J., Bauer A. E., Bluck A. F. L., Buitrago F., Mortlock A., 2011, MNRAS, 412, 2361

Grützbauch R., Conselice C. J., Varela J., Bundy K., Cooper M. C., Skibba R., Willmer C. N. A., 2010, MNRAS, pp 1856–+

Gunn J. E., Gott III J. R., 1972, ApJ, 176, 1

Hartley W. G., Almaini O., Cirasuolo M., Foucaud S., Simpson C., Conselice C. J., Smail I., McLure R. J., Dunlop J. S., Chuter R. W., Maddox S., Lane K. P., Bradshaw E. J., 2010, MNRAS, 407, 1212

Hartley W. G., Lane K. P., Almaini O., Cirasuolo M., Foucaud S., Simpson C., Maddox S., Smail I., Conselice C. J., McLure R. J., Dunlop J. S., 2008, MNRAS, 391, 1301

Hogg D. W., Blanton M. R., Eisenstein D. J., Gunn J. E., Schlegel D. J., Zehavi I., Bahcall N. A., Brinkmann J., Csabai I., Schneider D. P., Weinberg D. H., York D. G., 2003, ApJ, 585, L5

Hopkins P. F., Bundy K., Hernquist L., Wuyts S., Cox T. J., 2010, MNRAS, 401, 1099

Hubble E. P., 1925, The Observatory, 48, 139

Hubble E. P., 1936, Realm of the Nebulae

Iovino A., Cucciati O., Scodeggio M., Knobel C., Kovač K., Lilly S., Bolzonella M., Tasca L. A. M., Zamorani G., Zucca E., Caputi K., Pozzetti L., Oesch P., Lamareille F., Halliday C., others. 2010, A&A, 509, A40+

Kauffmann G., Charlot S., 1998, MNRAS, 294, 705

Kauffmann G., Heckman T. M., White S. D. M., Charlot S., Tremonti C., Brinchmann J., Bruzual G., Peng E. W., Seibert M., Bernardi M., Blanton M., Brinkmann J., others. 2003, MNRAS, 341, 33

Kauffmann G., White S. D. M., Heckman T. M., Ménard B., Brinchmann J., Charlot S., Tremonti C., Brinkmann J., 2004, MNRAS, 353, 713

Kereš D., Katz N., Weinberg D. H., Davé R., 2005, MNRAS, 363, 2

Kewley L. J., Geller M. J., Jansen R. A., 2004, AJ, 127, 2002

Kinney A. L., Calzetti D., Bohlin R. C., McQuade K., Storchi-Bergmann T., Schmitt H. R., 1996, ApJ, 467, 38

Kocevski D. D., Lemaux B. C., Lubin L. M., Shapley A. E., Gal R. R., Squires G. K., 2010, ArXiv e-prints

Kriek M., van der Wel A., van Dokkum P. G., Franx M., Illingworth G. D., 2008, ApJ, 682, 896

Kurk J., Cimatti A., Zamorani G., Halliday C., Mignoli M., Pozzetti L., Daddi E., Rosati P., Dickinson M., Bolzonella M., Cassata P., Renzini A., Franceschini A., Rodighiero G., Berta S., 2009, A&A, 504, 331

Lacey C., Cole S., 1993, MNRAS, 262, 627

Lawrence A., Warren S. J., Almaini O., Edge A. C., Hambly N. C., Jameson R. F., Lucas P., Casali M., Adamson A., Dye S., Emerson J. P., Foucaud S., Hewett P., Hirst P., Hodgkin S. T., others 2007, MNRAS, 379, 1599

Le Fèvre O., Vettolani G., Garilli B., Tresse L., Bottini D., Le Brun V., Maccagni D., Picat J. P., Scaramella R., Scodeggio M., Zanichelli A., others 2005, A&A, 439, 845

Leitherer C., Tremonti C. A., Heckman T. M., Calzetti D., 2011, AJ, 141, 37

Lilly S. J., Le Fèvre O., Renzini A., Zamorani G., Scodeggio M., Contini T., Carollo C. M., Hasinger G., Kneib J.-P., Iovino A., Le Brun V., Maier C., others 2007, ApJS, 172, 70

Lintott C. J., Schawinski K., Slosar A., Land K., Bamford S., Thomas D., Raddick M. J., Nichol R. C., Szalay A., Andreescu D., Murray P., Vandenberg J., 2008, MNRAS, 389, 1179

Madau P., Ferguson H. C., Dickinson M. E., Giavalisco M., Steidel C. C., Fruchter A., 1996, MNRAS, 283, 1388

McGee S. L., Balogh M. L., Bower R. G., Font A. S., McCarthy I. G., 2009, MNRAS, 400, 937

Mignoli M., Cimatti A., Zamorani G., Pozzetti L., Daddi E., Renzini A., Broadhurst T., Cristiani S., D'Odorico S., Fontana A., Giallongo E., Gilmozzi R., Menci N., Saracco P., 2005, A&A, 437, 883

Moresco M., Pozzetti L., Cimatti A., Zamorani G., Mignoli M., di Cesare S., Bolzonella M., Zucca E., Lilly S., Kovač K., Scodeggio M., Cassata other 2010, A&A, 524, A67+

Mortlock A., Conselice C. J., Bluck A. F. L., Bauer A. E., Gruetzbauch R., Buitrago F., Ownsworth J., 2011, ArXiv e-prints

Naab T., Johansson P. H., Ostriker J. P., 2009, ApJ, 699, L178

Oemler Jr. A., 1974, ApJ, 194, 1

Pannella M., Gabasch A., Goranova Y., Drory N., Hopp U., Noll S., Saglia R. P., Strazzullo V., Bender R., 2009, ApJ, 701, 787

Papovich C., Momcheva I., Willmer C. N. A., Finkelstein K. D., Finkelstein S. L., Tran K., Brodwin M., Dunlop J. S., Farrah D., Khan S. A., Lotz J., McCarthy P., McLure R. J., Rieke M., Rudnick G., Sivanandam S., Pacaud F., Pierre M., 2010, ApJ, 716, 1503

Patel S. G., Holden B. P., Kelson D. D., Illingworth G. D., Franx M., 2009, ApJ, 705, L67

Poggianti B. M., Desai V., Finn R., Bamford S., De Lucia G., Varela J., Aragón-Salamanca A., Halliday C., Noll S., Saglia R., others 2008, ApJ, 684, 888

Postman M., Geller M. J., 1984, ApJ, 281, 95

Quadri R., van Dokkum P., Gawiser E., Franx M., Marchesini D., Lira P., Rudnick G., Herrera D., Maza J., Kriek M., Labbé I., Francke H., 2007, ApJ, 654, 138

Quadri R. F., Williams R. J., Franx M., Hildebrandt H., 2011, ArXiv e-prints

Riess A. G., Filippenko A. V., Challis P., Clocchiatti A., Diercks A., Garnavich P. M., Gilliland R. L., Hogan C. J., Jha S., others 1998, AJ, 116, 1009

Rosa-González D., Terlevich E., Terlevich R., 2002, MNRAS, 332, 283

Rosati P., Tozzi P., Gobat R., Santos J. S., Nonino M., Demarco R., Lidman C., Mullis C. R., Strazzullo V., Böhringer H., Fassbender R., Dawson K., Tanaka M., Jee J., Ford H., Lamer G., Schwope A., 2009, A&A, 508, 583

Rubin V. C., Ford Jr. W. K., Whitmore B. C., 1988, ApJ, 333, 522

Simpson C., Martínez-Sansigre A., Rawlings S., Ivison R., Akiyama M., Sekiguchi K., Takata T., Ueda Y., Watson M., 2006, MNRAS, 372, 741

Sobral D., Best P. N., Smail I., Geach J. E., Cirasuolo M., Garn T., Dalton G. B., 2011, MNRAS, 411, 675

Somerville R. S., Lee K., Ferguson H. C., Gardner J. P., Moustakas L. A., Giavalisco M., 2004, ApJ, 600, L171

Spergel D. N., Bean R., Doré O., Nolta M. R., Bennett C. L., Dunkley J., Hinshaw G., Jarosik N., Komatsu E., Page L., Peiris H. V., Verde L., Halpern M., Hill R. S., Kogut A., other. 2007, ApJS, 170, 377

Spinrad H., Dey A., Stern D., Dunlop J., Peacock J., Jimenez R., Windhorst R., 1997, ApJ, 484, 581

Springel V., Di Matteo T., Hernquist L., 2005, ApJ, 620, L79

Stanford S. A., Eisenhardt P. R., Dickinson M., 1998, ApJ, 492, 461

Steidel C. C., Adelberger K. L., Shapley A. E., Erb D. K., Reddy N. A., Pettini M., 2005, ApJ, 626, 44

Tadaki K., Kodama T., Koyama Y., Hayashi M., Tanaka I., Tokoku C., 2010, ArXiv e-prints

Tasca L. A. M., Kneib J., Iovino A., Le Fèvre O., Kovač K., Bolzonella M., Lilly S. J., Abraham R. G., Cassata P., Cucciati O., Guzzo L., Tresse L., Zamorani G., Capak P., Garilli B., Scodeggio M., others. 2009, A&A, 503, 379

Thomas D., Maraston C., Bender R., Mendes de Oliveira C., 2005, ApJ, 621, 673

Toomre A., Toomre J., 1972, ApJ, 178, 623

Tully R. B., Fisher J. R., 1977, A&A, 54, 661

van den Bosch F. C., Aquino D., Yang X., Mo H. J., Pasquali A., McIntosh D. H., Weinmann S. M., Kang X., 2008, MNRAS, 387, 79

van der Wel A., 2008, ApJ, 675, L13

van Dokkum P. G., Franx M., 2001, ApJ, 553, 90

White S. D. M., Frenk C. S., 1991, ApJ, 379, 52

Williams R. J., Quadri R. F., Franx M., van Dokkum P., Labbé I., 2009, ApJ, 691, 1879

Willmer C. N. A., Faber S. M., Koo D. C., Weiner B. J., Newman J. A., Coil A. L., Connolly A. J., Conroy C., Cooper M. C., Davis M., Finkbeiner D. P., Gerke B. F., Guhathakurta P., others 2006, ApJ, 647, 853

Wolf C., Gray M. E., Meisenheimer K., 2005, A&A, 443, 435

Worthey G., 1994, ApJS, 95, 107

Wuyts S., Labbé I., Schreiber N. M. F., Franx M., Rudnick G., Brammer G. B., van Dokkum P. G., 2008, ApJ, 682, 985

Yamada T., Kodama T., Akiyama M., Furusawa H., Iwata I., Kajisawa M., Iye M., Ouchi M., Sekiguchi K., Shimasaku K., Simpson C., Tanaka I., Yoshida M., 2005, ApJ, 634, 861

York D. G., Adelman J., Anderson Jr. J. E., Anderson S. F., Annis J., Bahcall N. A., Bakken J. A., Barkhouser R., Bastian S., Berman E., others 2000, AJ, 120, 1579